

A Dissertation

entitled

Development of Selective Inhibitors against Enzymes Involved in the Aspartate
Biosynthetic Pathway for Antifungal Drug Development

By

Gopal P. Dahal

Submitted to the Graduate Faculty as partial fulfillment of the requirements for the

Doctor of Philosophy Degree in Chemistry

Dr. Ronald E. Viola, Committee Chair

Dr. Donald Ronning, Committee Member

Dr. Jianglong Zhu, Committee Member

Dr. Viranga Tillekeratne, Committee Member

Dr. Amanda C. Bryant-Friedrich, Dean
College of Graduate Studies

The University of Toledo

August 2018

© Copyright by Gopal P. Dahal, 2018

This document is copyrighted material. Under copyright law, no parts of this document may be reproduced without the expressed permission of the author.

An Abstract of

Development of Selective Inhibitors against Enzymes Involved in the Aspartate
Biosynthetic Pathway for Antifungal Drug Development

by

Gopal P. Dahal

Submitted to the Graduate Faculty as partial fulfillment of the requirements for the
Doctor of Philosophy Degree in Chemistry

The University of Toledo

August 2018

Aspartate semialdehyde dehydrogenase (ASADH) functions at a critical junction in the aspartate biosynthetic pathway and represents a validated target for antimicrobial drug design. This enzyme catalyzes the NADPH-dependent reductive dephosphorylation of β -aspartyl phosphate to produce the key intermediate aspartate semialdehyde. Production of this intermediate represents the first committed step for the biosynthesis of several essential amino acids in fungi and in bacteria. The absence of this enzyme in humans and other mammals will allow the selective targeting of any ASADH inhibitors against pathogenic microorganisms.

We have accumulated significant structural and mechanistic information about the bacterial ASADHs, but have only limited knowledge of their fungal counterparts. To bridge this gap we have determined the high-resolution structures of three pathogenic fungal forms of ASADH, from *C. neoformans*, *A. fumigatus*, and from *B. dermatitidis* in both apo- and ligand-bound forms. While the overall structures of the fungal ASADHs are similar to the bacterial orthologs, some critical differences both in biological assembly and

in secondary structural features can potentially be exploited for the development of species-selective drugs with selective toxicity against infectious fungal organisms. As an initial study ~1,000 compounds from our customized fragment libraries were screened against ASADH, followed by determination of the inhibition constant (K_i) values of the most potent hits. Encouragingly, these results showed that most of the hits obtained already have K_i values in the lower micromolar range. Several of these most potent and structurally diverse initial hits were selected for structural-activity relationship (SAR) evaluation, leading to optimized inhibitors against fungal ASADH with inhibition constants in the low micromolar/high nanomolar range, while still retaining high ligand efficiency values. The efficacy of these hits was further validated using a sensitive cell-based assay against the growth of *Candida* cells. These ASADH inhibitors suppress fungal growth, with most potent hits in this cell-based assay have low micromolar IC_{50} values. Further screening of ~1000 drug-like compounds from an NIH clinical collection library and a Prestwick drug library revealed that many of the hits from these libraries have core scaffolds that are representative of those obtained from the fragment library hits. These results confirm that fragments can serve as hit predictors and as a guide for optimized inhibitor selection. Native PAGE studies and small angle x-ray scattering (SAXS) analysis showed that the fungal ASADHs exist as a functional tetramer, in contrast to the bacterial ASADHs that exist as dimers. Some of these newly identified inhibitors show a non-competitive mode of inhibition, functioning to bind and cause oligomer dissociation into inactive dimers. These compounds are being used as starting points for designing protein-protein interaction inhibitors with a unique mode of action against our fungal enzyme target. High throughput docking against a sub-set of the ZINC compound library (70,000 compounds) also yielded

hits with similar sub-structures from fragment library screening, with measured K_i values as low as 4 μM . These docking results are being used to guide the design and development of more potent inhibitors.

The second project focused on purification, characterization and crystallization of membrane bound aspartate N-acetyltransferase (ANAT) enzyme, and performing inhibitor screening against mouse and human forms of this enzyme for the treatment of Canavan Disease (CD). ANAT catalyzes the biosynthesis of N-acetyl aspartate (NAA) in neurons, a major source of acetyl groups for lipid synthesis during brain development. CD is a fatal autosomal-recessive neurodegenerative disease caused by mutations in the *acy2* gene that leads to the deficiency of the enzyme aspartoacylase, the enzyme responsible for the deacetylation of NAA in the oligodendrocytes of the brain. An approach in which selective ANAT inhibitors are used to lower brain NAA levels back into the physiological range has the potential to treat the symptoms of CD without introducing higher risks. We have now screened several bisubstrate analog inhibitors and their truncated series against ANAT, and the most potent hits have been found to inhibit ANAT in the lower nanomolar range. These bisubstrate inhibitors are also used for co-crystallization of ANAT in order to determine the crystal structure of the enzyme. This study will allow us to understand the mechanism of the enzyme and develop selective inhibitors which, upon further modifications, will produce lead compounds for the treatment of Canavan Disease.

To my Mom and Dad and my wife Sierra, who arouse my curiosity in learning new things and has always supported me ever since.

Acknowledgements

I would like to thank my academic advisor, Dr. Ronald E. Viola, for his immense support, guidance and encouragement over the past 5 years. His motivation and commitment to science inspired me and enriched my passion for research. I was fortunate enough to have a great person like him as my research advisor and all the academic accomplishments I achieved, I have learned from him and his research lab. His organization skills, patience and discipline inspired me to finish my projects in strict timelines, and the professional skills that I acquired in his lab helped me to shape myself as an independent scientist.

I would like to thank my committee members Dr. Donald R. Ronning, Dr. Jianglong Zhu, and Dr. Viranga Tillekaratne for their constant support and motivation throughout my graduate studies. I would like to thank the Department of Chemistry and Biochemistry, the University of Toledo for providing me the opportunity to pursue my graduate studies. I would also like to thank all my past and present lab members for all their support, advice and words of encouragement, and for all the insightful scientific discussions and my friend's Dr. Hem Raj Khatri, Pratik Pote, Subash Sapkota, Prabhat Napit, Bibek Joshi, Dr. Sikes Manandhar, and Yogesh Pathak for their unwavering support. To my brother Kumar and his wife Deepa, my sister Laxmi and her husband Dinesh, my niece Yojana and my nephew Rishab, I thank them for their constant love, support, encouragement, and motivation throughout this PhD journey.

Table of Contents

Abstract.....	iii
Acknowledgements.....	vii
Table of Contents.....	viii
List of Tables.....	xvi
List of Figures.....	xvii
List of Abbreviations.....	xxi
List of Symbols.....	xxiii
Chapter 1: Introduction	
1.1 Background and significance.....	1
1.2 Antifungals and their mode of action.....	3
1.3 Antifungal drug resistance.....	5
1.4 Mechanism of antifungal drug resistance.....	6
1.5 Biofilm formation.....	7
1.6 Synopsis and chapter organization.....	8
Chapter 2: Aspartate biosynthetic pathway	
2.1 Background and significance.....	9
2.2 Aspartate semialdehyde dehydrogenase (ASADH)	10

2.3 Catalytic mechanism.....	11
2.4 Structure of ASADH.....	12
2.5 ASADHs from human fungal pathogens.....	13
2.6 Biophysical characterization of aspartate semialdehyde dehydrogenase.....	15
2.6.1 Cloning, expression and purification of ASADH from <i>Cryptococcus</i> <i>neoformans</i>	15
2.6.1.1 Cloning.....	15
2.6.1.2 Yeast expression system.....	16
2.6.1.3 Gene synthesis.....	16
2.6.1.4 Pilot expression.....	17
2.6.1.5 Protein characterization.....	17
2.6.1.6 Protein purification.....	18
2.6.2 Cloning, expression and purification of ASADH from <i>Aspergillus</i> <i>fumigatus</i>	20
2.6.2.1 Cloning.....	20
2.6.2.2 Protein expression and purification.....	20
2.6.3 Cloning, expression and purification of ASADH from <i>Blastomyces</i> <i>dermatitidis</i>	22
2.6.3.1 Cloning, protein expression and purification.....	22
2.6.4 Cloning, expression and purification of ASADH from <i>Toxoplasma</i> <i>gondii</i>	24
2.6.4.1 Cloning expression and purification.....	24
2.6.4.2 GST fusion cloning of TgASADH.....	28

2.6.4.3	MBP fusion cloning of <i>Tg</i> ASADH.....	29
2.6.4.4	<i>T. gondii</i> ASADH alternative purification protocol.....	31
2.6.4.5	Other purification strategies.....	32
2.6.5	Cloning, expression and purification of ASADH from <i>Histoplasma capsulatum</i>	32
2.7	Biochemical assay of ASADHs.....	33
2.8	Kinetic parameters for the reaction catalyzed by ASADH.....	36
2.9	Kinetic screening.....	37
2.9.1	Fragment library screening.....	37
2.9.1.1	Water and DMSO-soluble fragment library preparation...38	
2.9.1.2	Constrained analog and drug library preparation.....	39
2.9.2	Results and discussion.....	41
2.9.2.1	Inhibitor identification from library screening.....	41
2.9.2.2	Selectivity of initial fungal ASADH inhibitors.....	43
2.9.2.3	Establishing the mode of ASADH inhibition.....	45
2.9.2.4	Electrospray Ionization – Mass Spectrometry (ESI-MS)...47	
2.9.2.5	Structure-Activity Relationship (SAR) studies.....	50
2.9.2.6	Inhibitor species selectivity.....	53
2.9.3	Drug library screening.....	55
2.9.4	Future inhibitor optimization.....	58
2.10	Oligomeric state of fungal ASADHs.....	58
2.10.1	Native PAGE.....	58
2.10.2	Protein-Protein interactions inhibitors.....	59

2.11 Other enzyme targets in the aspartate biosynthetic pathway.....	60
2.11.1 Homoserine dehydrogenase.....	61
2.11.1.1 Cloning of homoserine dehydrogenase.....	61
2.11.1.2 Expression and purification.....	63
2.11.1.3 Kinetic assay and library screening of <i>Ca</i> HDH.....	64
2.12 L-lysine biosynthesis in fungi.....	65
2.12.1 Homocitrate synthase.....	66
2.12.2 Homoaconitase.....	67
2.12.3 Homoisocitrate dehydrogenase.....	67
2.13 Conclusions and future work.....	69

Chapter 3: Structural studies of different ASADHs

3.1 Introduction.....	70
3.2 Pre-crystallization test (PCT) and initial crystal screening.....	71
3.3 <i>Cn</i> ASADH crystal screening.....	71
3.3.1 Crystal seeding.....	72
3.3.2 Additive screening.....	73
3.3.3 Data collection and processing.....	74
3.3.4 Structure solution and refinement.....	76
3.3.5 Results and discussion.....	76
3.3.5.1 Overall structure of <i>Cryptococcus neoformans</i> ASADH...76	

3.3.5.2	Secondary structure arrangement and comparison.....	79
3.3.5.3	Comparison to related ASADHs structures.....	80
3.3.5.4	Positioning of the conserved active site residues.....	81
3.3.5.5	Binding of an exogenous ligand.....	83
3.3.5.6	Tetramer interface and oligomeric arrangement.....	84
3.3.6	Conclusions.....	85
3.4	<i>Af</i> ASADH crystal screening.....	85
3.4.1	Data collection and processing.....	86
3.4.2	Structure solution and refinement.....	87
3.4.3	Results and discussion.....	89
3.4.3.1.	Overall structure.....	89
3.4.3.2.	Absence of cofactor and inhibitor binding.....	90
3.4.3.3	Secondary structural arrangement.....	91
3.4.3.4.	Comparison with related structures.....	92
3.4.3.5	Active site comparison.....	95
3.4.3.6	Binding of an exogenous ligand.....	96
3.4.3.7	Differences in oligomeric arrangement.....	99
3.4.4	Conclusions.....	101

3.4.5 Re-screening of <i>Af</i> ASADH crystals.....	101
3.5 <i>Bd</i> ASADH crystals screening.....	102
3.5.1 Data collection and processing.....	103
3.5.2 Result and discussion.....	105
3.5.2.1 Overall structure of a fungal ASADH.....	105
3.5.2.2 Domain and secondary structural arrangement.....	106
3.5.2.3 Comparison with related structures.....	107
3.5.2.4 Active site comparison.....	107
3.5.2.5 Cofactor binding and conformational changes.....	108
3.5.2.6 Binding of an active site inhibitor.....	109
3.5.3 Conclusions.....	111
3.6 Crystallization of <i>Tg</i> ASADH.....	111
3.7 Crystallization of <i>Ca</i> HDH.....	112
3.8 Neutron crystallography.....	112
Chapter 4: Computational studies of different ASADHs	
4.1 Docking studies.....	114
4.1.1 Ligand preparation for docking studies.....	115
4.1.2 Protein structure preparation for docking studies.....	115
4.2 High-throughput docking.....	116

4.3 Inhibitor docking and binding affinities.....	116
4.4 Zinc library virtual screening.....	120
4.5 Molecular dynamics.....	123
4.5.1 Results and discussion.....	124
4.6 Dynamic light scattering (DLS)	125
4.7 Small angle x-ray scattering (SAXS)	126
4.8 Conclusions.....	128
Chapter 5: Cell based screening of ASADH inhibitors against <i>Candida albicans</i>	
5.1 Introduction.....	129
5.2 Materials and methods.....	131
5.2.1 General reagents.....	131
5.2.2 Growth media.....	131
5.2.3 Inoculum preparation.....	131
5.2.4 Microbial susceptibility against yeast and hyphal forms.....	132
5.2.5 The growth curve of <i>C. albicans</i>	133
5.2.6 Effect of small molecule inhibitors on biofilm formation.....	134
5.3 Results and discussion.....	135
5.3.1 Antifungal susceptibility bioassay.....	135
5.3.2 Inhibitor effects on <i>C. albicans</i> growth curves.....	138
5.4 Conclusions and future work.....	140

Chapter 6 Canavan disease

6.1 Introduction.....	141
6.2 Challenges in ANAT study.....	143
6.3 Cloning of mANAT gene.....	144
6.4 Purification of mANAT.....	145
6.5 ANAT kinetic assay and biochemical properties.....	147
6.6 Crystallization of mANAT.....	148
6.7 Protein engineering of ANAT.....	149
6.8 Bisubstrate inhibitors of ANAT.....	150
6.9 Bisubstrate inhibitor design and screening.....	151
6.10 Conclusions and future work.....	154
References.....	155
Appendix.....	166
Appendix A High throughput docking configuration file.....	166
Appendix B Configuration file for MD simulation	168
Appendix C DLS parameters during analysis of <i>Af</i> ASADH sample.....	170

List of Tables

Table 2.1 Kinetic parameters catalysed by different forms of ASADH.....	36
Table 2.2 ASADH inhibitors from fragment library screening	45
Table 2.3 Selectivity of naphthoquinone derivatives against fungal ASADHs.....	54
Table 3.1 Data collection, processing and refinement statistics of <i>Cn</i> ASADH	75
Table 3.2 Data collection, processing and refinement statistics of <i>Af</i> ASADH.....	88
Table 3.3 Buried surface area and energetics of ASADH subunit dissociation.....	101
Table 3.4 Data collection, processing and refinement statistics of <i>Bd</i> ASADH.....	104
Table 4.1. Predicted affinities and measured inhibition constants of <i>Ca</i> ASADH inhibitors.....	120
Table 4.2 Compounds showing high affinity scores with K_i values against <i>Ca</i> ASADH...	122
Table 4.3: Radius of gyration distribution of different ASADHs sample with theoretical and experimental R_g parameters.....	128
Table 5.1: Effect of small molecule inhibitors against <i>Candida albicans</i>	137
Table 6.1 Kinetic evaluation of truncated analog inhibitors of ANAT	153
Table 6.2 Synergistic effect of simultaneous binding of ANAT inhibitors.....	153

List of Figures

Figure 1.1 Structures and mechanism of action of currently used antifungal drugs.....	5
Figure 2.1 The aspartate biosynthetic pathway.....	10
Figure 2.2 ASADH catalyzed reaction in biosynthetic direction.....	11
Figure 2.3 Catalytic mechanism of ASADH.....	12
Figure 2.4 MALDI-MS MASCOT search results of <i>Cn</i> ASADH	18
Figure 2.5 Elution and SDS-PAGE profile of <i>Cn</i> ASADH from Ni-IMAC column.....	19
Figure 2.6 Elution and SDS-PAGE profile of <i>Af</i> ASADH from Source 15Q column.....	21
Figure 2.7 MALDI-MS MASCOT search results of <i>Af</i> ASADH	22
Figure 2.8 Elution and SDS-PAGE profile of <i>Bd</i> ASADH from Ni-IMAC column.....	24
Figure 2.9 MALDI-MS MASCOT search results of <i>Tg</i> ASADH	26
Figure 2.10 Elution profile of <i>Tg</i> ASADH from Ni-IMAC and Source 15Qcolumn.....	27
Figure 2.11 Western blot and SDS PAGE profile of <i>Tg</i> ASADH sample.....	27
Figure 2.12 SDS-PAGE profile of GST fusion <i>Tg</i> ASADH from GST column.....	29
Figure 2.13 SDS-PAGE profile of eluted MBP fusion <i>Tg</i> ASADH from MBP column ...	30
Figure 2.14 ASADH catalyzed reaction in biosynthetic direction.....	34
Figure 2.15 Kinetic assay of ASADH at 340 nm	35
Figure 2.16 Coupled enzymatic assay of the reaction catalyzed by ASADH at 500 nm....	35
Figure 2.17 Fragment library screening against pathogenic fungi in 96-well format.....	42
Figure 2.18 ESI-MS spectra of <i>Af</i> ASADH sample and its deconvoluted spectra.....	48

Figure 2.19 ESI-MS and deconvoluted spectra of phthaldehyde treated <i>Af</i> ASADH	49
Figure 2.20 <i>p</i> -Benzoquinone structural analogs screened as potential inhibitors <i>Ca</i> ASADH.....	53
Figure 2.21 Representative dose-response curves for 2-chloro-1,4-naphthoquinone against <i>Af</i> ASADH.....	55
Figure 2.22 The most potent inhibitors against <i>Ca</i> ASADH identified from the NIH clinical collection library and the Prestwick library.....	57
Figure 2.23 Native PAGE electrophoresis of different ASADHs on 3-12% bis-tris gel	59
Figure 2.24 Effect of increasing [phthalaldehyde] on dissociation of <i>Ca</i> ASADH into inactive dimers.....	60
Figure 2.25 Agarose gel profile after PCR of <i>Ca</i> HDH gene.....	63
Figure 2.26 Elution profile and SDS-PAGE profile of <i>Ca</i> HDH from Ni-IMAC column..	64
Figure 2.27 Kinetic reaction catalyzed by homoserine dehydrogenase (HDH).....	65
Figure 2.28 Agarose gel profile after PCR of the <i>Ca</i> HID gene	68
Figure 3.1 Initial hits of <i>Cn</i> ASADH from Jena Bioscience screening kit	72
Figure 3.2 A diffraction image of <i>Cn</i> ASADH crystal at Rigaku FR-E source.....	74
Figure 3.3 Overall structure of <i>Cn</i> ASADH and its superposition with <i>Ca</i> ASADH structure.....	78
Figure 3.4 Topology diagram showing the secondary structural arrangement of a <i>Cn</i> ASADH monomer.....	79
Figure 3.5 Sequence alignment of representative ASADH enzymes from fungal, bacterial and archael forms.....	81

Figure 3.6 Superposition of the active site residues involve in substrate binding and catalysis between <i>Cn</i> ASADH and <i>Ca</i> ASADH.....	82
Figure 3.7 Schematic representation of the interaction made by ethylene glycol (EG) bound at the active site.....	84
Figure 3.8 Initial hits from Index screening from <i>Af</i> ASADH at 14 mg/ml	86
Figure 3.9 Overall structure of <i>Af</i> ASADH and its superposition with <i>Cn</i> ASADH.....	90
Figure 3.10 <i>Af</i> ASADH monomer showing the secondary structural arrangement	92
Figure 3.11 Sequence alignment of representative ASADH enzymes from fungal, bacterial and archael forms.....	94
Figure 3.12 Superpositioning of the residues in the active site of <i>Af</i> ASADH and <i>Cn</i> ASADH.....	96
Figure 3.13 Representative electron density and modelling of amino acid side chains and sulfate ion bound near the active site.....	99
Figure 3.14 Re-screening hits of <i>Af</i> ASADH sample	102
Figure 3.15 Initial hits from Index screening for <i>Bd</i> ASADH at 10 mg/ml	102
Figure 3.16 Overall structure of <i>Bd</i> ASADH with NADP bound in both subunits.....	106
Figure 3.17 Electron density of NADP bound to <i>Bd</i> ASADH in the cofactor binding site.....	109
Figure 3.18 Hydrogen bonding and hydrophobic interactions made by <i>p</i> -benzoquinone bound to <i>Bd</i> ASADH.....	110
Figure 3.19 Crystallization of <i>Ca</i> HDH at 10 mg/ml using Hampton index screening...	112
Figure 3.20 A typical sandwich box setup and neutron crystals of <i>Af</i> ASADH.....	113

Figure 4.1 Predicted binding mode of 1,4-naphthoquinone derivatives binding in the active site of <i>Ca</i> ASADH.....	119
Figure 4.2 best binding pose and H-bonding interactions of ZINC01574202 in the active site of <i>Ca</i> ASADH	123
Figure 4.3: RMSD variation versus the simulation time after 4 ns MD simulation.....	125
Figure 4.4 DLS analysis of <i>Af</i> ASADH sample	125
Figure 4.5 SAXS analysis of <i>Af</i> ASADH sample	127
Figure 5.1 Growth of the CAF2-1 wild-type strain of <i>C. albicans</i>	133
Figure 5.2 <i>Candida albicans</i> biofilm observed under a light microscope at 10x magnification.....	135
Figure 5.3 Relationship between K_i vs IC_{50} values of small molecule inhibitors against <i>C. albicans</i>	137
Figure 5.4 Structures of the most potent <i>C. albicans in vivo</i> growth inhibitors and <i>C. albicans</i> ASADH <i>in vitro</i> inhibitors	138
Figure 5.5 Effect of various concentrations of 2,3-dichloro-1,4-naphthoquinone on the growth of <i>C. albicans</i>	139
Figure 6.1 Schematic representation of the biological role of ANAT and aspartoacylase in the human brain.....	143
Figure 6.2 Elution profile and SDS-PAGE profile of mANAT from Ni-IMAC column .	146
Figure 6.3 Elution profile and SDS-PAGE profile of mANAT from amylose column...	146
Figure 6.4 Schematic representation of DTNB assay for ANAT activity measurement...	147
Figure 6.5 mANAT MembFrac screening results.....	149
Figure 6.6 ANAT bisubstrate analog and its truncation series	153

List of Abbreviations

6xHis	Hexahistidine
AdoMet	S-adenosyl methionine
<i>Af</i>	<i>Aspergillus fumigatus</i>
ADP.....	Adenosine diphosphate
ANAT	Aspartate N-acetyltransferase
APS	Advanced Photon Source
ASA.....	Aspartate semialdehyde
ASADH.....	Aspartate semialdehyde dehydrogenase
ASPA	Aspartoacylase
ATCC.....	American Type Culture Collection
ATP.....	Adenosine triphosphate
<i>Bd</i>	<i>Blastomyces dermatitidis</i>
<i>Bs</i>	<i>Bacillus subtilis</i>
<i>Ca</i>	<i>Candida albicans</i>
CD.....	Canavan Disease
CDC	Center for Disease Control and Prevention
Co-IMAC	Cobalt-immobilized metal affinity chromatography
DMF.....	Dimethylformamide
DMSO.....	Dimethyl sulfoxide
DNA.....	Deoxyribonucleic acid
DTT.....	Dithiothreitol
EDTA.....	Ethylenediaminetetraacetic acid
EG	Ethylene glycol
ESI.....	Electrospray Ionization
GST	Glutathione S-transferase
<i>Hc</i>	<i>Histoplasma capsulatum</i>
HCS.....	Homocitrate synthase
HDH.....	Homoserine dehydrogenase
HEPES	4-(2-Hydroxyethyl)-1-piperazineethane sulfonic acid

Hi.....*Haemophilus influenzae*
 HK.....Homoserine kinase
 HMT.....Homocysteine methyltransferase

 INT.....Iodonitrotetrazolium chloride
 IPTG.....Isopropyl β -D-1-thiogalactopyranoside

 kDa.....Kilodalton
 MALDI-MSMatrix-assisted laser desorption/ionization – Mass Spectrometry
 MBPMaltose binding protein
 MES2-(N-morpholino) ethanesulfonic acid
 MRSAMethicillin-resistant *Staphylococcus aureus*

 NAA.....N-acetyl aspartate
 NADPH.....Nicotinamide adenine dinucleotide phosphate
 NBS.....N-Bromosuccinamide
 NIHNational Institutes of Health
 NIHCCNIH Clinical Collection
 Ni-NTA.....Nickel-nitrilotriacetic acid
 NMRNuclear Magnetic Resonance

Pa.....*Pseudomonas aeruginosa*
 PCR.....Polymerase Chain Reaction
 PDB.....Protein Data Bank
 PEG.....Polyethylene glycol
 PMS.....Phenazine methosulfate

 rpmRevolutions per minute

Sa.....*Staphylococcus aureus*
Sp.....*Streptococcus pneumoniae*

Tg*Toxoplasma gondii*

 UV.....Ultra-violet

Vc*Vibrio cholerae*

List of Symbols

%	Percentage
μ	Micron
\AA	Angstroms
ϕ	Phi
α	Alpha
β	Beta
γ	Gama
ε	Epsilon
σ	Sigma
ψ	Psi
$^{\circ}\text{C}$	degree celsius
M	molar
mg	milligrams
mL	milliliter
mM	millimolar
nm	nanometer
nM	nanomolar
rpm	revolution per minute
v/v	volume/volume
w/v	weight/volume
μL	microliter
μM	micromolar

Chapter 1

Introduction

1.1 Background and significance

Fungal infections are a global health problem, and they can affect millions of people worldwide¹. These infections pose serious threats to human life, ranging from superficial skin infections to life threatening infections such as candidiasis and aspergillosis. The most common human fungal pathogens to humans include *Candida albicans* (20% to 40% mortality),² *Cryptococcus neoformans* (20% to 70%)³ and *Aspergillus fumigatus* (50% to 90%) causing ~ 1.5 million life threatening infections annually⁴. Spores released from these fungi can elicit several types of allergic reactions depending upon the different taxonomic branch⁵. Fungi can infect a healthy human host, but the highest incidences of serious infections occur in immunocompromised populations such as neonates, cancer patients receiving chemotherapy, organ transplant patients and patients suffering from HIV⁵. These fungal pathogens are of two types: filamentous fungi and yeasts. Filamentous fungi are the primary pathogens, while yeasts are opportunistic pathogens⁵. Recently, a significant increase in the frequency of fungal infections is threatening to overwhelm our limited array of antifungal drugs, compared to the much wider range of antibacterial agents that are currently available. Also, previously benign fungi have now become the cause of systemic

fungus infections in immunocompromised patients⁶. Also, many fungal species, including *Candida* and *Aspergillus* are developing resistance to those available antifungal drugs⁶, paralleling the phenomenon observed in bacteria. The Center for Disease Prevention and Control (CDC) has already classified *Candida* infections as a serious threat to human health, due to the dramatic increase in resistance to currently available antifungal drugs.⁷ So, the search for new antifungal agents against new targets should be of utmost importance, due both to intrinsic resistance and to the development of resistance during treatment with available antifungal drugs.

The development of antifungal agents has lagged behind antibacterials due to significant differences in cellular structure between these organisms. This antifungal drug deficiency is likely due to fungi being eukaryotic, with more limited molecular targets available for selective antifungal development without cross-target effects in humans. Most agents that are toxic to fungi are also toxic to the human host⁶. Bacteria, being prokaryotic, possess numerous structural and metabolic targets that are different than the human host⁸. Additionally, there have not been epidemics of fungal outbreaks, in contrast to those caused by bacteria such as tuberculosis, bubonic plague, malaria, etc. Also, fungal infections, in comparison to bacterial infections, are typically less life threatening on the basis of frequency of occurrence, severity and fatality by these organisms. In addition, fungi are multicellular and generally grow slower and are more difficult to quantify than bacteria⁸. Because of these reasons, the experimental design and properties of a particular antifungal agent are more difficult to evaluate.

1.2 Antifungals and their mode of action

Antifungal drugs are used for the treatment and prevention of fungal infections, and they act by either inhibiting or killing the fungal growth. These agents selectively eliminate the pathogens from a host, typically with minimal toxicity to the host⁸. Despite extensive research aimed at developing new agents to combat fungal infections, there are currently only a handful of frontline antifungal agents. These agents, from four different molecular classes targeting three distinct metabolic pathways, are currently used in the treatment of essentially all systemic fungal infections. These classes consist of fluoropyrimidine analogues, polyenes, azoles and newly discovered echinocandins.⁵ There is clearly a growing need to develop new antifungals against novel targets to be available for use in clinical settings. Current antifungals available in the market are classified into four distinct types depending on their cellular target and mechanism of action (Figure 1).

Polyenes: These are the first developed, very powerful but highly toxic antifungals (developed in 1950s) which act by binding ergosterol (the main component of fungal membrane sterols). Fungi possess a unique ergosterol membrane differing from mammalian cholesterol, and these polyenes form transmembrane pores in the ergosterol membrane which disrupts cellular permeability and eventually leads to cellular death. These transmembrane channels/pores will allow small molecules to leak from the inside of the fungal cell to the outside⁸. These agents are all derived from *Streptomyces* species, and are characterized by alternating conjugated double bonds that constitute a part of their macrolide ring structure. These agents (e.g., Amphotericin B, nystatin, and pimaricin) are the last line of defense to combat invasive fungal infections, and are widely used due to their broad spectrum efficacy.

Pyrimidines: These pyrimidines were developed in 1960s but acquired drug resistance quickly, so they are currently being used in combination with other polyene antifungals⁴. These agents (e.g. flucytosine) act by causing RNA miscoding and inhibiting DNA synthesis *via* the intracytoplasmic conversion of 5-fluorocytosine to 5-fluorouracil

Azoles: Azoles target the unique enzyme lanosterol 14- α demethylase, which catalyzes the synthesis of ergosterol from lanosterol in fungal cell membranes⁹. The ergosterol membrane is essential for fungal cell membrane structure and function. These are characterized by the presence of unique 5-membered azole rings that contain either two (the imidazoles) or three nitrogen atoms (the triazoles). These agents (e.g. fluconazole and voriconazole) are the most widely used antifungals due to their better safety profile and availability in both oral and intravenous formulations.

Echinocandins: These are recently developed antifungals (e.g. caspofungin, micafungin) targeting β -(1,3)-D-glucan synthase, an enzyme involved in glucan biosynthesis, an essential component in the fungal cell wall. This enzyme is absent in humans so toxicity from these compounds is minimal.

Despite the recent advances in antifungal therapy and new antifungal targets, the treatment options against these fungal infections is suboptimal, and mortality and morbidity rates due to these fungal infections is unacceptably high. Due to this limited array of antifungals, several targets are under study for the development of potential new antifungals. Of those, the most promising targets currently under development include: fungal sphingolipids, GPI anchor biosynthesis, Farnesyl transferase, Calcineurin, Hsp90, Acetyl transferase and deacetylase.

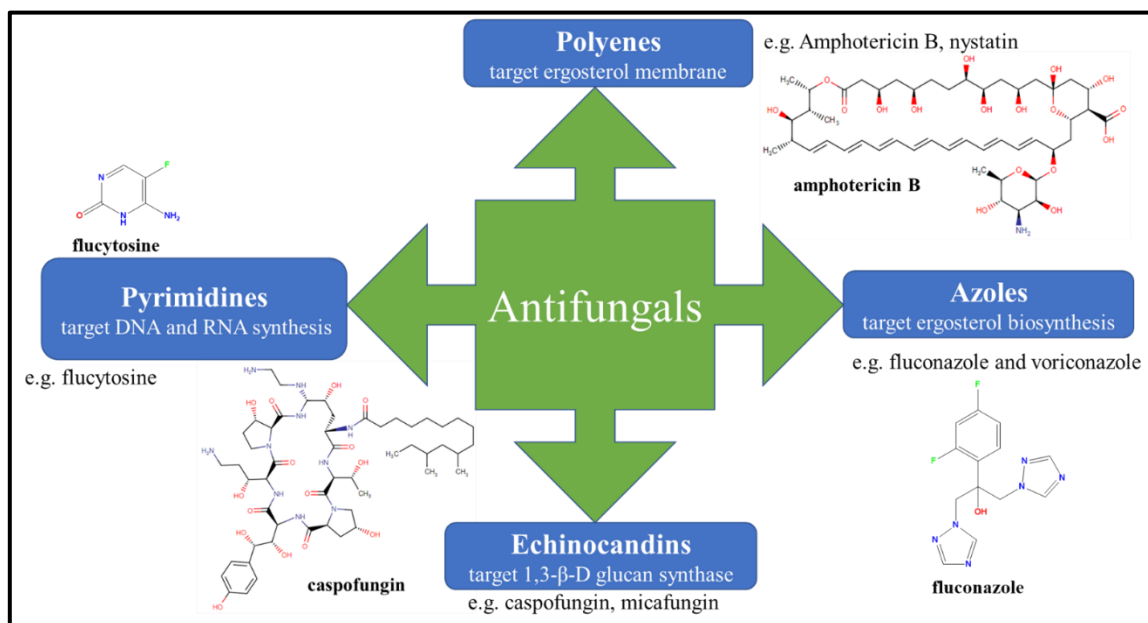


Figure 1.1: Structures and mechanism of action of currently used antifungal drugs in the market with their targets and examples.

1.3 Antifungal drug resistance

Although there are significant efforts being devoted in research and development of new antifungals, all the available drugs are having high level of drug resistance to newly emerging pathogenic fungal strains, and also to existing strains. Some pathogenic strains are also showing multiple drug resistance to recently developed antifungals. This resistance is due to wide use of the same frontline drug, and also to fungi being able to adapt themselves to survive under harsh condition either by modifying the drug or by modifying the target. Antifungal resistance arise in the clinical settings when the growth of the specific fungal pathogen is unaffected after administering a therapeutic concentration of the antifungal agent.¹⁰ Antifungal resistance threat is a global issue with pathogenic fungi *Candida albicans* being treated in the list of the serious threat to human health according

to Center for Disease Prevention and Control (CDC) report, 2016. This is due to the dramatic increase in resistance to currently available antifungal drugs against *Candida* infections.

1.4 Mechanism of antifungal drug resistance

Fungi can overcome the effect of antifungals either by mutating the drug target, eventually reducing the affinity of the drug, overexpressing the target protein by promoter region modification in the gene sequence, increasing efflux of the drug out of the cell, or by degrading the drug molecule¹¹. **Azoles** are notoriously susceptible to drug resistance, and it primarily occurs by mutating the target genes CYP51A and CYP51B which reduce the interaction of the drug with its genetic product, with the amino acids G54, P216, F219, M220, and G448 being the most common sites for mutation¹¹. Resistance also occurs in azoles through efflux of drugs by multi-drug transporters and by overexpression of the Erg11p, thereby minimizing the effect of the drug. Echinocandins undergo drug resistance due to the mutation of the drug target. **Echinocandin** targets beta-1,3-D-glucan synthase, an enzyme that consists of three FKS subunits. Resistance occurred by modifying the amino acids in the FKS1 and FKS2 subunits of the enzyme, which will increase the MIC level required for the administered drug needed to dramatic reduce the glucan synthase activity. The predominant site of the mutation in the FKS gene is a short conserved region, known as “hot-spot” region of the gene, that encodes the FKS1 and FKS2 subunit of beta-1,3-D-glucan synthase. Resistance to **polyenes** is the least compared to other antifungals, and it is generally due to increase level of production of reactive oxygen species (ROS), altering the mitochondrial activity that leads to reduced ergosterol concentration, and by reducing the drug target binding¹⁰. **Pyrimidine** analogs undergo resistance by specific

mutations in the cytosine permease and deaminase enzyme, which inhibits the drugs effect on the DNA and RNA synthesis, or by slowing the molecular machinery of the particular fungal pathogen¹⁰. Also, sometimes drug resistance is due to adaptive stress response as the highly dynamic nature of the fungal cell allows it to synthesize many of the cell wall components even if any specific cell wall biosynthetic pathway is disrupted¹². Although fungi have adapted a wide range of antifungal resistance mechanisms, the significance of each mechanism differs significantly between species, and also between the different strains of the same species¹³.

Concurrently, antimicrobial drug resistance along with the frequency and severity of fungal infections is increasing significantly over the recent years, and **biofilm formation** is among the leading cause for the drug resistance. This issue is even more acute for treating pathogenic infections from biofilm forming species¹⁴, since there are fewer effective anti-biofilm inhibitors even before the emergence of resistance. To combat such high microbial resistance infections and their drug-resistant biofilms, developing small molecule inhibitors against these biofilm is of utmost importance.

1.5 Biofilm formation

Biofilms are organized, highly structured surface-associated cell aggregates that are enclosed within a protective extracellular matrix¹⁵⁻¹⁶. These biofilms are attached to surfaces and exist within self-produced extracellular polymeric substances (EPS). The formation of biofilms is the emerging global cause of drug resistance for bacteria and fungi. There are multiple factors necessary for biofilm formation, such as pili and other appendages, quorum sensing molecules, motility, and EPS. Each of these critical biofilms forming factors are responsible for rendering the microbes more resistant to drugs, and it

is estimated that about 65% of all human infections are related to biofilm formation. Also, these biofilms constitute a phenotypic shift from individual planktonic bacteria to a surface associated community of bacteria with contrasting gene expression profiles, cellular compositions and reduced growth rates making their treatment strategy difficult. Biofilm formation provides microbes enhanced survivability on surfaces, including in-dwelling on medical devices, hospital equipment and clothing, leading to higher rates of secondary infection.

1.6 Synopsis and chapter organization

The research described in this dissertation focuses on the development of inhibitors against enzymes involved in an amino acid biosynthetic pathway and approaches for the treatment of Canavan Disease. **Chapter 2** emphasizes the cloning, expression and purification of different enzymes involved in amino acid biosynthesis. It also describes the development of potent inhibitors against different fungal ASADHs through library screening. The crystallization and structure determination aspects of different ASADHs is discussed in **Chapter 3**, and the computational studies that augment the structural features are described in **Chapter 4**. **Chapter 5** explains the cell-based studies of *in vitro* ASADH inhibitors against *C. albicans* and enzymology and bisubstrate inhibitor development of ANAT are summarized in **Chapter 6**.

Chapter 2

Aspartate Biosynthetic Pathway

2.1 Background and significance

The continuous widespread increase in antimicrobial resistance by microbes has become a serious threat to human health. There is urgency in developing potent antifungals and antibacterials which can stop antimicrobial growth. The aspartate biosynthetic pathway¹⁷ exists as a unique biosynthetic pathway in microorganism which is responsible for the biosynthesis of three essential amino acids; i.e., methionine, threonine, and isoleucine in fungi, and including lysine in bacteria (Figure 2.1). In addition to these essential amino acids, several important metabolites are synthesized by this pathway that play crucial role in various cellular development process. Dihydropicolinate, a precursor of the intermediate dipicolinate, is essential for sporulation in certain Gram-positive bacteria¹⁸. UDP-MurNAc pentapeptide, produced from the intermediate diaminopimelate, is an essential bacterial cross-linking material for peptidoglycan polymers¹⁹. S-adenosyl methionine (AdoMet), an essential requisite for methyl transfer reaction which is crucial for cell growth and viability is synthesized through this pathway¹⁷. Acyl-L-homoserine lactones and 4, 5-dihydroxy-2, 3-pentanedione, obtained from S-adenosyl methionine are bacterial quorum signaling molecules that play critical roles in activating virulence in

infectious microorganisms. The level of each amino acid and total amino acid production in this pathway is regulated by the end product amino acids *via* feedback inhibition and selective gene repression¹⁷. Since this critical pathway is only present in plants and microbes but absent in mammals, any disruptions of the critical enzymes in this pathway will be fatal to these organisms. Therefore, enzymes in this pathway are attractive and untested targets for antifungal drug development.

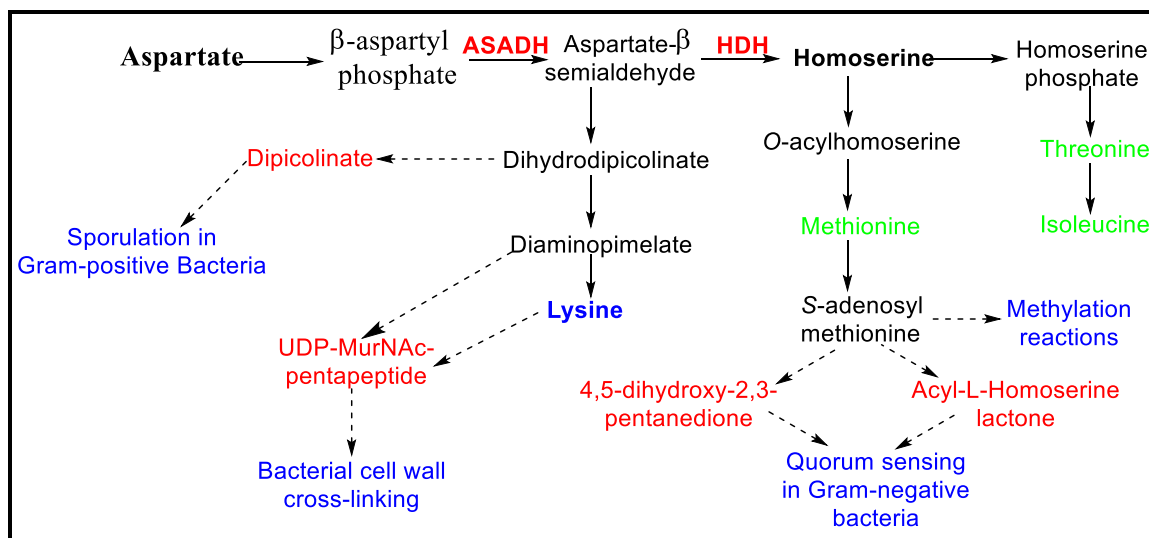


Figure 2.1: The aspartate biosynthetic pathway. The amino acids threonine, isoleucine and methionine (shown in green) are synthesized *via* this pathway in fungi, and also lysine (shown in blue, bold) in bacteria.

2.2 Aspartate semialdehyde dehydrogenase (ASADH)

Aspartate semialdehyde dehydrogenase (ASADH; E.C. 1.2.1.11) is the central enzyme in the aspartate pathway, and inhibition of which causes blockage of the entire aspartate pathway, leading to microbial death. ASADH lies at the first branch point of aspartate biosynthetic pathway and catalyze the nicotinamide adenine dinucleotide phosphate (NADPH)-dependent reductive dephosphorylation of the substrate aspartyl

phosphate to produce aspartate semialdehyde in the biosynthetic direction (Figure 2.2). This is a unique and previously untested target that can potentially be exploited as an antifungal drug target. The critical catalytic functional groups²⁰ and substrate binding groups²¹ are highly conserved in all of the ASADHs studied to date, despite sequence homologies ranging from more than 90% to less than 10%²². The key amino acid residues are Cys156 acting as an active site nucleophile and His256 acts as an acid/base catalyst. The cofactor NADP is positioned through interactions of three sets of amino acids, Thr12-Ser14, Ser37-Ser40, and Gly84-Val89 that are located in three different unstructured loops²³. The substrate binding is mediated through interactions between Glu240, Arg267 and Gln161, whereas Arg101 and Lys243 are the phosphate binding sites²⁴.

2.3 Catalytic mechanism

Aspartate semialdehyde dehydrogenase catalyzes the reductive dephosphorylation of the substrate β -aspartyl phosphate into aspartate semialdehyde (Figure 2.2), a key intermediate in the aspartate biosynthetic pathway. A four step sequential mechanism is proposed on the basis of pH and chemical modification studies²⁵, and on high resolution crystal structures of the two intermediates²⁶ formed during the catalytic cycle²⁷.

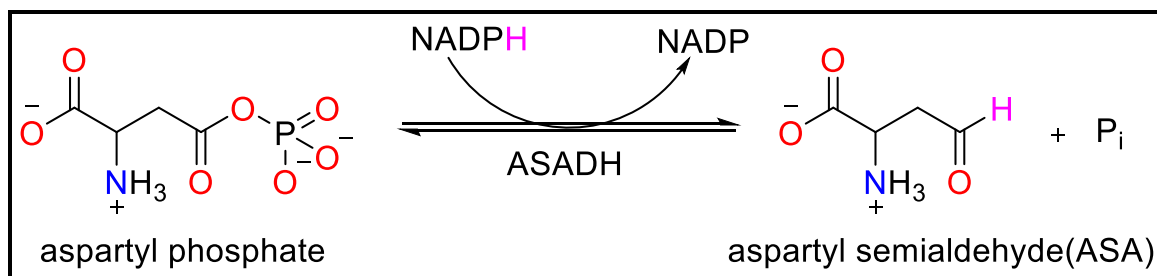


Figure 2.2: ASADH catalyzed reaction in biosynthetic direction²⁸

The proximity of the active site base His274 generates the Cys135 thiolate nucleophile that attacks the electron deficient carbonyl carbon of the substrate aspartyl phosphate (Figure 2.3) (1) to form a tetrahedral intermediate (2), which then collapses with the expulsion of phosphate²⁹. This results in formation of a relatively stable thioacyl enzyme intermediate (3), with hydride transfer to this intermediate from NADPH forming a second tetrahedral intermediate (4). Subsequent collapse of this intermediate *via* expulsion of the enzyme thiolate group produces aspartate semialdehyde. The active site base His274 will protonate the enzyme thiolate group, allowing the enzyme to cycle through the next round of the catalytic cycle. The enzyme exhibit an ordered sequential mechanism based on kinetic analysis, with binding order as NADPH binding first followed by substrate β -aspartyl phosphate and order release of ASA before NADP²⁴ in the physiological direction.

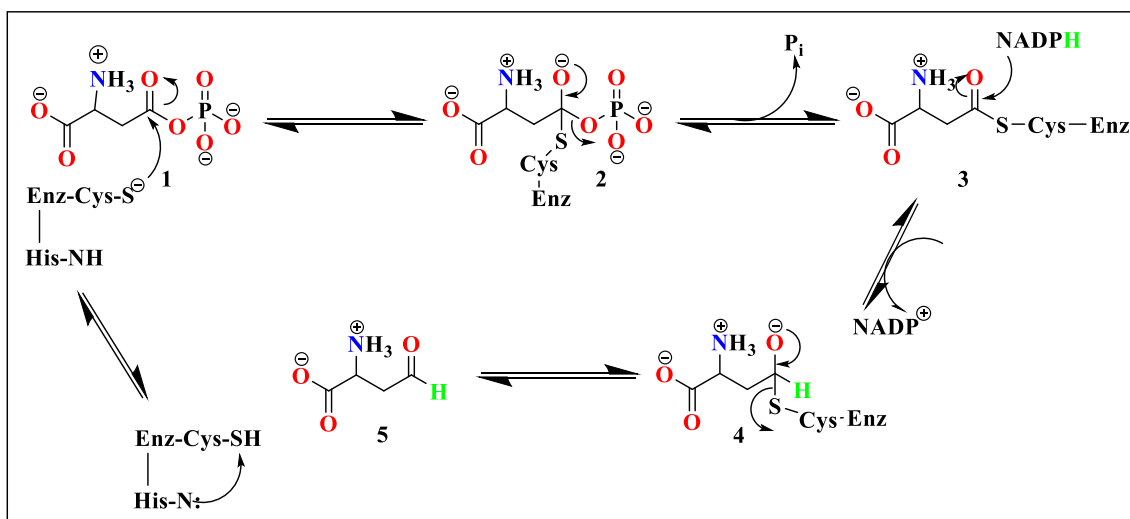


Figure 2.3: Catalytic mechanism of ASADH

2.4 Structure of ASADH

The ASADH structure has been solved from species present in all domains of life; i.e. *Methanococcus janaschii* (archaea)³⁰, *Haemophilus influenza* (bacteria)²⁶, and *Candida*

albicans (fungi)²³. Each monomeric unit is composed of an N-terminal coenzyme-binding domain and a C-terminal catalytic and dimerization domain²³. Although the critical catalytic residues are highly conserved, significant differences have been found in secondary structures among different domain species. The orientation of the active-site nucleophile has been found to be in an alternative conformation in fungal ASADH²³. The α -helical subdomain, which is a part of dimerization interface in bacterial ASADHs, is missing in fungal²³ and archaeal³⁰ forms. The oligomeric state of the fungal ASADHs has been found as a dimer of dimers, whereas bacterial ASADHs existed as a dimer only³¹.

2.5 ASADHs from human fungal pathogens

Four fungal forms and one parasitic protozoan form of ASADHs have been chosen for study, selected on following basis:

- a. These organisms each share less than 25% sequence identity to the most studied bacterial species (*Streptococcus pneumoniae*) and around 50% sequence identity with a fungal species (*C. albicans*)
- b. Sequence alignment of *C. albicans* ASADH with *H. capsulatum* ASADH shows some deletions in the C-terminal domain. Similar sequence alignment of *C. albicans* with *T. gondii* shows deletions in both the N- and C-terminus, as well as a few insertions in the gene sequence.
- c. ASADH structure from parasitic protozoan and basidiomycota fungi have not been solved, and it would be intriguing to know the structural details of the ASADHs from these organisms with large deletions and insertions in the gene sequence.

d. All of the species chosen are human pathogens, and structural information from these novel targets will aid in selective and potent inhibitor design, which will ultimately lead to the development of new antifungal agents.

The wide discrepancies in gene sequences between these selected organisms has served to broaden the scope of our research project. Understanding the differences among these selected enzymes will narrow the targeted species that could be beneficial for drug design. This would also advance the approach of species-specific inhibitor design.

C. neoformans is an encapsulated, basidiomycetous fungal pathogen responsible for causing cryptococcosis³² and cryptococcal meningoencephalitis in immunocompetent as well as in immunocompromised human populations³³. Infections with *C. neoformans* can be fatal if untreated, and even treatment with the most potent antifungals can be fatal if the patient does not have enough T-cell-dependent immune function³³. *Aspergillus fumigatus* is a ubiquitous, saprophytic fungi found both in plants and as a human pathogen, responsible for causing the destructive lung disease chronic pulmonary aspergillosis¹. In addition, this organism is responsible for causing a wide range of other human ailments depending upon the immune system of the host. Mortality rates from *aspergillus* infections range from 40% to as high up to 90% in high risk populations, and also depends upon the site of infection, treatment regimen and immune system of the infected host³⁴. *Blastomyces dermatitidis* is an invasive fungus which causes serious infections in both animals and humans and is responsible for the destructive pulmonary disease blastomycosis. This fungus forms filamentous mycelia in the environment but switches to an infectious yeast form upon contact with the human host. *Toxoplasma gondii*, is a ubiquitous opportunistic pathogen responsible for causing the disease toxoplasmosis³⁵. It is an obligate intracellular

parasite and is one of the most common parasites infecting humans and other warm-blooded animals³⁵. The development of efficacious therapies against such intracellular eukaryotic pathogens is a severe challenge, given the protective location of these pathogens and also their similar biology with the human host³⁶.

2.6 Biophysical characterization of aspartate semialdehyde dehydrogenase

2.6.1 Cloning, expression and purification of ASADH from *Cryptococcus neoformans*

2.6.1.1 Cloning

(Text and figures in this section are adapted from Dahal et. al., Acta Cryst F., 2015)

Cryptococcus neoformans, a causative agent of cryptococcosis, is an encapsulated yeast that can live on plants and animals. Cloning of the *CnASD* gene (CNA02450, 1095bp) encoding aspartate semialdehyde dehydrogenase from *Cryptococcus neoformans* var. *neoformans* serotype D (strain JEC21) was initially carried out using restriction enzyme cloning. Two oligonucleotide primers were designed with Nco I and Xho I recognition sites on the N-terminal and C-terminal, respectively, of a pET28a (+) vector. Forward primer 5'- AAT ATT CCA TGG ATG TCC CCC CGC CCG CAG ATC-3' and reverse primer 5'- GAG TAT CTC GAG CTG GAT CAA ACC CTT CTC GAC CGC AAT CTC G -3' were used to amplify the *CnASADH* gene from the genomic DNA via standard polymerase chain reactions (PCR). The amplified gene and the vector were digested with Nco I and Xho I restriction enzyme, ligated with quick DNA ligase and transformed on *E. coli* DH5 α competent cells. Colonies from kanamycin-resistant LB plates were extracted from a miniprep spin kit (Qiagen) and digested with Sac I (gene cutter) and Apa I (gene + vector cutter) for plasmid confirmation. The integrity of the plasmid was finally confirmed by DNA sequencing (Eurofins).

2.6.1.2 Yeast expression system

The PCR amplified *CnASD* gene was found to have 4 introns on its genomic DNA amplified gene. In order to remove the introns, we transformed our *CnASD* gene into a *Pichia pastoris* cell line (KM71H) due to its splicing properties. EcoRI and XhoI restriction sites were used for sub-cloning into the pPICZa vector under control of a methanol-induced (AOX 1) promoter with C-terminal 6XHis tag selected as expression vector. Ligation was performed between the amplified gene and digested pPICZa vector and transformed into *P. pastoris* KM71H competent cells in Zeocin (light sensitive) resistant plates utilizing standard procedure of Easy Select Pichia Transformation kit (Invitrogen). Positive colonies were grown overnight in low salt LB media (1 g tryptone, 0.5 g NaCl and 0.5 g yeast extract). The plasmid was purified with a plasmid purification kit (Qiagen) and restriction digestion and DNA sequencing was performed to confirm the construct. Despite using the eukaryotic *Pichia pastoris* yeast expression, this system was not able to splice the introns from *CnASD* gene.

2.6.1.3 Gene synthesis

Since the eukaryotic expression was not able to remove the introns, gene encoding *CnASADH* was codon-optimized for *E. coli* expression and was synthesized from Invitrogen utilizing Eco RI and Xho I site at the *N*-terminal and *C*-terminal, respectively, using a pMA-T vector. The optimized gene was ligated into a pET28a(+) vector (Novagen) with a carboxy-terminus hexa-histidine tag using these *NcoI* and *XhoI* restriction sites. The ligated plasmid was transformed into the DH5 α *E. coli* cell line, followed by BL21(DE3) as an expression host and the construct was extracted and purified from kanamycin-

resistant colonies using the Miniprep plasmid extraction kit (Qiagen, USA). The DNA sequence was confirmed by restriction digestion and by DNA sequencing.

2.6.1.4 Pilot expression

The pET28a (+) construct of *CnASADH* was grown in LB media overnight at 310K. The cells were induced when the OD₆₀₀ reaches 0.6-0.8 by using three different concentration of IPTG (0.1, 0.5, and 1 mM) and grown further at two different temperatures (293 K and 301 K). 1 ml of the cell culture was aliquoted at different time intervals (0, 1, 3, 5, 7, 9, and 18 h) and centrifuged. The pellet was dissolved using Bug buster solution (Invitrogen) and centrifuged and insoluble pellet was dissolved in 2% (v/v) Triton X-100 and 50 mM Tris-HCl, pH 5.5. The supernatant from each step was separated and proceeded further for SDS-PAGE and anti-his Western blot protocol. From the pilot expression, the *CnASADH* protein was found to be expressed at 0.5 mM IPTG concentration at 293 K.

2.6.1.5 Protein characterization

The protein band corresponding to the expected size of ASADH was excised from the SDS gel, in-gel reduced, alkylated, destained and proteolytically cleaved with TPCK-treated trypsin (Invitrogen) following a standard protocol³⁷. 2,5-DHB Matrix (10 mg/ml saturated solution) was dissolve in 0.1% trifluoroacetic acid in acetonitrile solution. 1 µL matrix was mixed with 1 µl of digested gel mixture, put in desiccator and dried. The cleaved peptide masses were identified by MALDI-TOF mass spectrometry using a Bruker ultrafleXtreme MALDI-TOF/TOF spectrometer, with a MASCOT database search³⁸ used for confirmation of the protein identity. The exact species and strain of *CnASADH* protein was confirmed by MALDI-MS with protein score of 118 and 47% sequence coverage with

higher confidence ($p < 0.05$) (Figure 2.4).

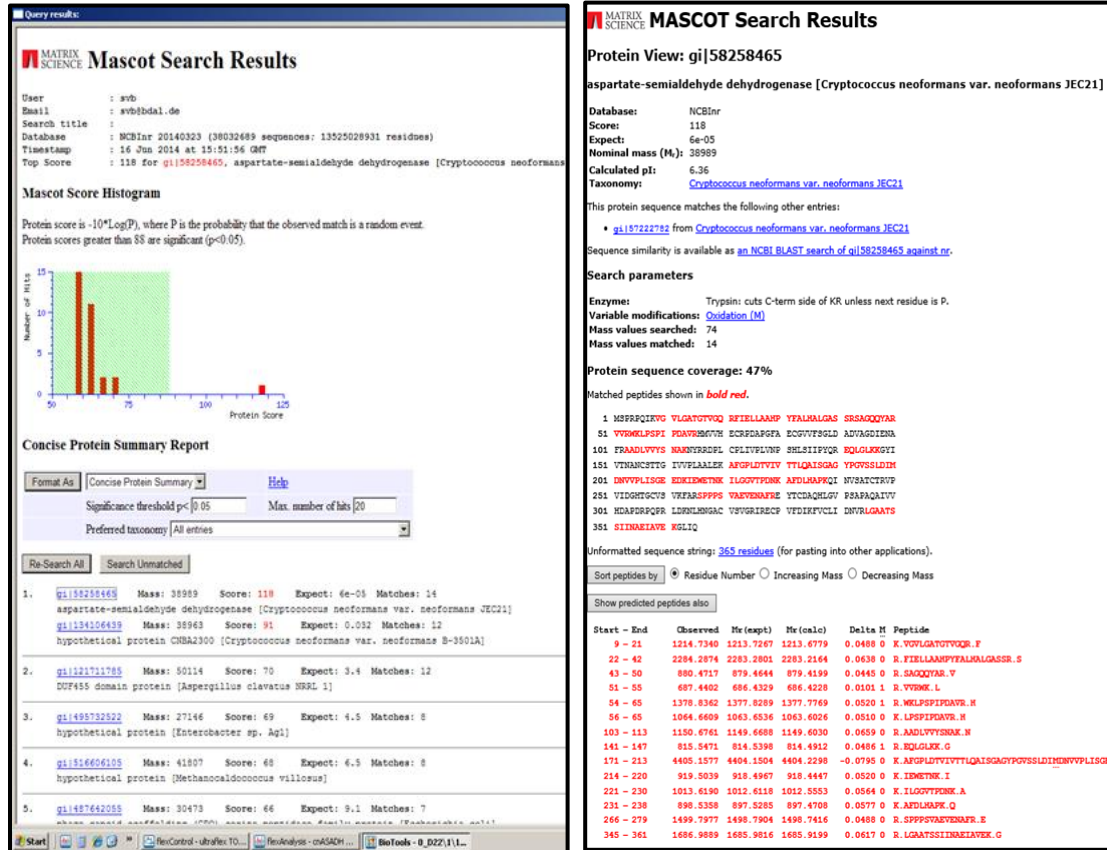


Figure 2.4: Mascot result from in-gel digestion with trypsin from SDS-PAGE of *CnASADH*. The protein identity was confirmed with protein score of 118 and 47% sequence coverage.

2.6.1.6 Protein purification

The transformed cells were grown at 310 K in LB media containing $30 \mu\text{g ml}^{-1}$ kanamycin until an A_{600} of 0.6-0.8 was obtained. Cells were then induced by addition of 0.5 mM IPTG and were grown for an additional 16 h at 293 K (optimum condition for protein expression). Cells were harvested by centrifugation at 17,000 g for 10 min. All protein extraction steps were done at 4 °C unless otherwise specified. The cell pellet (~12 g from 4L) was resuspended in buffer A consisting of 50 mM potassium phosphate, pH 7.2, 200 mM NaCl, 25 mM imidazole, homogenized by a hand homogenizer and subsequently lysed by ultrasonication for total of 8 min at 30 s interval with a Fisher model

550 sonic dismembrator. Cell debris was removed by centrifugation at 12,000 rpm for 30 min and the supernatant was filtered through a 28 mm 0.45-micron membrane syringe filter. The clarified soluble lysate was loaded onto a nickel-nitrilotriacetic acid (Ni-NTA) column and the target protein was eluted by using a 25 mM to 400 mM imidazole gradient. The eluted fractions (Figure 2.5, left) showing catalytic activity and a single band on Coomassie-stained polyacrylamide gel (Figure 2.5, right) were pooled and dialyzed overnight against a buffer consisting of 20 mM HEPES, pH 7.0, 50 mM NaCl, 0.5 mM EDTA and 1 mM DTT. The dialyzed sample was concentrated to 10 mg ml⁻¹ by ultracentrifugation using a 10 kDa MW cut-off spin concentrator (Millipore). The intense peak in the chromatogram before the expected molecular weight of our protein (peak before red rectangle) might be weakly binding protein expressed from *E. coli* and eluted early from the column at lower concentration of imidazole. The protein concentration was measured using a Nanodrop 2000 spectrophotometer and the enzyme was stored at 253 K until used. Stability of protein was checked at three different temperature (277 K, 253 K and 193 K) and effect of DMSO was checked using (0-50%) DMSO concentration.

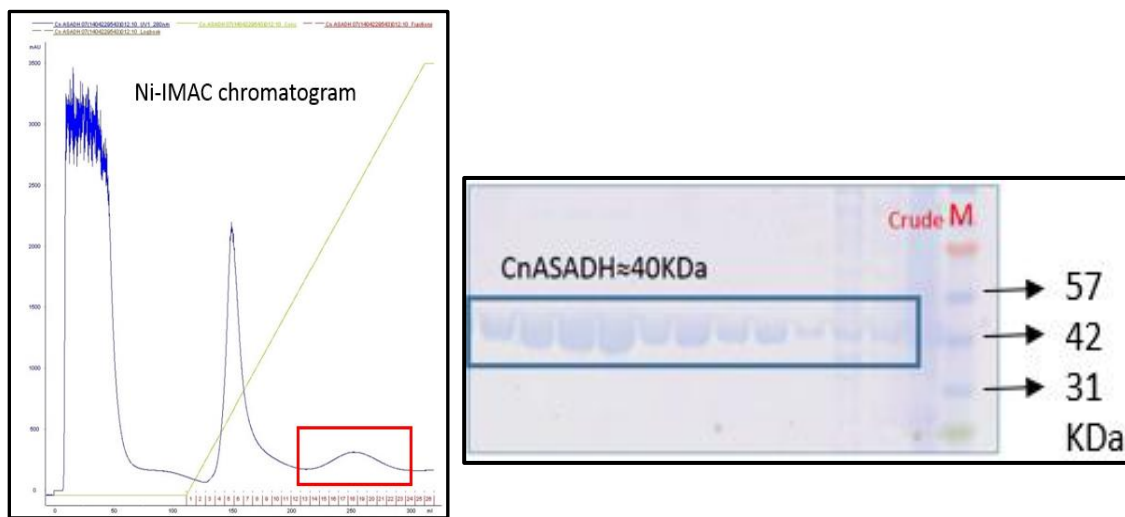


Figure 2.5 Left): Elution profile of *CnASADH* from Ni-IMAC column. Fractions inside the red rectangle shows activity. Right): SDS PAGE profile of eluted fractions.

2.6.2 Cloning, expression and purification of ASADH from *Aspergillus fumigatus*

(Text and figures in this section are adapted from Dahal et al., Acta Cryst F., 2017)

2.6.2.1 Cloning

The gene encoding AfASADH was synthesized from Invitrogen and was ligated using restriction enzyme cloning utilizing the NcoI and XhoI restriction sites of pET28a (+) vector with a C-terminal hexa-histidine tag. The ligated cloning plasmid was transformed into DH5 α *E. coli* cell lines and then further transformed into BL21 (DE3) *E. coli* expression host. The integrity of the plasmid was confirmed by restriction digestion and DNA sequencing. The recombinant construct was expressed in *E. coli* BL21 (DE3) cells by inducing with 0.1 mM IPTG when the OD₆₀₀ reaches between 0.6-0.8 in 4 L of LB media at 293 K supplemented with kanamycin (30 μ g/ml). The temperature was lowered to 289 K and cell were grown for an additional 18 h. The cell paste was harvested by centrifuging at 17000 g for 15 min at 4 °C and stored at -80 °C until use.

2.6.2.2 Protein expression and purification

(A portion of this text is adapted from Dahal et al., Acta Cryst F., 2017)

The frozen cell pellet was suspended in 50 mM potassium phosphate, pH 7.2, 200 mM NaCl, 20 mM imidazole, and 10% (v/v) glycerol (Buffer A) and homogenized by a hand homogenizer. Lysozyme (10 μ M, Sigma) and DNaseI (100 μ M, Sigma) were added to the lysis buffer and incubated on ice for 1 hour. Cells were lysed by ultra-sonication for total of 8 min at 30 s interval with a Fisher model 550 sonic dismembrator. Insoluble protein and other cellular debris were removed by centrifugation at 12,000 g for 40 min and the supernatant was filtered through a 28 mm 0.45-micron membrane syringe filter. The clarified soluble lysate was loaded onto a nickel-nitrilotriacetic acid (Ni-NTA) column

pre-equilibrated with buffer A. The column containing the bound protein was washed with 10 column volumes of buffer A, and the target enzyme was eluted by using a 20 mM to 400 mM imidazole gradient. The protein was further purified using an anion exchange Source 15Q column (GE Healthcare) with a 50 mM to 600 mM NaCl gradient (Figure 2.6, left). Protein purity was analyzed by SDS-PAGE, and the active and pure fractions showing a single band on Coomassie-stained polyacrylamide gel (Figure 2.6, right) were pooled and dialyzed overnight against a buffer consisting of 20 mM HEPES pH 7.0, 50 mM NaCl, 0.5 mM EDTA and 1 mM DTT. Protein concentration was determined by absorbance at 280 nm using a Nanodrop 2000 spectrophotometer and was subsequently concentrated to 40 to 50 mg ml⁻¹ by ultracentrifugation using a 10 kDa MW cut-off spin concentrator (Millipore). The enzyme identity was confirmed by MALDI-MS with 59% sequence coverage (Figure 2.7) and an anti-his Western Blot protocol, and the enzyme was stored at 253 K until used.

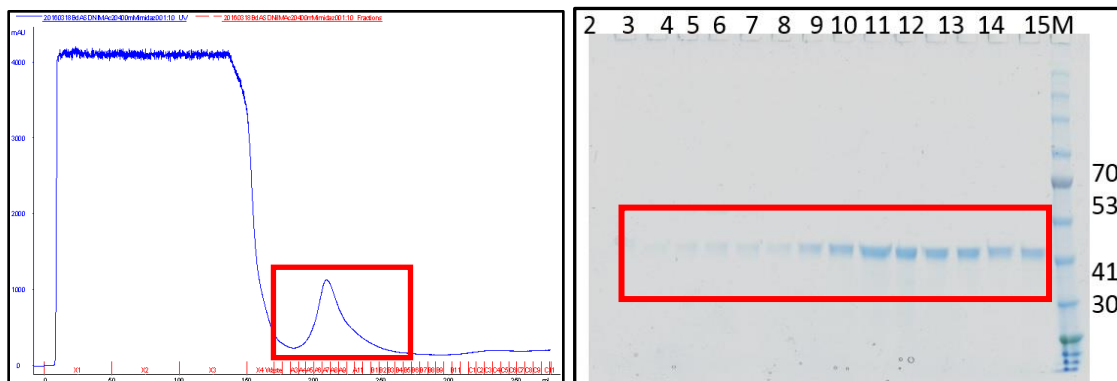


Figure 2.6 Left): Chromatogram profile of *AfASADH* after Source 15Q column using 50 mM – 600 mM NaCl gradient. The fraction inside the red square showed activity. Right: SDS-PAGE profile of eluted fractions, single band \approx 40 kDa corresponding to *AfASADH*, Molecular weight marker (kDa) shown on right side of SDS gel

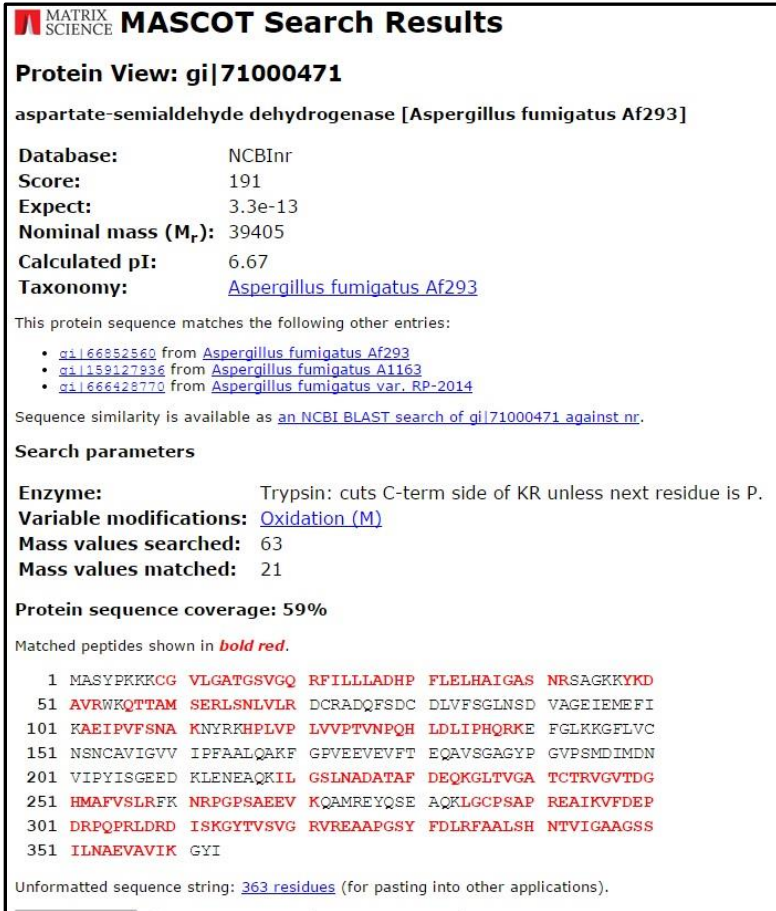


Figure 2.7: MASCOT search result after MALDI-MS of excised gel band of AfASADH. The sequence coverage was found to be 59% with matched peptide highlighted in red.

2.6.3 Cloning, expression and purification of ASADH from *Blastomyces dermatitidis*

2.6.3.1 Cloning, protein expression and purification

The BDCG_01946 gene (Uniprot accession ID: C5GC63, Gene ID: 8509855) encoding full length *BdASADH* enzyme from *Blastomyces dermatitidis* was codon-optimized for *E. coli* expression and synthesized by Invitrogen (Life Technologies). The synthesized gene was ligated between the *NcoI* and *HindIII* restriction sites of pET-28a (+) plasmid (Novagen, USA) to produce an expression construct with a C-terminus hexahistidine tag. The integrity of the ligated plasmid was confirmed by restriction digestion and by DNA sequencing. The recombinant enzyme was expressed in *E. coli* B121 (DE3)

cells during the growth cycle (A_{600} between 0.6-0.8) at 300 K by inducing with 100 μ M IPTG added to the LB media containing 30 μ g ml⁻¹ kanamycin. The temperature was reduced to 289K and cells were grown for an additional 16 h, and then harvested by centrifugation at 17,000 g for 15 min and stored at 193 K. The cell pellet was suspended in 50 mM potassium phosphate, pH 7.2, 200 mM NaCl, 20 mM imidazole, and 10% (v/v) glycerol (Buffer A) and homogenized by a hand homogenizer. Lysozyme (10 μ M, Sigma) and DNaseI (100 μ M, Sigma) were added to the lysis buffer and incubated on ice for 1 h. Cells were lysed by ultra-sonication for total of 8 min at 30 s interval with a Fisher model 550 sonic dismembrator. Insoluble protein and other cellular debris were removed by centrifugation at 12,000 g for 40 min and the supernatant was filtered through a 28 mm 0.45 micron membrane syringe filter. The clarified soluble lysate was loaded onto a nickel-nitrilotriacetic acid (Ni-NTA) column pre-equilibrated with buffer A. The column containing the bound protein was washed with 10 column volumes of buffer A, and the target enzyme was eluted by using a 25 mM to 500 mM imidazole gradient (Figure 2.8). The protein was further purified using an anion exchange Source 30Q column (GE Healthcare) with a 50 mM to 600 mM NaCl gradient. Protein purity was analyzed by SDS-PAGE, and the active and pure fractions showing a single band on Coomassie-stained polyacrylamide gel were pooled and dialyzed overnight against a buffer consisting of 20 mM 4-(2-hydroxyethyl)-1-piperazineethane-sulfonic acid (HEPES) pH 7.0, 50 mM NaCl, 0.5 mM EDTA and 1 mM DTT. Protein concentration was determined by absorbance at 280 nm using a Nanodrop 2000 spectrophotometer and was subsequently concentrated to 40 to 50 mg ml⁻¹ by ultracentrifugation using a 10 kDa MW cut-off spin concentrator (Millipore).

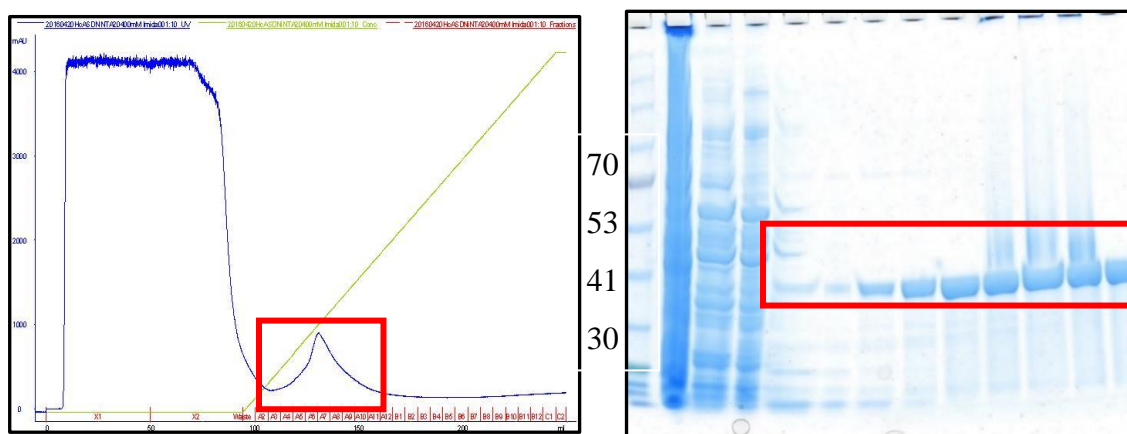


Figure 2.8: (Left) Chromatogram profile After Ni-IMAC column of *BdASADH* using 25 – 400 mM imidazole gradient. Active fractions are shown inside red rectangle. Right: SDS PAGE showing eluted fractions from Ni-IMAC. Thick band \approx 40kDa corresponds to *BdASADH*, Molecular weight marker (kDa) shown on left side of SDS gel.

2.6.4 Cloning, expression and purification of ASADH from *Toxoplasma gondii*

2.6.4.1 Cloning, expression, and purification

The gene encoding the ASADH from *Toxoplasma gondii*, was synthesized from Invitrogen (NY, USA). The gene was cloned into pET28a (+) expression vector containing a C-terminus hexahistidine tag to generate a plasmid coded as TgASADH. Nco I and Xho I multiple cloning sites were used for cloning *TgASADH*. The resulting plasmid with the *asd* encoding gene was then transformed into BL21 (DE3) cells for expression and bulk cultures. Protein expression was carried out in pilot scale using various time, temperature, and IPTG concentrations. Unfortunately, the majority of the protein was found to be expressed in inclusion bodies. The identity of the expressed protein sample was confirmed by Western blotting (Figure 2.11, left) and MALDI-MS from the excised band from SDS-PAGE following in-gel trypsin digestion protocol. The protein species was confirmed by

MASCOT mass search. The sequence coverage for *Tg*ASADH was found to be 22% (Figure 2.9).

Cell paste was resuspended in the lysis buffer (50 mM potassium phosphate, pH 7.2, 200 mM NaCl) and was subsequently lysed by ultra-sonication. The resulting suspension is then centrifuged at 10,000 rpm for 30 min to get the crude ASADH sample. Since the majority of the protein was present in inclusion bodies, urea denaturation process was carried out for solubilization, denaturation and refolding of the protein from inclusion bodies. The supernatant, recovered by centrifugation, was filtered through syringe and protein was eluted by a 50 mM-400 mM imidazole gradient using the Ni-NTA column. The enzyme activity of the eluted fractions and was monitored with the standard ASADH assay.

The insoluble pellet was subjected to serial dilution of urea buffer (6 M urea buffer to 1 M urea buffer) dissolved in 50 mM potassium phosphate, pH 7.2, 200 mM NaCl for solubilization. The fractions from 6 M, 4 M, 2 M and 1 M urea buffer were pooled and dialyzed overnight against gradual decreasing concentration of urea buffer; i.e., 6 M to 4 M to 2 M to 1 M, and finally dialyzed against 20 mM HEPES pH 7.0, 50 mM NaCl, 0.5 mM EDTA and 1 mM DTT. Fractions after dialysis from 2 M and 1 M urea buffers were found to be active. Also, the protein was precipitated while dialyzing with decreasing concentration of urea buffer when using either 6 M or 4 M urea. The dialyzed fractions were eluted with a 40-200 mM imidazole gradient using a Ni-IMAC column (Figure 2.10, left). The majority of the protein fractions dialyzed from 2 M and 1 M urea was found to be the correct size of ASADH from the SDS-PAGE profile, but there were still contaminating protein bands in a small proportion above and below the expected molecular

weight of *Tg*ASADH (Figure 2.11). These fractions were further purified using a 50 mM – 600 mM NaCl gradient from an anion exchange source 30Q column (Figure 2.10, right). The protein sample was found to be about 95% pure after anion exchange column but, unfortunately, the fractions didn't show any enzymatic activity.

MATRIX SCIENCE MASCOT Search Results

Protein View: gi|237836951

aspartate-semialdehyde dehydrogenase, putative [Toxoplasma gondii ME49]

Database: NCBIInr
Score: 68
Expect: 0.079
Nominal mass (M_r): 42653
Calculated pI: 5.67
Taxonomy: [Toxoplasma gondii ME49](#)

This protein sequence matches the following other entries:

- [gi|527313345](#) from [Toxoplasma gondii ME49](#)
- [gi|557737251](#) from [Toxoplasma gondii VEG](#)
- [gi|672258713](#) from [Toxoplasma gondii p89](#)
- [gi|672264378](#) from [Toxoplasma gondii GAB2-2007-GAL-DOM2](#)
- [gi|672558790](#) from [Toxoplasma gondii VAND](#)
- [gi|672567678](#) from [Toxoplasma gondii MAS](#)

Sequence similarity is available as [an NCBI BLAST search of gi|237836951 against nr.](#)

Search parameters

Enzyme: Trypsin: cuts C-term side of KR unless next residue is P.
Variable modifications: [Oxidation \(M\)](#)
Mass values searched: 27
Mass values matched: 7

Protein sequence coverage: 22%

Matched peptides shown in **bold red**.

```

1  MEAAGRDDHQ  FTSARKKRA  PTLSCERKVN  VGILGATGAV  GQRFVSLHGH
51  HPYFRITAVA  ASARSAGKAY  GDVVEWRLLD  TAPLTDEIRG  MTVIRCEPDL
101  FREKGCVIIF  SALDAAAATE  LESLFAASGF  MVFSNAKSHR  MDADVPIILLP
151  YVNAPLLDGV  RSQPHYSKTG  GAIVTNSNCA  SAGISVALKP  LLDKWGAIARL
201  SIATLQAISS  AGYPGLSALD  MIDNVIPHIS  GEEKLESEP  QKILGTLSDG
251  STRITSATFE  SVAMCHRVPV  IDGHIVTVTV  DFPPSTFPNS  ANPDTVSTQV
301  SAALRGFRFP  PNVAELPSCP  DEVLFSFASI  QTGPNRALID  CVGEEWQYLL
351  APSRLNMLPV  PPPGQSSRR  LCGWMFDSER  GTGPEKRSGF  VARWDVSES

```

Figure 2.9: MASCOT search result after MALDI_MS of excised gel band of *Tg*ASADH. The sequence coverage was found to be 22% with matched peptide highlighted in red.

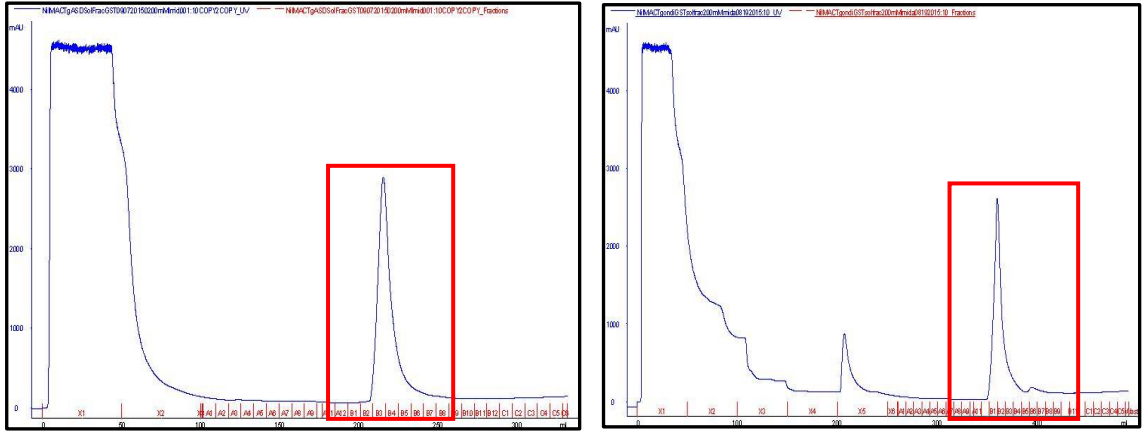


Figure 2.10: Left) Chromatogram profile after Ni-IMAC of *TgASADH* using a 40 mM – 200 mM imidazole gradient. Right: Chromatogram profile after Source 15Q of *TgASADH* using a 50 mM – 600 mM NaCl gradient. The fractions inside the red rectangle showed the pure fractions corresponding to *TgASADH*.

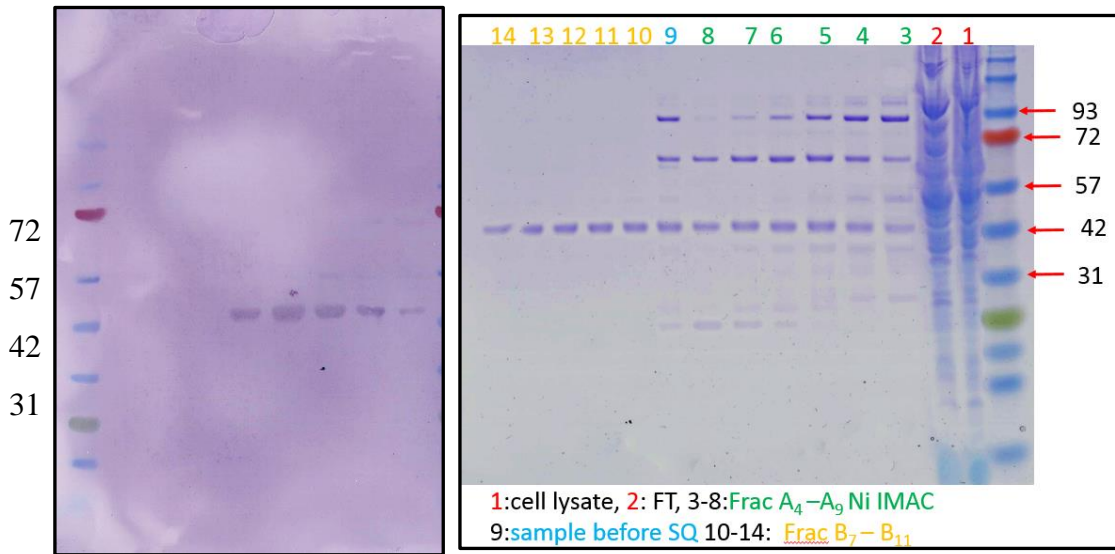


Figure 2.11: Left) Protein bands blotted against anti-His antibody from soluble fractions of *TgASADH* sample. Right: SDS-PAGE profile after Ni-IMAC and Source 15Q fractions of *TgASADH* sample. The right most lane shows the standard molecular weight marker (kDa).

2.6.4.2 GST fusion cloning of *TgASADH*

From pilot scale expression, most of the protein was found to be expressed in inclusion bodies from *TgASADH*. So, a new construct was designed in order to get the protein into a soluble fraction by using the solubilizing proteins, GST and MBP, as fusion partners. The gene encoding *TgASADH* was previously cloned into a pET28-a (+) vector using NcoI and XhoI restriction sites. The gene was cut and paste using ligation-dependent cloning using the same restriction sites into pET41a (+) vector to make a GST fusion construct (GST-His-enterokinase site-POI-His) with the aim to get the protein into the soluble fraction. The gene was successfully cloned into pET41a vector and the sequence was confirmed by DNA sequencing. The GST-fusion construct of *TgASADH* was grown in LB media overnight at 310 K. The small-scale protein expression was carried out at various time interval using different IPTG concentration and growth temperature. Although various attempts have been made varying IPTG concentration and temperature, the protein band corresponding to *TgASADH* (41 kDa) fused with the GST tag (26 kDa) was not found by Western blot protocol. The soluble lysate was purified by Ni-IMAC column using a 20 - 400 mM imidazole gradient. The protein band corresponding to the fusion construct were treated with enterokinase in order to cleave the GST tag and get the native protein. 5 μ L of enterokinase (1unit/ μ L) was added to 8 ml of fusion protein (0.55 mg/ml) and incubated overnight, both at room temperature and also at 4 °C with 10 mM Tris, pH 8.0, and 10 mM CaCl₂ buffer. The enterokinase-treated sample was dialyzed and monitored for enzymatic activity. The protein sample didn't show any enzymatic activity after eluting from Ni-IMAC column and enterokinase treatment. The GST fusion construct was attempted to be purified by using a GST resin column using a 0-10 mM reduced

glutathione gradient using the same buffer used in Ni-IMAC purification. However, none of the eluted fractions from the GST column corresponded to the correct molecular weight of the fusion construct, and these fractions were also not active (Figure 2.12).

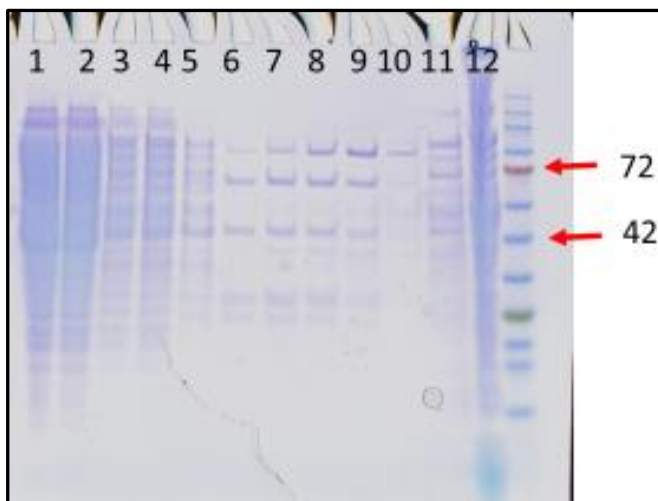


Figure 2.12: SDS-PAGE profile of eluted fractions after GST column of *TgASADH* using 0–10 mM reduced glutathione gradient. None of the fractions showed activity, Molecular weight marker (kDa) shown on right side of SDS gel.

2.6.4.3 MBP fusion cloning of *TgASADH*

Since we were not able to get pure protein from GST fusion construct, an MBP fusion construct was designed with the aim of getting the protein into the soluble fraction. Two PCR primers (Forward: AAGTC GGA TCC ATG GAG GCA GCA GGT CGT GAT GAT and Reverse: GCTAGG CTC GAG CTA GCT TTC GCT AAC ATC CCA ACG) were designed with BamHI and Xho I sites on N- and C-terminus, respectively. The gene was PCR amplified and ligated with MBP fusion pET28a(+) vector (His-MBP-precission protease site-BamHI-*TgASADH*-STOP codon-XhoI). The ligated construct was transformed into the DH5 α cell line followed by the BL21 expression cell line. The

expression construct was confirmed by restriction digestion and DNA sequencing. The *TgASADH* was purified using Ni-IMAC column, followed by a Source 15Q column. SDS-PAGE of the eluted fractions showed other interfering bands above and below the expected molecular weight after Ni-IMAC profile. Those interfering bands were removed by an anion exchange column and a clear single band of approximately 80 kDa was shown on SDS-PAGE profile. The protein was also purified with an amylose column with a 0-10 mM maltose gradient utilizing the affinity of maltose with the MBP tag. The SDS-PAGE profile obtained after amylose column is shown in Figure 2.13. Unfortunately, the eluted fractions from the amylose column didn't show measurable enzymatic activity.

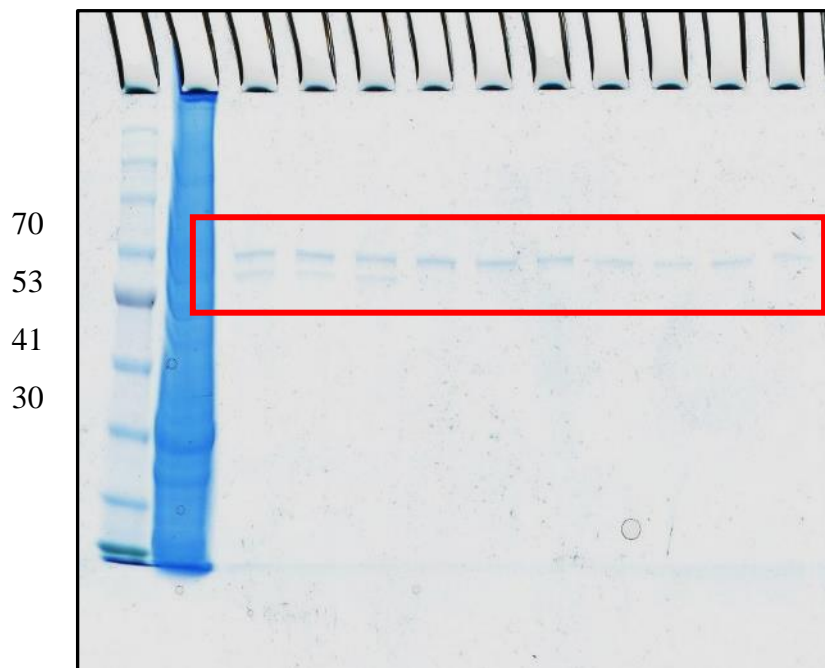


Figure 2.13: SDS-PAGE profile after amylose column of *TgASADH* using a 0 to 10 mM maltose gradient. Molecular weight marker (kDa) shown on left side of SDS gel. The expected molecular weight of the *TgASADH*-MBP fusion protein (82 kDa) is shown inside the red rectangle.

2.6.4.4 *T. gondii* ASADH alternative purification protocol

Several attempts to get purified proteins from *T. gondii* didn't yield any active protein. This modified inclusion bodies extraction protocol was followed with an aim of obtaining active protein. A new protocol ³⁹ was followed with some slight modifications for purification of *T. gondii* ASADH from inclusion bodies. 5 g of cell pellets was resuspended in Buffer A (10 mM Tris/HCl, pH 8.0) and lysed using a hand homogenizer. The lysate was centrifuged at 10,000 g for 30 min at 4 °C, and the inclusion body pellet was washed three times in Buffer B (10 mM Tris/HCl pH 8.0, 0.2 mM phenylmethanesulfonyl fluoride (PMSF), 1% Triton X-100 and once in Buffer C (10 mM Tris/HCl pH 8.0, 0.2 mM PMSF). The final pellet was solubilized in Buffer D (10 mM Tris/HCl pH 8.0, 8 M urea, 10 mM dithiothreitol, 0.2 mM PMSF) for 30 min at 4 °C while mixing by axial rotation. Different concentration of urea samples (6 M, 4 M and 2 M) was used to solubilize the final pellet. The protein solution was then clarified by centrifugation at 30,000 g for 30 min at 4 °C. 30 mg of denatured protein was diluted into 0.5 L of refolding solution containing 100 mM Tris/HCl pH 8.0, 400 mM L-arginine/HCl, 2 mM EDTA and 3 M urea for urea sample in 8 M, 6 M and 4 M. The refolding solution was also prepared with no urea for refolding of the sample that was denatured in 2 M urea. Both refolding mixture was incubated at 4 °C for 24 h with vigorous stirring and then subjected to dialysis against 5 L of Buffer A with four buffer changes over a period of 24 h. Tris/HCl pH 8.0, NaCl and imidazole were added to the final concentrations of 20, 500 and 20 mM, respectively, and the sample was loaded onto a 20 ml Co-IMAC column pre-equilibrated with Buffer E (20 mM Tris/HCl pH 8.0, 500 mM NaCl, 20 mM imidazole). The column was washed with 50 ml of the same buffer and protein was eluted with Buffer F (20 mM

Tris/HCl pH 8.0, 500 mM NaCl, 500 mM imidazole). The protein eluted from Co-IMAC column was analyzed by SDS-PAGE and checked for enzymatic activity with the standard ASADH assay. Unfortunately, none of the eluted fractions showed measurable enzymatic activity.

2.6.4.5 Other purification strategies

A Cation exchange column with a 50-600 mM NaCl gradient was employed for purification of the MBP construct, using a 1 ml DEAE (GE healthcare) column. Hydrophobic chromatography was also performed using either octyl-sepharose or phenyl-sepharose columns with a 1.7 M AmSO₄ to 0 M gradient in phosphate buffer, pH 7.4. The MBP fusion protein sample, after purification on a source Q column, was proceeded to a SP sepharose column with elution by a 50-600 mM NaCl gradient (Cation Exchange column). In all of the cases, the eluted protein was found to be pure in these different purification protocols, but none of the purification strategies yielded an enzymatically active protein.

2.6.5 Cloning, Expression and Purification of ASADH from *Histoplasma capsulatum*

The organism *H. capsulatum* is the causative agent of histoplasmosis, and the *asd* gene from *H. capsulatum* has a 30 amino acid deletion from the C-terminus. This difference makes it important to study this target from a structural perspective. The gene encoding the ASADH from *Histoplasma capsulatum* was synthesized from Genscript (NJ, USA). The gene was cloned into the pET28a(+) expression vector containing a C-terminus hexahistidine tag to generate a plasmid coded as *HcASADH*. The resulting plasmid with *HcASADH* gene was then transformed into BL21(DE3) cells for expression and bulk cultures. To prepare the bulk cultures, a single colony from the transformation was

introduced into a 50 mL LB broth, grown overnight at 310 K with 250 rpm shaking. This starter culture was used to inoculate four 1L bulk cultures. The cultures were incubated at 310 K and 250 rpm until it reaches an OD₆₀₀ of 0.6 to 0.8, after which the cultures were induced with various concentration of IPTG. The level of *HcASADH* protein expression was examined using various temperatures (293 K, 297 K, 301 K) and IPTG concentrations (0.1, 0.5 and 1 mM) in a pilot scale expression. From the pilot scale expression, it was found that majority of the protein was expressed in inclusion bodies. Various attempts to extract and refold the protein from inclusion bodies was adopted in order to yield soluble *HcASADH* protein.

2.7 Biochemical assay of ASADHs

(The text and figures in this section were adapted from Dahal et. al., SLAS Disc., 2018)

Due to the instability of the substrate aspartyl phosphate, the enzymatic activity assay was carried out in the non-physiological direction to measure the increase in absorbance of NADPH at 340 nm ($\epsilon_{340} = 6220 \text{ M}^{-1}\text{cm}^{-1}$) using a CARY UV-visible spectrophotometer (Figure 2.14). Assay was performed in a 1 mL Quartz cuvette using an assay buffer containing a final concentration of 20 mM phosphate, 1.5 mM NADP, 0.3 mM ASADH, 120 mM N-cyclohexyl-2-aminoethanesulfonic acid (CHES) buffer, pH 8.6 and 200 mM KCl. The enzyme was added to initiate the reaction to the final concentration of 0.08 mg ml⁻¹. Enzyme activity of the crude sample and fractions were monitored with the standard ASADH assay. The increase in absorbance of NADPH corresponds to the increase in formation of the product aspartyl phosphate by phosphorylation of substrate ASA in the non-physiological direction (Figure 2.15, left). Because the enzymatic activity was initially monitored at a lower wavelength (340 nm), a set of screened compounds showed

background absorbance at this wavelength which interfered with the rate measurement. To avoid this interference an alternative assay was developed to shift the wavelength to the visible region by using a coupled enzyme assay where phenazine methosulfate (PMS), an electron carrier from NADPH, will reduce iodonitrotetrazolium (INT), an internal dye, to a wine red colored compound formazan which absorbs at 500 nm with a screening assay quality coefficient (Z' factor)⁴⁰ of 0.82. This assay was conducted either in a CHES buffer (pH 8.6), containing 200 mM KCl and 20 mM phosphate or phosphate buffer containing 50 mM potassium phosphate and 200 mM NaCl, 1.5 mM NADP, 0.3 mM ASA, 0.5 mM INT and 0.1 mM PMS. The enzymatic assay was initiated by adding 30 μ L of 0.05 mg/ml ASADH in 200 μ L total reaction mixture and monitored the increase in absorbance of formazan at 500 nm (Figure 2.15, right). This assay will assist in high throughput screening of compound libraries against our enzyme in order to identify initial hits that can be further optimized for lead molecule development. This assay (Figure 2.16) was used to screen compound libraries that contained a significant fraction of UV-absorbent compounds that would potentially interfere with the standard assay at 340 nm.

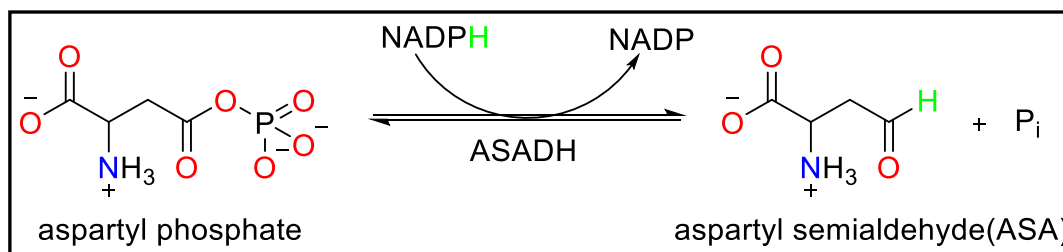


Figure 2.14: ASADH catalyzed reaction in biosynthetic direction²⁸

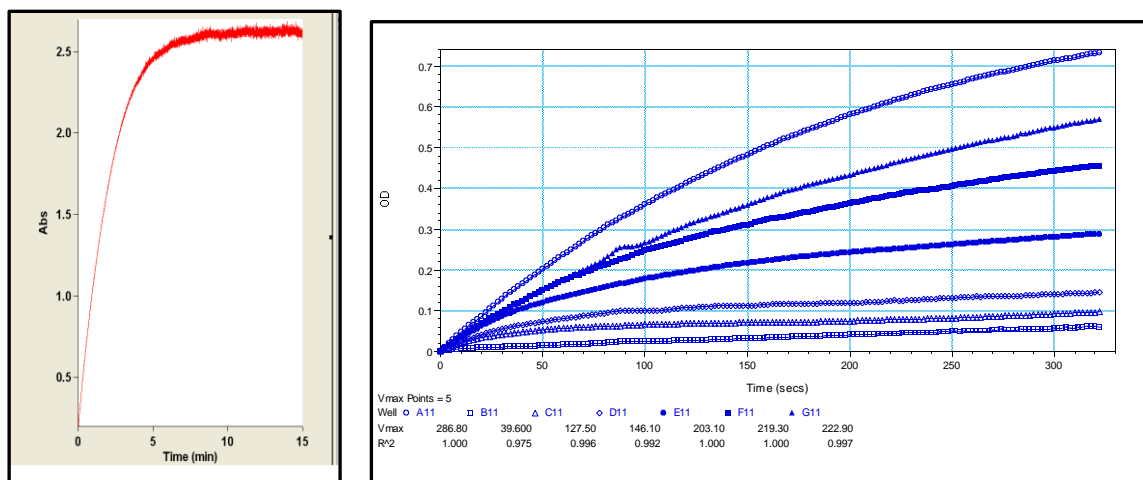


Figure 2.15: (Left) Graph showing increasing absorbance of NADPH on standard enzymatic assay for calculation of specific activity. Right: Increase in signal due to increase in absorbance of formazan at 500 nm for the coupled enzymatic assay of ASADH at increasing concentrations of L-ASA.

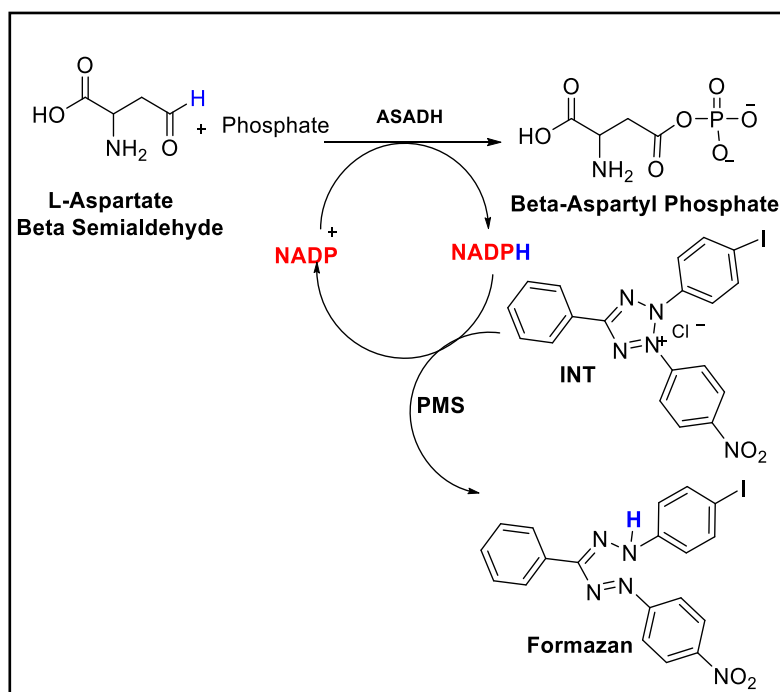


Figure 2.16: Coupled enzymatic assay of the reaction catalyzed by ASADH. Because the reduced cofactor (NADPH) absorbs in a region (340 nm) that is obscured by some of the organic library compounds the reducing potential of NADPH is used to reduce iodonitrotetrazolium (INT) to formazan (500 nm) using phenazine methosulfate (PMS) as an electron carrier. This assay moves the activity read-out into the visible wavelength region, away from the absorbance of most of the organic compounds in these libraries.

2.8 Kinetic parameters for the reaction catalyzed by ASADH

The kinetic parameters K_m , k_{cat} , and k_{cat}/K_m for each enzyme for the substrate aspartate semialdehyde (Table 2.1) was determined following increase in absorbance of NADPH at 340 nm.

Table 2.1 Kinetic parameters catalysed by different forms of ASADH

Enzyme ASADH	Substrate	K_m (mM)	k_{cat} (s^{-1})	k_{cat}/K_m ($s^{-1}M^{-1}$)
<i>C. neoformans</i>	aspartate semialdehyde	0.34	10.2	3.01×10^4
<i>A. fumigatus</i>	aspartate semialdehyde	0.29	6.1	3.1×10^3
<i>B. dermatitidis</i>	aspartate semialdehyde	0.54	13.8	2.56×10^4

While the sequence similarity between different fungal ASADHs is about 55%, and decreases to about 20% with the bacterial ASADHs, the critical catalytic residues are conserved throughout the entire ASADH family⁴¹. Despite this conservation, the kinetic parameters are found to vary significantly among members of the bacterial and fungal ASADHs. The k_{cat} of CnASADH is $10.2 s^{-1}$ and the K_m for the native substrate ASA is 0.34 mM, with a catalytic efficiency of $3.01 \times 10^4 s^{-1} M^{-1}$, whereas the k_{cat} for CaASADH is only $0.12 \pm 0.01 s^{-1}$ ²³. CnASADH shows about an 85-fold higher k_{cat} values compared with CaASADH, and still shows 5-fold higher values than the Gram-positive ortholog, *S. pneumonia* ASADH ($k_{cat} = 2 s^{-1}$)²⁷ and 2.5-fold higher values than the archaeal ortholog *M. jannasschii* ($k_{cat} = 4 s^{-1}$)³⁰. The k_{cat} and K_m values for the native substrate ASA was found to be $6.1 s^{-1}$ and 0.29 mM, respectively, for AfASADH. This k_{cat} value is 50-fold higher than that of CaASADH, but is similar to the values measured for CnASADH ($10.2 s^{-1}$)⁴¹ and for TrASADH ($16.5 s^{-1}$)³¹. In contrast to these similarities with the other fungal ASADHs, the k_{cat} for the bacterial ASADHs vary from $610 s^{-1}$ for the *E. coli* enzyme, 100-

fold higher than for *Af*ASADH, to as low as 58 s^{-1} for one of the ASADH forms from *V. cholerae*⁴². These wide differences in catalytic efficiencies are likely a consequence of the changes in quaternary structures between the fungal and bacterial enzyme forms, and also differences in the nature of the subunit-subunit interactions. The different environmental and evolutionary requirements for the survival of this specific pathogen also likely play a role in these kinetic differences. This higher catalytic activity in *Cn*ASADH suggests that there should be some conformationally favourable interactions in active site when the substrate is bound or may be the specific requirement of this particular fungal pathogen from evolutionary point of view.

2.9 Kinetic screening

2.9.1 Fragment library screening

(The text and figures in this section are adapted from Dahal et. al., SLAS Disc., 2018)

Fragment-based drug discovery has gained significant popularity in the field of drug design in the last decade.⁴³ Several marketed drugs, such as ABT-263 (an inhibitor of B cell lymphoma 2) and ABT-518 (a matrix metalloprotease inhibitor) from Abbott Laboratories, AT7519 (cyclin-dependent kinase 2 inhibitor), AT9283 (serine/threonine kinase inhibitor) from Astex Therapeutics, and LP261 (tubulin inhibitor) from Locus, were each developed from compounds initially identified through a fragment-based drug screening approach.⁴⁴

Traditional compound library screening relies on very large library sizes to increase the likelihood that compounds which were developed against specific drug targets will show some affinity against a new target. Given the vastness of chemical space and the narrow diversity of most compound libraries, even the largest libraries will be able to sample only a miniscule fraction of that space. By contrast, the fragment-based drug development

strategy uses low molecular weight compounds as a starting point for lead compound generation, with the goal of identifying sub-sites where these fragments will bind with at least moderate affinities. There are significantly fewer possible chemical structures as the number of atoms is decreased. So, despite the much smaller library sizes, fragment libraries can lead to improved coverage of their chemical space. A limitation of this approach is that the fragment library components are relatively small compounds possessing few functional groups and limited drug-like properties. However, these hits can be rapidly expanded and optimized to produce effective lead compounds. Compound optimization, either through the coupling of fragments that bind in adjacent sites or by the elaboration of these core structures, is then used to develop these initial hits into advanced lead compounds. Any hits obtained from fragment library screening will typically have low binding affinities (mid to low millimolar), but their selection for further development is based on their high ligand efficiency value,⁴⁵ which is defined (eq. 1) as the free energy of binding of a ligand (ΔG in kcal/mol) per ligand heavy (non-hydrogen) atom.

$$\text{Ligand efficiency (L.E.)} = -\Delta G/N_{(\text{no. of non-hydrogen atoms})} \quad (1)$$

Generally, for a hit to be a useful starting point for drug development, its ligand efficiency should be 0.3 or higher, with the goal of maintaining this value during inhibitor optimization. This ligand efficiency metric is used as the selection criteria to guide the development of initial inhibitors into advanced lead compounds.

2.9.1.1 Water and DMSO-soluble fragment library preparation

The water-soluble and DMSO-soluble libraries were assembled using commercially available low molecular weight compounds dissolved in either water or DMSO, with some pH adjustment as needed to solubilize acids or bases. The water-soluble

library consists of 384 compounds from four different classes: amino acids and derivatives, metabolites and analogs, carbohydrates and bases, and water-soluble organics and aromatics. Similarly, the DMSO-soluble organic fragment library also consists of 384 compounds from four different classes: benzene derivatives, five-membered heterocycles, six-membered heterocycles, and fused/multiple ring systems.⁴⁶

2.9.1.2 Constrained analog and drug library preparation

The constrained analog library was compiled using aspartic acid-based analogs that mimic the core ASA substrate structure. This library contains 83 compounds consisting of 5-6 membered heterocycles, isoxazoles, amino acid analogs, halo acids, pyrazoles, and pyrrolidine derivatives with average molecular weight of 173 Da, with compounds ranging from 111 to 282 Da. These compounds were prepared by dissolving in DMSO at 200 mM stock concentrations and were tested at 1 mM initial concentrations. Many of the compounds in this library contain novel chemical scaffolds when compared to our fragment libraries, increasing the probability of finding novel starting points. The NIH clinical collection library consists of 726 compounds supplied in 96-well plates prepared in DMSO solution at a stock concentration of 10 mM (http://www.nihclinical-collection.com/product_info.php). Since most of the compounds from the NIH clinical collection have already been through pre/clinical trials⁴⁷, these drug-like candidates have a greater possibility of development as antifungal drugs. These compounds have highly developed properties of drug-likeness such as bioavailability and stability. They also exhibit well-characterized safety profiles as they have been used in humans. So, we expect the overall hit rate from this library will be higher compared to other raw chemical libraries. The Prestwick library consists of 1320 drugs and drug candidates supplied in 96-well plates

dissolved in 50% DMSO/water at a concentration of 1 mM. 10 to 20 μ l of each inhibitor was transferred to 200 μ l solution of assay recipe to give final concentration of 100 to 500 μ M for each compound.

ASADH was found to retain at least 70% of its enzymatic activity at DMSO concentrations as high as 50%, allowing the screening of organic compounds with low water solubility in a DMSO/water mixture. The average molecular weight of the compounds in these libraries is \sim 160 Da, with 90% of the compounds between 90 and 260 Da. The majority of the compounds obey the general fragment library rules:⁴⁸ (i) heavy atoms count \leq 22; (ii) clogP $<$ 3; (iii) number of H-bond donors \leq 3; (iv) number of H-bond acceptors \leq 3; (v) number of rotatable bonds \leq 5, with only a few exceptions. Initial screening was conducted using cocktails of four compounds, one from each category, resulting in 96 fragment cocktails. The pH was adjusted to 8-9 by titrating with sodium hydroxide or hydrochloric acid before screening. The reactions were monitored in a 96-well plate by using SpectramaxR 340PC Microplate Spectrophotometer with Softmax Pro software (Molecular Devices, Sunnyvale USA) to improve the screening efficiency. Some compounds from the organic fragment library produced strong absorption that interfered with our assay at 340 nm and led to false positive readings. So, the alternative coupled assay at 500 nm was used to screen these highly absorbing compounds. Compounds that showed less than 20% of the initial rate compared to control reactions without inhibitors are arbitrarily classified as good inhibitors and also for easier classification of stronger and weaker inhibitors. Cocktail fragments that showed inhibition were then screened individually at 2 mM concentration to specify the inhibitor among the mixture of

compounds. Dixon analysis⁴⁹ was used to calculate inhibition constant (K_i values) in which the inhibitor is assumed to compete with one of the substrates for binding to the enzyme.

2.9.2 Results and discussion

Previous studies have developed inhibitors against bacterial ASADH⁵⁰⁻⁵² as potential antibacterial agents, but the development of antifungal inhibitors against this target has not yet been investigated. Two focused fragment libraries with chemical class diversity were screened to identify initial inhibitors against representative members of the fungal ASADH family. A water-soluble and a DMSO-soluble library were screened in 96 four-compound cocktails at 2 mM initial concentrations. We classified the inhibitors classes in house such as cocktails showing $\leq 20\%$ initial velocity compared to the control reaction were classified as containing strong enzyme inhibitors, those showing 20-50% as moderate, and those with $>50\%$ as weak/non-inhibitors. These libraries were initially screened against four fungal enzyme forms (*Ca*ASADH, *Af*ASADH, *Cn*ASADH, and *Bd*ASADH) and one bacterial form (*Sp*ASADH) as a selectivity control. Five of the water-soluble fragment library cocktails showed strong inhibition and five showed moderate inhibition (Figure 2.17A), whereas seven organic fragment library cocktails showed strong and fifteen showed moderate inhibition against all fungal forms of ASADH (Figure 2.17B). A total of 160 cocktails (640 compounds) from both libraries showed little or no significant inhibition against these enzymes and were eliminated by this preliminary screening.

2.9.2.1 Inhibitor identification from library screening

Compounds from each cocktail hit were then screened separately, yielding five compounds from the water-soluble library and 13 from the DMSO-soluble library that showed good inhibition against several fungal ASADHs, resulting in overall hit rates of

1.3% and 3.4%, respectively. Because these library compounds can bind with low selectivity to different enzyme targets the hit rates are higher than is typically seen for HTS library screening. An aspartic acid analog library composed of 83 rotationally constrained substrate analogs was also assembled and tested. Screening of this analog library yielded three strong hits and three moderate hits against the *C. albicans* form of ASADH.

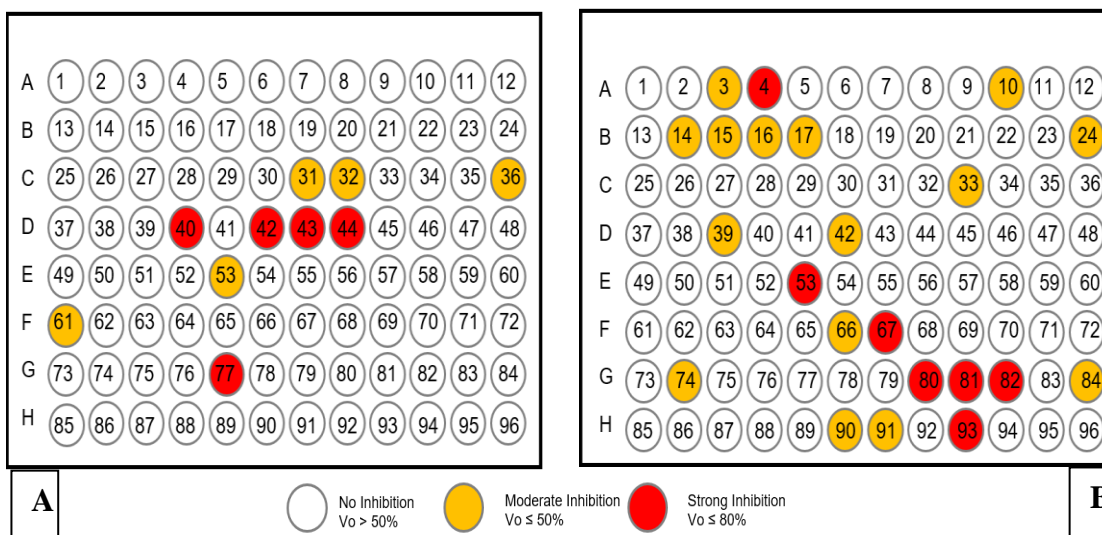


Figure 2.17: Fragment library screening against *Candida albicans* (*Ca*ASADH), *Cryptococcus neoformans* (*Cn*ASADH), *Aspergillus fumigatus* (*Af*ASADH), and *Blastomyces dermatitidis* (*Bd*ASADH) in a 96-well plate format. (A) water-soluble fragment library, (B) DMSO-soluble fragment library. Each well consists of cocktail of four compounds, one from each structural class from the respective libraries. Cocktails that showed strong inhibition ($\leq 20\%$ activity) against all four fungal forms are shown in dark shading, moderate inhibition ($\leq 50\%$ activity) in light shading and cocktails showing little or no inhibition ($> 50\%$ activity) are shown with no shading. The relatively small number of wells showing strong inhibition allows a rapid identification of the best enzyme inhibitors from this screen.

2.9.2.2 Selectivity of initial fungal ASADH inhibitors

Inhibition constants (K_i values) were determined for each inhibitory compound, initially against the *C. albicans* form of ASADH, to analyze their potency. Compounds with K_i values less than 1 mM and with high L.E. values were considered as promising starting points for further elaboration. To evaluate fungal ASADH selectivity inhibitor potency was next evaluated against four different fungal orthologs, and also checked against a representative bacterial ASADH. These fungal ASADHs share ~55% sequence similarity, but only about ~25% sequence similarity to their bacterial counterparts. Despite the highly conserved catalytic residues across the ASADH family, and nearly identical active site architecture, several inhibitors show selectivity between the bacterial and the fungal species, and some compounds also showed selectivity between the ASADHs from different fungal species. Some compounds are non-selective inhibitors; for example, catechol, benzene-1,3,5-triol and cyclohexyl iodide show similar potency with both the fungal and bacterial enzymes (Table 2.2, section a). Several fungal inhibitors have little inhibitory activity against the bacterial ASADH, but show 4-fold or greater potencies against each of the fungal enzymes (Table 2.2, section b). Some compounds show preferential inhibitor selectivity for one of the fungal ASADHs, with 2- to 7-fold greater potency relative to the other fungal enzyme orthologs (Table 2.2, section c, bold entries). These results suggest that subtle differences in the nature of the substrate binding pocket may lead to differences in potency and selectivity of these inhibitors between these different enzyme forms. While these selectivities are still fairly modest, these lead compounds will be used as starting points for the optimization of species-selective

inhibitors which, upon further development, could provide novel compounds against this untested drug target.

From our initial fragment screening of about 850 compounds, a total of 24 fungal enzyme inhibitors were identified, 14 of which showed good inhibition against multiple ASADHs (Table 2.2). These initial hits display a range of binding affinities, with the best inhibitors possessing K_i values in the low micromolar range against fungal ASADHs. Several of the inhibitors identified were already shown to inhibit other metabolic enzymes, and have been used as a starting point for the development of more potent inhibitors against these potential drug targets.⁵³⁻⁵⁴ Similarly, further elaboration of these initial ASADH inhibitors will be needed to develop their selectivity for this enzyme as a drug target.

Table 2.2. ASADH inhibitors from fragment library screening

Classes of ASADH inhibitors	microbial ASADHs (K_i values, μM) ^a				
	<i>C. neoformans</i>	<i>C. albicans</i>	<i>A. fumigatus</i>	<i>B. dermatitidis</i>	<i>S. pneumoniae</i>
a. non-selective microbial inhibitors					
1-amino-2-naphthol-4-sulfonic acid	115 ± 17	93 ± 12	219 ± 50	104 ± 13	234 ± 26
catechol	141 ± 16	121 ± 17	458 ± 94	141 ± 19	158 ± 31
benzene-1,3,5-triol	260 ± 70	440 ± 110	249 ± 45	153 ± 29	144 ± 30
<i>cis</i> -1,2-diaminocyclohexane	284 ± 36	287 ± 26	251 ± 32	428 ± 64	310 ± 44
cyclohexyl iodide	544 ± 55	154 ± 28	210 ± 35	188 ± 33	390 ± 92
b. fungal selective inhibitors					
L-thiazolidin-2-one-4-carboxylic acid	230 ± 33	225 ± 24	513 ± 101	230 ± 45	1790 ± 290
2-chloro-3-pyrrolidino-1,4-naphthoquinone	282 ± 89	950 ± 46	338 ± 34	311 ± 61	1140 ± 250
2-chloro-3',4'-dihydroxyacetophenone	360 ± 77	860 ± 150	517 ± 68	600 ± 115	1365 ± 48
3,4,5-trichloropyridazine	420 ± 90	453 ± 81	763 ± 108	877 ± 104	1820 ± 81
3,4-dihydroxy phenylacetic acid	220 ± 20	630 ± 140	650 ± 76	336 ± 51	> 2000
c. fungal species selective inhibitors					
<i>p</i> -benzoquinone	22 ± 2^b	73 ± 11	54.4 ± 8.3	126 ± 14	123 ± 21
phthaldehyde	150 ± 20	63 ± 11	154 ± 31	130 ± 28	159 ± 24
5-aminoisoquinoline	170 ± 50	84 ± 15	265 ± 53	172 ± 26	165 ± 41
4-amino-3-hydroxy-1-naphthalene sulfonic acid	580 ± 80	366 ± 45	84.6 ± 5.0	329 ± 62	>2000

^a *Cryptococcus neoformans*, *Candida albicans*, *Aspergillus fumigatus*, and *Blastomyces dermatitidis* are fungal enzyme forms, whereas *Streptococcus pneumoniae* is a bacterial form of ASADH.

^b Values in bold indicate the most potent inhibitors against the different bacterial and fungal ASADHs

2.9.2.3 Establishing the mode of ASADH inhibition

Many of our hits from library screening contain a quinone moiety, which could potentially act as a redox recycling agent on the PMS assay coupling step or by generating

hydrogen peroxide through reaction with a strong reducing agent such as DTT.⁵⁵ To test for the possible occurrence of a non-enzymatic redox reaction the assay was carried out by including two quinone-containing inhibitors, p-benzoquinone (200 μM) or 2,3-dichloro-1,4-naphthoquinone (20 μM), in the absence of ASADH and also in the absence of NADP. Alternatively, the complete coupling assay with ASADH and those inhibitors was tested without the substrate ASA. In each case no activity was detected, confirming the absence of quinone-induced redox cycling and any false positive hits from redox active compounds. To examine the potential reaction between our quinone inhibitors and a strong reductant, ASADH was dialyzed to replace DTT with a weaker reducing agent (β -mercaptoethanol) and also in the absence of any reducing agents. In both cases, the enzyme remained active and the same inhibition was observed with these two quinone-containing inhibitors, confirming that these compounds are targeting ASADH and that the observed inhibition is not due to redox artifacts.

Because the enzyme active site contains a cysteine nucleophile it is possible that some of these inhibitors could function by covalently modifying the active site thiol group, thereby leading to an inactivated enzyme. To test this possible mode of action the enzyme (30 μM) was incubated with a high concentration (500 μM) of either phthaldehyde or p-benzoquinone, two potentially reactive inhibitors, for 1 h and then dialyzed against buffer overnight to remove excess unbound inhibitor. The dialyzed enzyme remained active despite extensive exposure to these potentially reactive compounds. The redox inhibitor-incubated enzyme was also diluted into the assay mixture without dialysis. This 10-fold dilution lowers the final concentration of the inhibitor below its K_i value, resulting in a rate that is only slightly lower than the control in the absence of inhibitor, confirming that the

observed inhibition by these compounds is freely reversible. The incubated enzyme inhibitor complex was subjected to mass spectrometric analysis in order to confirm the mode of inhibition.

2.9.2.4 Electrospray Ionization – Mass Spectrometry (ESI-MS)

To test the reversibility of these protein-protein interaction inhibitors, ESI-MS analysis was conducted on protein samples treated with different small molecule inhibitors. The protein sample was dialysed overnight in 10 mM ammonium acetate, pH 7.0. The sample was then concentrated to 1.5 mg/ml to give a final protein concentration of around 50 μ M. The experiment was set up by taking one vial with enzyme as a control vial and another vial with 1 μ L of 50 mM phthaldehyde (cyclohexyl iodide) to produce a final concentration of 500 μ M phthaldehyde (or cyclohexyl iodide). The inhibitor was incubated with enzyme for 20 min and then examined by ESI-MS analysis. The ammonium acetate dialyzed sample was treated with 0.1% formic acid and the sample was loaded on to SYNAPT G2-Si High Definition Mass Spectrometry (Waters). The capillary voltage was set to 3.0 kV with 1 μ l/min flow rate and the expected molecular peak was further evaluated with MassLynx software. The sample was also subjected to ESI-MS without addition of 0.1% formic acid (native condition), but not enough peak was observed due to incomplete ionization of the sample.

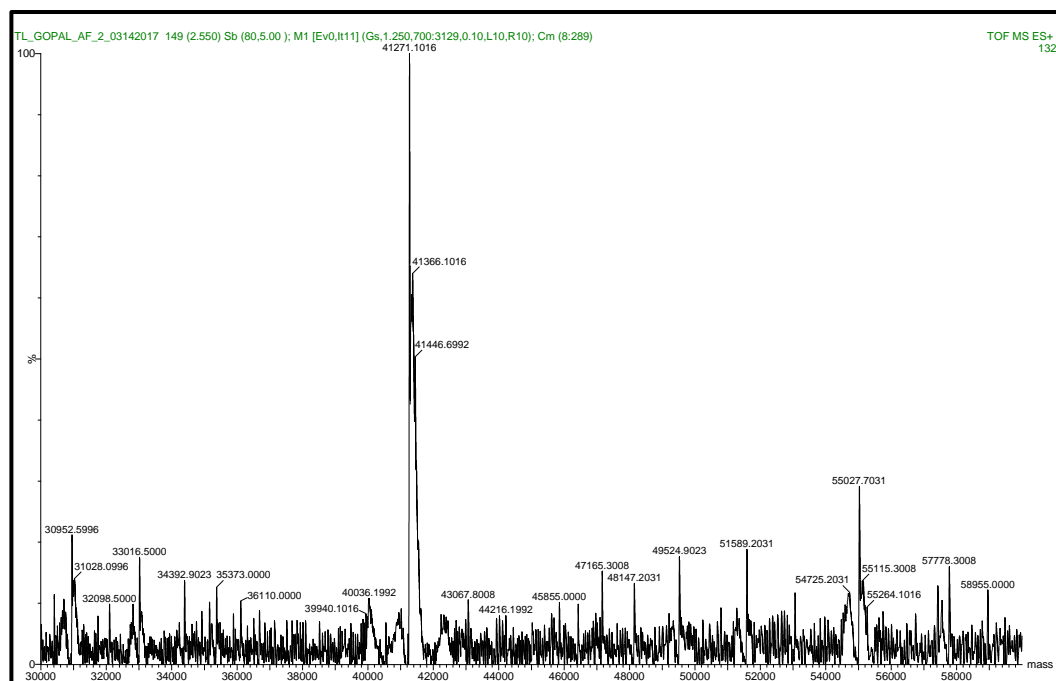
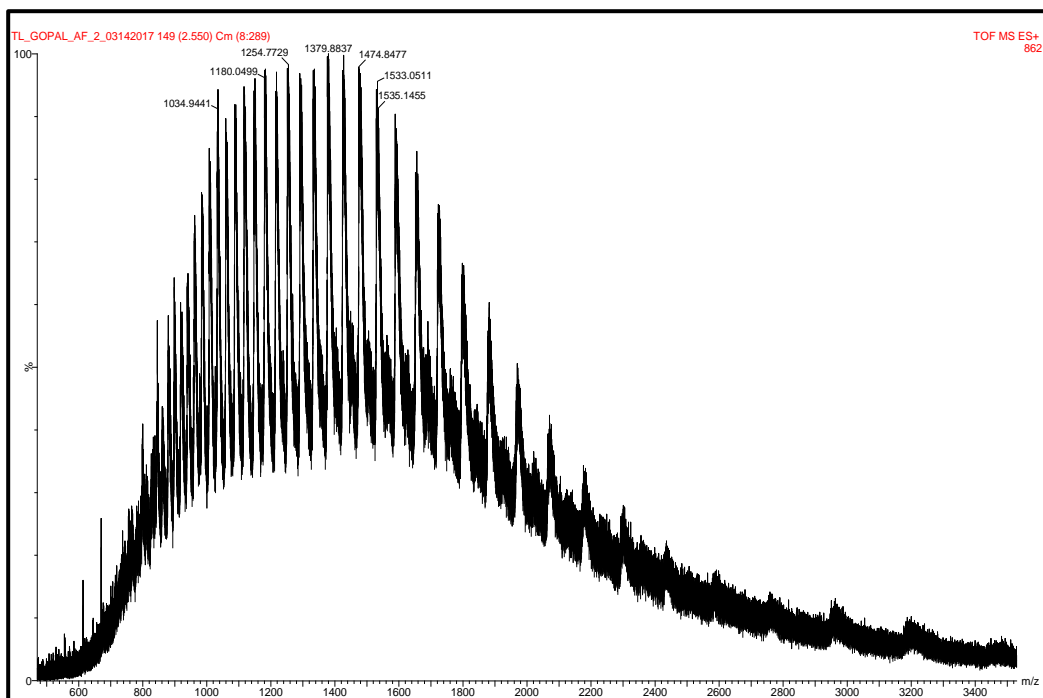


Figure 2.18: top) ESI-MS spectra of *AfASADH* sample in formic acid. bottom) ESI-MS deconvoluted spectra of *AfASADH*

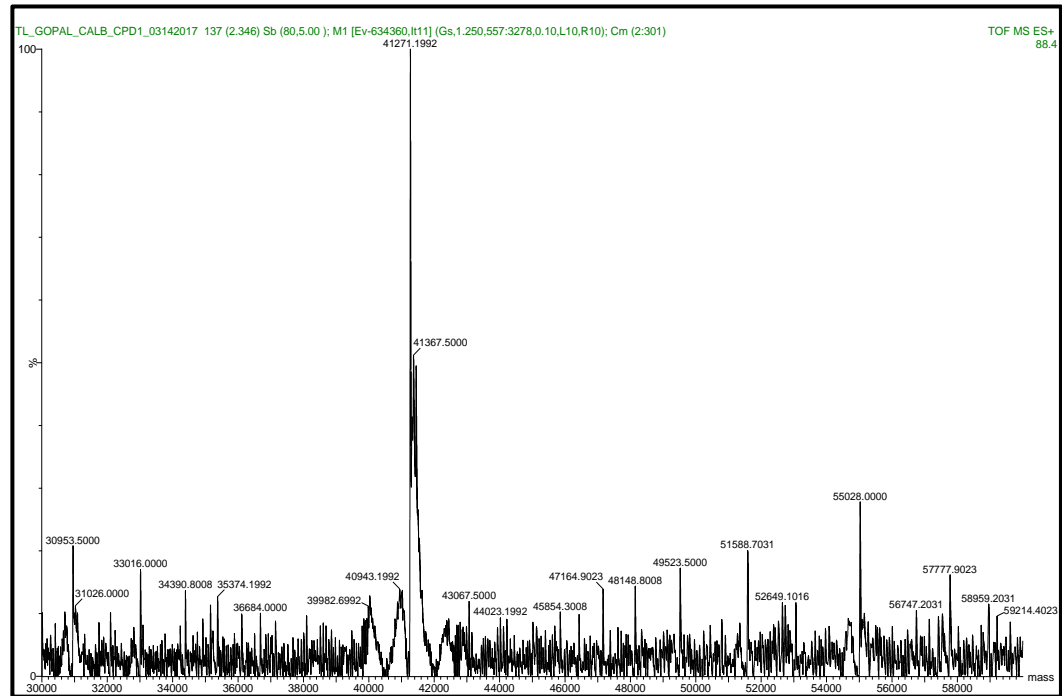
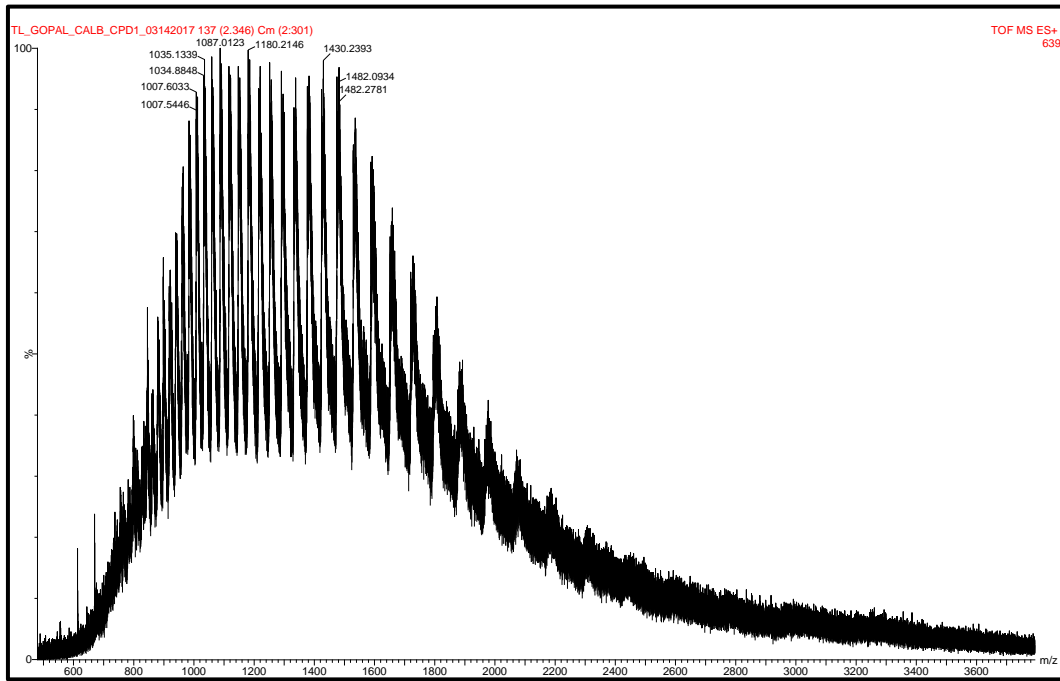


Figure 2.19: top) ESI-MS of phthalaldehyde-treated *AfASADH* sample. Bottom) ESI-MS deconvoluted spectra of phthalaldehyde treated *AfASADH*.

The control vial showed a single peak that closely corresponded to the molecular weight of the enzyme in its monomeric form (Figure 2.18), while the sample incubated

with the inhibitor did not show any changes in the measured mass (Figure 2.19). This result confirms that both phthaldehyde and cyclohexyl iodide (data not shown) are non-covalent, reversible inhibitors of *Af*ASADH.

2.9.2.5 Structure-Activity Relationship (SAR) studies

For inhibitor optimization and structure-activity relationship (SAR) studies, *Ca*ASADH was used as a model enzyme, due to the ease of crystallization of this enzyme form, enzyme stability, a higher yield during purification and, most importantly, because *Candida albicans* infections are considered a serious threat against humans. All of the compounds identified to date as inhibitors against *Ca*ASADH have also shown reasonably good inhibitory activity against the other fungal ASADHs.

Structural analogs of four different chemical scaffolds identified from fragment library screening, phthaldehyde and 5-aminoisoquinoline (*Ca*ASADH selective inhibitors), *p*-benzoquinone (a *Cn*ASADH selective inhibitor), and cyclohexyl iodide (a non-selective inhibitor), were chosen for evaluation of their SAR properties. In the available crystal structures,^{31, 41, 56} the active site of fungal ASADHs is shallow and partially open, with a central cavity that is fairly solvent accessible. The features of this accessible active site can be exploited to generate inhibitors encompassing the full active site environment. Also, the fungal forms are missing a small helical subdomain found in bacterial ASADHs, and these fungal ASADHs are found to be tetrameric³¹ in contrast to dimer found in bacterial species. This discrepancy can be utilized to develop selective inhibitors to potentially disrupt this tetrameric interface, which would present a novel route to develop inhibitors with a unique mode of action.

A characteristic feature of phthaldehyde is the presence of aldehyde functional groups in the 1,2 positions of the ring. Examination of a series of phthaldehyde-related compounds as potential *CaASADH* inhibitors revealed the importance of both the position and the nature of functional groups. Removal of one of the aldehyde groups (benzaldehyde) leads to complete loss of potency, while changing the relative positions of the aldehyde groups to the 1,3-position (isophthaldehyde) or the 1,4-position (terephthaldehyde) has a similar effect. Oxidizing phthaldehyde to phthalic acid also leads to a loss of potency while, in contrast, reduction to the dialcohol (catechol, $K_i = 121 \pm 17 \mu\text{M}$) causes only a 2-fold reduction of potency. Replacing one of the aldehyde groups with a nitro group (2-nitrobenzaldehyde, $K_i = 180 \pm 19 \mu\text{M}$) results in a 3-fold loss of potency, while extending the benzene ring to a naphthalene ($K_i = 45 \pm 8 \mu\text{M}$) leads to a slight improvement in potency. Each of these *CaASADH* inhibitors possess very good ligand efficiencies that are used to select fragment library hits for further structural elaboration. Examination of nearly 20 additional benzene or naphthalene structural derivatives, with either alcohol, thiol, nitro or carboxyl groups in various combinations and in various positions did not identify any additional fungal *ASADH* inhibitors.

A series of benzoquinone (Figure. 2.20, cpd. **1**) derivatives were also evaluated for inhibitory activity against *CaASADH*. Similar to the observation with phthaldehyde, reduction of the ketone functional groups to alcohols (**2**) has no effect on inhibitor potency, while the incorporation of a methyl group (**3**) shows a 3-fold loss in potency. The tetrachloro- (**4**) and the dichloro, dicyano-derivatives (**5**) show similar potency to the parent benzoquinone. Expansion of the benzene ring (1,4-naphthoquinone, **6**) also maintained inhibitory potency, suggesting the presence of a relatively large binding pocket in

CaASADH for these benzoquinone derivatives. However, further expansion of the aromatic ring system (anthraquinone, **7**) lead to complete abolition of binding affinity. Examination of a series of 1,4-naphthoquinone derivatives produced inhibitors with a range of potencies, with the best K_i values in the lower micromolar range. The halogenated naphthoquinone derivatives, 2,3-dichloro (**8**), 2-chloro (**9**), 2-bromo (**10**), and 2,3-dichloro-5,8-dihydroxy (**11**) each showed potent inhibition of *CaASADH*, with up to a 20-fold increase in affinity relative to the parent compound while still maintaining excellent ligand efficiencies (Figure 2.20). Maintaining a chlorine at the 2-position showed that inhibitor potency is also affected by alterations at the 3-position, with a 3-phenoxy derivative (**12**) being 18-fold less potent and the 3-methoxy derivative (**14**) nearly 3-fold more potent than the parent 2-chloro derivative (**9**). Both the identity and the position of the functional groups on the naphthoquinone ring were found to be critical. When the position of the dichloro groups were moved to the opposite side of the ring (from 2,3- to 6,7-dichloro) this derivative was a non-inhibitor.

For the initial 5-aminoisoquinoline inhibitor, moving the position of the amino group, or replacing the amino group with a different potential hydrogen bond donor/acceptor group (hydroxyl) at those different positions resulted in the complete loss of potency. Similarly, modifications made to the cyclohexyl iodide inhibitor, such as replacement of the iodide with other halides or with an amine group caused a loss of potency. The 1,2-diaminocyclohexane derivative is a moderate inhibitor ($K_i = 251 \pm 32 \mu\text{M}$) when these functional groups are oriented in a *cis*-geometry, but the *trans*-diamine derivative does not show measurable inhibition against *CaASADH*.

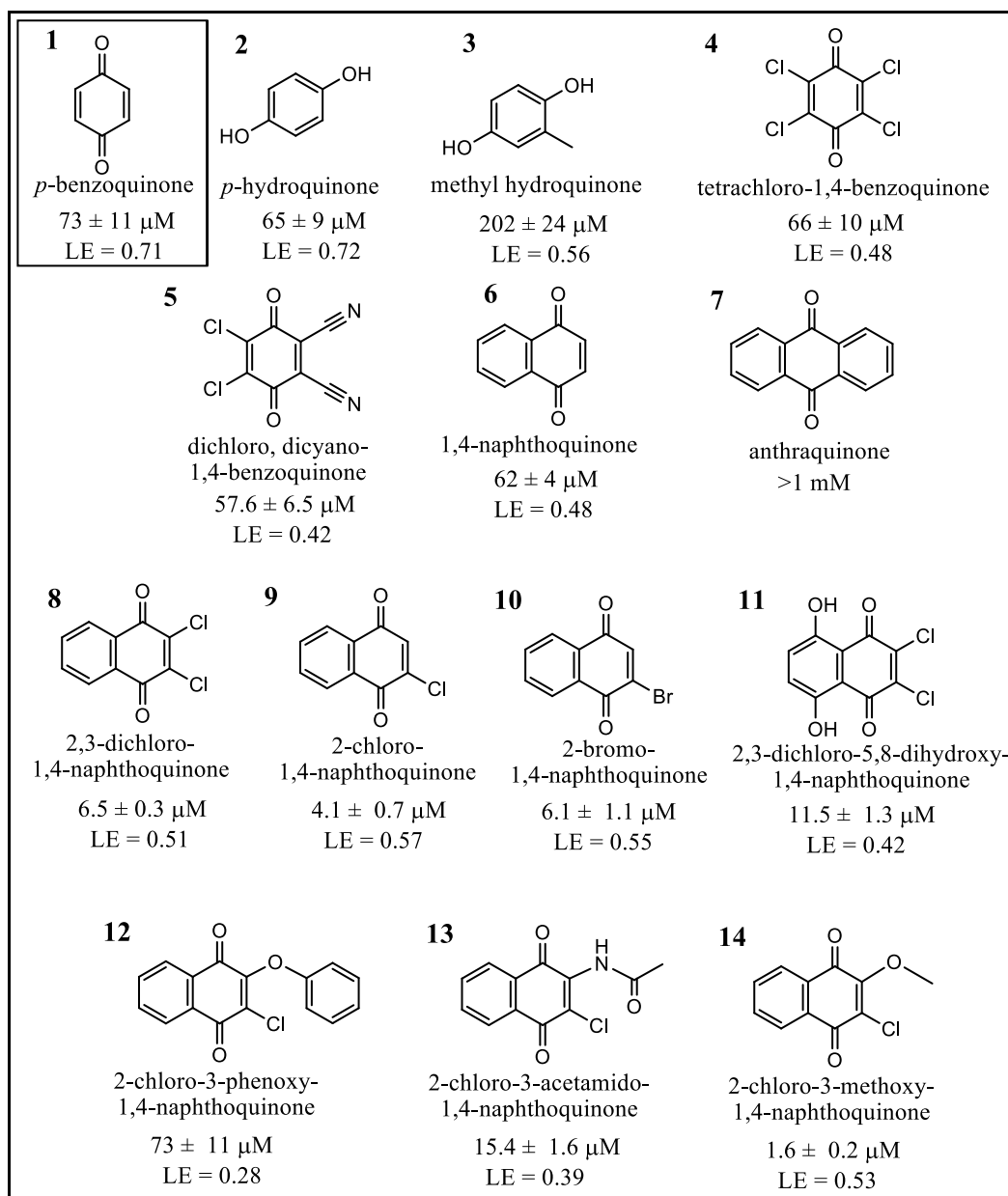


Figure 2.20: *p*-Benzoquinone structural analogs screened as potential inhibitors against *Ca*ASADH. The most potent of these inhibitors, based on a naphthoquinone core structure, have inhibition constants in the very low micromolar range and excellent ligand efficiency (L.E.) values.

2.9.2.6 Inhibitor species selectivity

A number of different naphthoquinone derivatives show enhanced affinity to *Ca*ASADH relative to the parent benzoquinone compound, with up to a factor of nearly 50

for the most potent derivative (Figure 2.18). An examination of these compounds as inhibitors of the other fungal ASADHs show similar improvements. The parent *p*-benzoquinone binds to *Af*ASADH with comparable affinity to that against *Ca*ASADH, and with an IC₅₀ value that is similar to its inhibition constant (Figure 2.19). This inhibitor shows some ortholog specificity, with a 3-fold greater affinity in binding to *Cn*ASADH (Table 2.3). However, each of the halo-naphthoquinones show the greatest affinity with *Af*ASADH, with improvements ranging from 2- to 7-fold for these derivatives relative to that against *Ca*ASADH. The 2,3-dichloro derivative (cpd. **8**) and the 2-chloro-3-methoxy derivative (cpd. **14**) are the most potent inhibitors of these fungal ASADHs, with a 60- to 75-fold improvement both in K_i and in IC₅₀ values (Figure 2.21) over the parent *p*-benzoquinone, leading to the first sub-micromolar inhibitors of a fungal ASADH (Table 2.3).

Table 2.3. Selectivity of naphthoquinone derivatives against fungal ASADHs

Cpd. No.	Quinone inhibitors	Fungal ASADHs (K _i values, μM)			
		<i>C. neoformans</i>	<i>C. albicans</i>	<i>A. fumigatus</i>	<i>B. dermatitidis</i>
1	<i>p</i> -benzoquinone	22 ± 2	73 ± 11	54.4 ± 8.3	126 ± 14
12	2-chloro-3-phenoxy-1,4-naphthoquinone	77 ± 12	73 ± 11	61.0 ± 7.2	86 ± 12
13	2-chloro-3-acetamido-1,4-naphthoquinone	18.2 ± 1.9	15.4 ± 1.6	12.7 ± 1.3	16.6 ± 1.8
11	2,3-dichloro-5,8-dihydroxy-1,4-naphthoquinone	8.3 ± 1.5	11.5 ± 1.3	5.25 ± 0.27 ^a	10.8 ± 1.9
10	2-bromo-1,4-naphthoquinone	10.5 ± 1.6	6.1 ± 1.1	2.51 ± 0.25	6.3 ± 1.0
9	2-chloro-1,4-naphthoquinone	6.2 ± 1.6	4.1 ± 0.7	1.43 ± 0.14	2.1 ± 0.3
8	2,3-dichloro-1,4-naphthoquinone	1.2 ± 0.1	6.5 ± 0.3	0.91 ± 0.12	1.7 ± 0.3
14	2-chloro-3-methoxy-1,4-naphthoquinone	2.5 ± 0.3	1.6 ± 0.2	0.88 ± 0.12	2.2 ± 0.3

^a Values in bold show the most potent inhibitors against four different fungal ASADHs

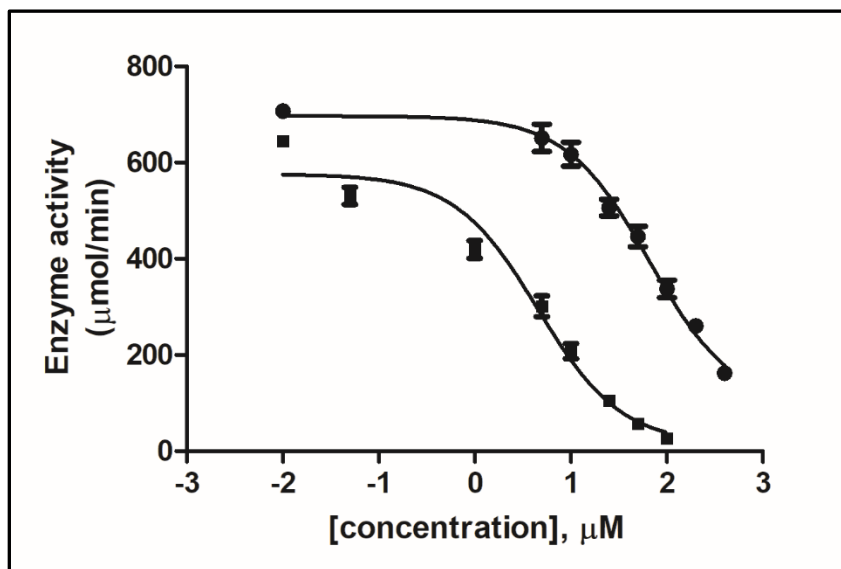


Figure 2.21: Representative dose-response curves for 2-chloro-1,4-naphthoquinone (■), a strong inhibitor ($\text{IC}_{50} = 0.6 \mu\text{M}$), and for *p*-benzoquinone (●), a moderate inhibitor ($\text{IC}_{50} = 50 \mu\text{M}$), interacting with AfASADH. Each rate was determined in triplicate with the error bars shown on each data point.

2.9.3 Drug library screening

The more traditional approach to compound screening uses larger chemical libraries containing drug-like compounds that have been optimized against previously identified targets to assess any potential cross-reactivity against new potential drug targets. The NIH clinical collection (NCC) is a library of over 700 drug and drug-like compounds, while the Prestwick library is a University of Toledo collection of over 1300 drugs and drug candidates. The NCC library was screened at $500 \mu\text{M}$, with these screening experiments performed in duplicate using the coupled enzymatic assay for primary screening. Due to limited compound availability screening was initially performed only with CaASADH. From this initial screening a total of 14 compounds showed good enzyme inhibition, with the percent inhibition ranging from 70% to as high as 97%. The overall hit rate for the NCC library was about 2% which is quite high compared to other chemical library screens.

However, once again it is not surprising to have these higher hit rates considering that the majority of these drugs have gone through multiple selections from numerous libraries, and have been optimized for binding to a range of different drug targets.

The compounds showing 70% or more decrease in enzyme rates compared to controls were selected as potential inhibitors for K_i value determination. The compounds examined each inhibited *Ca*ASADH in the lower micromolar range, with K_i values ranging from ~200 μ M down to 42 μ M. Interestingly, some of these best NCC library hits possess similar pharmacophoric features as those of the better fragment library hits (Figure 2.22, highlighted in red).

To test the importance of these pharmacophores in binding to fungal ASADHs a set of about 70 compounds were selected from the Prestwick drug library for testing, based on the presence of their potentially related sub-structures. Screening of these compounds identified an additional 15 inhibitors of *Ca*ASADH, an unusually high hit rate of 20% that serves to validate the importance of these sub-structures in recognition by the fungal ASADHs. The six most potent of these inhibitors have K_i values between ~50 to 200 μ M, and included compounds with catechol, quinone and isoquinoline-type sub-structures (Figure 2.22). The majority of these drugs still have quite high ligand efficiency values, except for those with more extensive structures relative to the fragment library hit structures. The failure of the clinical drugs to bind with significantly higher affinities than that seen for the simpler structural components confirms that these compounds have already been optimized for selectivity against their designated targets. A similar optimization scheme will be needed to generate potent and selectivity inhibitors against the fungal ASADHs.

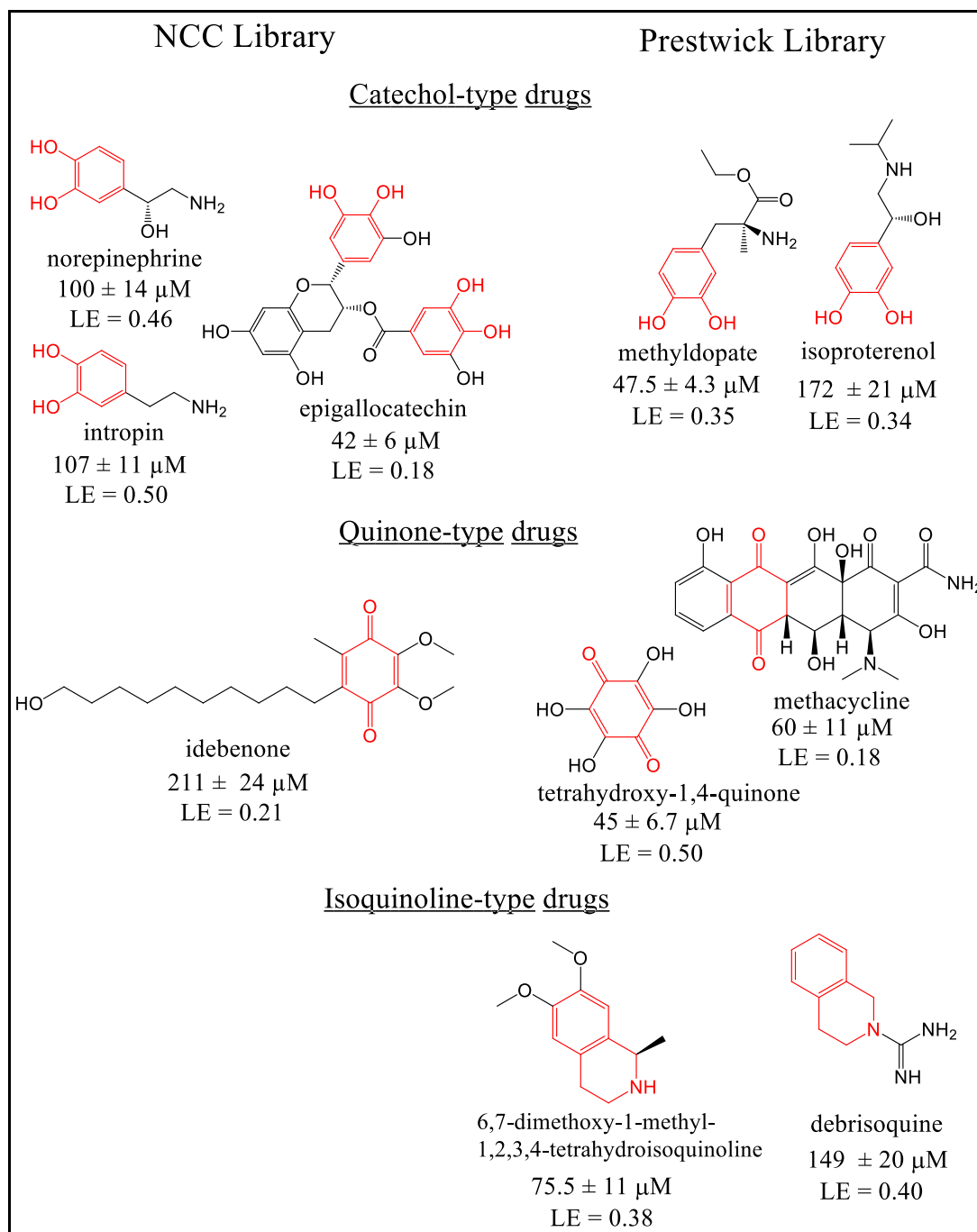


Figure 2.22: The most potent inhibitors against *Ca*ASADH identified from the NIH clinical collection library (left) and the Prestwick library (right). The essential core sub-structures are highlighted in red, showing the common catechol, quinone and isoquinoline moieties that are also found in the inhibitors that were identified from fragment library screening.

2.9.4 Future inhibitor optimization

Most of the productive interactions identified between these fungal ASADHs and the more potent inhibitors are proposed to involve just two functional groups on the naphthoquinone ring (Figure 2.18). Additional functionalization and elaboration of this core structure has the potential to make new interactions with an array of active site functional groups. The proposed interactions with the docked compounds from virtual library screening will be tested by the incorporation of these and related functional groups into the inhibitor structures. As structure of these inhibitors bound to our target enzyme become available this information will be incorporated into our inhibitor optimization scheme. This structure-guided approach will likely lead to significantly more potent and more selective inhibitors of this essential fungal enzyme.

2.10 Oligomeric state of fungal ASADHs

2.10.1 Native PAGE

In order to identify the oligomeric state of different fungal ASADHs, Native PAGE electrophoresis protocol was performed following standard protocol optimized by Invitrogen (Life Technologies). 5 μ L of each protein sample (2 mg/ml) with total sample volume of 20 μ L was loaded onto each well of 3-12% bis-tris native gel. The setup was run using dark cathode buffer in the inner chamber with running buffer outer chamber for 1 h at 150V followed by 1 h at 250V at 4 °C. Protein bands were destained using 40% methanol and 10% acetic acid solution, and oligomeric state was identified on the basis of movement of standard protein marker. From the native page results the oligomeric state of bacterial ASADHs was found to be a dimer, whereas for the fungal ASADHs it was found to be either a dimer of dimers or a tetramer (Figure 2.23, left).

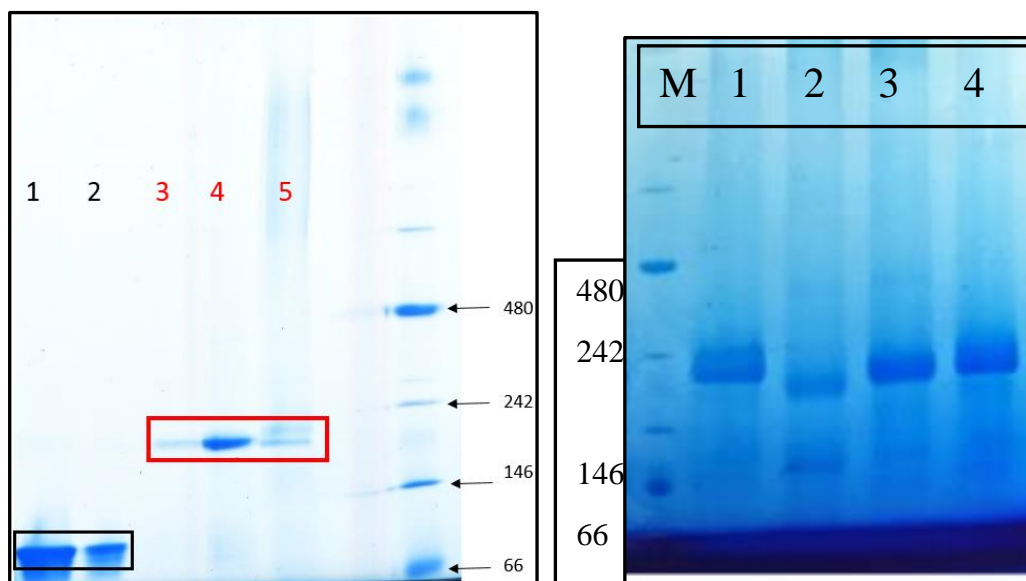


Figure 2.23: (Left) Native PAGE electrophoresis of different ASADHs on 3-12% bis-tris gel. Lane 1 and 2 corresponds to bacterial ASADHs *S. pneumoniae* and *V. cholerae* ASADH respectively. Lane 3, 4 and 5 represents fungal ASADHs that corresponds to *A. fumigatus*, *C. albicans* and *C. neoformans* ASADH respectively. The rightmost lane shows the standard molecular weight marker with corresponding molecular weight in kDa. Right: Effect of increasing [cyclohexyl iodide] on dissociation of *Ca*ASADH into inactive dimers. Lane 1-4: [cyclohexyl iodide] = 0, 500, 250, 100, μ M, respectively.

2.10.2 Protein-Protein interactions inhibitors

Fungal ASADH was found to assemble as a tetramer, in contrast to bacterial ASADHs that are functional dimers. It was found that tetramerization is essential for fungal ASADHs to be active, determined *via* site-directed mutagenesis, small angle x-ray scattering and biochemical analysis. We attempted a screen of some small molecule inhibitors to identify compounds that could specifically bind at the interface and disrupt the tetrameric assembly. Initial fragment library hits were screened against different fungal ASADHs and the effect of these small molecules were observed by native gel

electrophoresis. Two structurally diverse small molecules were found to be shifting the oligomeric arrangement from tetramer to dimer. Cyclohexyl iodide and phthalaldehyde shifted the movement of the protein band to a position corresponding to dimeric molecular weight. The effect of each of these compounds were further verified by incubating different concentration of the inhibitor with the enzyme, and each compound showed a concentration dependent shift in molecular weight of fungal ASADHs (Figure 2.24). A general shift in tetrameric molecular weight of the enzyme was observed and additional studies needs to be performed in order to explain this mobility of the enzyme. This concentration-dependent effect was observed with several other fungal ASADHs as well (data not shown).

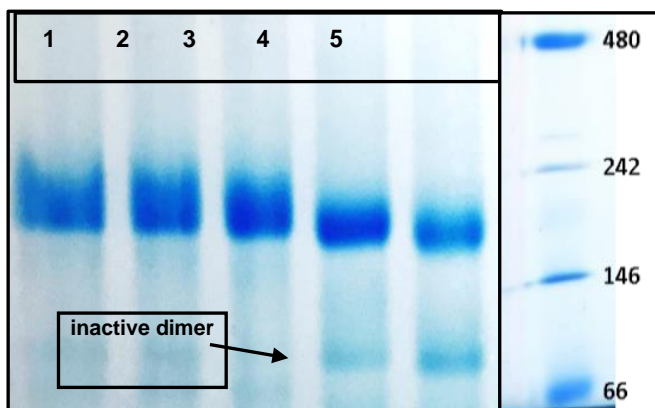


Figure 2.24: Effect of increasing [phthalaldehyde] on dissociation of *Ca*ASADH into inactive dimers. Lane 1-5: [phthalaldehyde] = 0, 10, 100, 500, 1000 μ M, respectively.

2.11 Other enzyme targets in the aspartate biosynthetic pathway

Several additional enzymes involved in the aspartate biosynthetic pathway are also attractive targets for antifungal drugs. Besides ASADHs, we have studied several other enzymes in the pathway that are validated drug targets from pathogenic fungal organisms. The preliminary results with these alternative drug targets are described below.

2.11.1 Homoserine Dehydrogenase

The NADPH-dependent reduction of ASA to produce homoserine is catalyzed by homoserine dehydrogenase, a key enzyme involved in biosynthesis of methionine, isoleucine and threonine⁵⁷ in fungi. The crystal structure of HDH has been solved from five different organisms, with a total of eight crystal structures from *Thiobacillus denitrificans* (PDB code 3mtj), *Thermoplasma volcanicum* (PDB code: 3jsa and 3c8m), *Thermoplasma acidophilum* (PDB code: 3ing), *Archeoglobis fulgidus* (PDB code: 3do5), *Thermus thermophiles* (PDB code: 2ejw) and *Sachharomyces cerevisiae* (PDB code: 1tve, 1q7g, 1ebf and 1ebu)⁵⁸ to date. The crystal structure of HDH from *S. cerevisiae* has been found to be a dimer, with each monomer comprising of a nucleotide binding region, a dimerization region and a substrate binding region⁵⁸. Since limited structural information is known regarding other pathogenic fungal species, we aim to resolve the issue by solving the crystal structure from one of the most common human fungal pathogens, *Candida albicans*.

2.11.1.1 Cloning of homoserine dehydrogenase

Cloning of the gene encoding homoserine dehydrogenase from the fungal species *Candida albicans* was initially carried out by Gibson cloning (New England Biolabs)⁵⁹. The *CaHDH* gene was initially amplified from the genomic DNA of *C. albicans* (genomic DNA received as a gift from Dr. Conti, Biology Department, University of Toledo) using standard polymerase chain reactions. The overnight fungal cell culture received from Dr.

Conti's lab was purified to extract the genomic DNA by using a genomic DNA elute kit (Sigma Aldrich). Two oligonucleotide primers were designed:

Forward primer: 5'- tgggtcgcggatccgaattcATGTCAAAGTCAGTTAATGTTG-3'

Reverse primer: 5'- cagtgggtgggtgggtgggtgctcgagTCAATTGGCAATTCTTTCAG-3'

complementary to the amino terminal and the carboxyl terminal, respectively were used to amplify the gene from the genomic DNA. The gene was successfully amplified using the reaction mixture consisting 20 ng of genomic DNA, 10 μ M each of forward and reverse primers, 8 μ mole of dNTP mix, and 2000 units/ml of Q5 DNA polymerase. The thermal cycler parameters were set as follows: Initial denaturation at 94 °C for 30 s, annealing 59 °C for 30 s, extension at 72 °C for 30 s for total of 25 cycles.

The pET-28a (+) vector was linearized using two oligonucleotide primers:

Forward primer: 5'- CTCGAGCACCACCACCAC-3'

Reverse primer 5'- GAATTCGGATCCGCGACC -3'

in order to have the overlapping sequence complementary with the *Ca*HDH gene sequence with an EcoRI site at the N-terminus and an XhoI site at the C-terminal. The amplified gene corresponding to the correct molecular weight on the agarose gel was extracted and purified using Qiagen gel extraction kit. Gibson assembly was carried out using 1:2 concentration of purified vector: insert with 2 μ L of the Gibson master mix setup for 30 min at 50 °C for the isothermal reaction. The plasmid was transformed into DH5 α *E. coli* cloning host and positive colonies were grown overnight. The DNA sequence was confirmed by restriction digestion.

The *CaHDH* gene cloned using Gibson assembly showed single band around 1100 bp which is expected for the correct molecular weight of the *CaHDH* gene (Figure 2.25, last two lanes). The gel purified gene and vector were found to be pure with no protein contaminants. The Gibson assembled plasmid gave more than 100 colonies in the kanamycin-resistant plates, which showed the successful cloning of the *CaHDH* gene into the pET28a (+) vector. Sequencing results showed the correct incorporation of the gene after the *EcoRI* and *XhoI* sites with the hexahistidine tag.



Figure 2.25: Agarose gel profile after PCR of *CaHDH* gene. The bands corresponding to the gene (≈ 1100 bp) are shown inside the red rectangle.

2.11.1.2 Expression and purification

Expression constructs was prepared by transforming kanamycin-resistant colonies into a BL21 (DE3) *E. coli* cell line. The integrity of the clone was confirmed by DNA sequencing. The optimized construct was cloned into a modified pET28a (+) vector with a C-terminal hexahistidine tag using Gibson cloning. The protein was induced using 0.4 mM IPTG until the cell density reached OD_{600} of 0.6 to 0.8, and cells were allowed to grow for additional 20 h at 16 °C. Cell paste was prepared by centrifuging the overnight culture at 11,000 rpm. For protein purification 5 g of cell paste was loaded onto a Ni-IMAC column

and the protein was eluted using a 20 to 400 mM linear imidazole gradient. The protein was eluted with several other impurities as shown by SDS gel (Figure 2.26 b). The protein was further purified using anion exchange source 30Q column using a 50 to 600 mM NaCl gradient, and the eluted protein shows a higher level of purity when compared to the Ni-IMAC sample (data not shown). The protein band corresponding to the expected molecular weight from SDS-PAGE was checked for activity assay and dialyzed overnight in a buffer containing 20 mM HEPES pH 7.0, 0.5 mM EDTA and 50 mM NaCl.

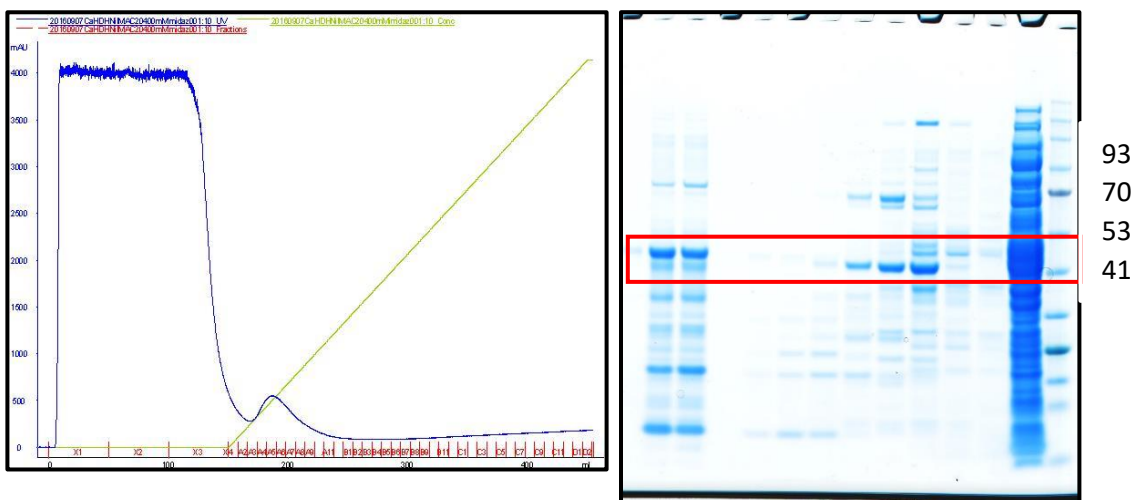


Figure 2.26: a) Ni-IMAC purification profile of *CaHDH* b) SDS PAGE gel after Ni-IMAC column. The band inside the red rectangle showed the expected molecular weight of *CaHDH* sample (≈ 40 kDa)

2.11.1.3 Kinetic assay and library screening of *CaHDH*

Since HDH is also a NADPH-dependent dehydrogenase⁶⁰, a kinetic assay was developed on the basis of absorption of NADPH at 340 nm. The kinetic assay of *CaHDH* was performed in the reverse direction using the conversion of the substrate L-homoserine into the product ASA, whereby NADP get reduced to NADPH (Figure 2.27). This assay was carried out in the presence of 10 mM L-homoserine and 0.1 mM NADP for the reverse

reaction. Utilization of a coupled enzyme assay was performed to shift the absorbance from 340 nm to 500 nm, using an INT-PMS coupled assay developed for ASADH.

A small molecule screening against yeast HDH has been conducted to identify a new class of fungal inhibitors⁶¹. Homology modelling, molecular dynamics and virtual screening against the ZINC database has been previously attempted in order to identify lead compounds that are predicted to show appreciable binding affinity against HDHs⁶². In order to achieve our selective inhibitor design strategy, an in-house fragment library screening against fungal HDHs was performed. The initial hits identified from the library screening are currently being used for co-crystallization experiments in order to get a starting point for crystal optimization.

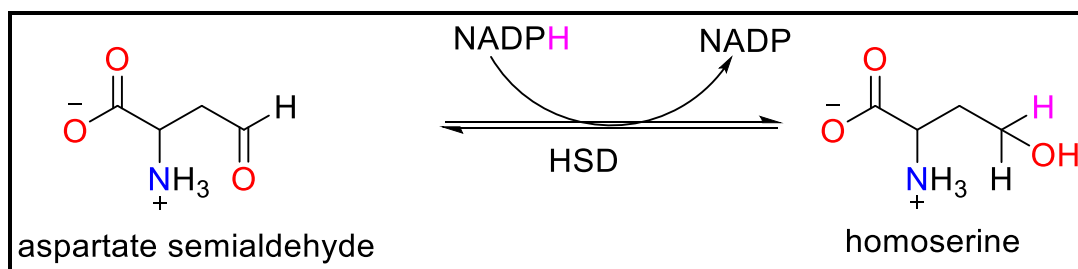


Figure 2.27: Kinetic reaction catalyzed by homoserine dehydrogenase (HDH)

2.12 L-lysine biosynthesis in fungi

Lysine biosynthesis is unique in fungi. Lysine is one of the eight essential amino acids for human and animals and can only be obtained from the protein in the diet⁶³ and depletion of lysine leads to auxotrophy. While bacterial biosynthesis of lysine starts with L-aspartate as the precursor, lysine biosynthesis in fungi utilizes α -ketoglutaric acid as a precursor with eight sequential steps⁶⁴. The first half of the pathway, yielding α -aminoadipate, takes place in mitochondria, while the remaining conversion to L-lysine

occurs in the cytoplasm with exception of the synthesis of homocitrate in the nucleus⁶⁴. Several steps in this pathway closely resembles the bacterial arginine biosynthesis pathway⁶³ and this pathway is a member of glutamate family of amino acid biosynthesis. We have studied three essential enzymes from this lysine biosynthesis pathway from pathogenic fungi *Candida albicans* and all three enzymes doesn't have any introns in them.

2.12.1 Homocitrate Synthase

The first committed step of lysine biosynthesis in fungi is the condensation of α -ketoglutarate and acetyl-CoA, catalyzed by the enzyme homocitrate synthase (HCS, EC:2.3.3.14) to form the product homocitrate⁶⁴. The *Lys1* gene encoding HCS from *Candida albicans* (1254 bp) was PCR amplified using the *C. albicans* genomic DNA as a template. The amplified template was subjected to Gibson assembly to sub-clone with pET 28a (+) vector to yield the final expression construct containing *CaHCS*. Primers for amplification of gene and vector using Gibson cloning are listed below.

CaHCS Forward: GAATTCGGATCCGCGACC

CaHCS Reverse: CTCGAGCACCACCACCAC

pET28a Forward: tgggtcgcggatccgaattcATGTCTGTTGCTTCTAATC

pET28a Reverse: cagtgggtggtggtggtgctcagCTATACTTTTTGTTTTTAATTTCTGG

The *CaHCS* plasmid-containing cells were transformed into DH5 α and BL21 cells, and the sequences were confirmed by DNA sequencing. The optimum condition for protein expression was found to be 0.1 mM IPTG at 16 °C for 18 h. The protein purification was performed by Ni-IMAC chromatography following a similar protocol to that used for *CnASADH* purification, and pure fractions were dialyzed and stored at 4 °C for further use.

2.12.2 Homoaconitase (homoaconitate hydratase)

The enzyme homoaconitase (HAN) encoded by the LYS4 gene catalyzes the two-step transformation of homocitrate to homoisocitrate *via* the homo-cis aconitate intermediate. This transformation is analogous to the conversion of citrate to isocitrate in the TCA cycle by aconitase⁶⁴. The Lys4 gene encoding HCS from *Candida albicans* (2055 bp) was PCR amplified using a genomic DNA as a template. The amplified template was subjected to Gibson assembly to sub-clone with pET 28a (+) vector to yield the final expression construct *CaHAN*. Primers used for amplification of the gene and the vector is listed below.

CaHAN Forward: GAATTCGGATCCGCGACC

CaHAN Reverse: CTCGAGCACCACCACCAC

pET28a Forward: tgggtcgcggatccgaattcATGATGTTACGATTTAGGTC

pET28a Reverse: cagtgggtggtggtggtgctcagTTATTGGTTTGTTCATTCAATTCAC

Transformation with DH5 α and BL21 cells was performed and final construct was confirmed by DNA sequencing. The optimum condition for protein expression was found to be 0.5 mM IPTG at 16 °C for 18 h. Optimization of the protein purification is currently under progress.

2.12.3 Homoisocitrate dehydrogenase

Homoisocitrate dehydrogenase (HID) catalyses the NAD⁺-dependent transformation of the substrate homoisocitrate to the product α -keto adipate⁶³. The Lys1 gene encoding HCS from *Candida albicans* (1131 bp) was PCR amplified using a genomic DNA as a template (Figure 2.28). The amplified template was subjected to Gibson assembly to sub-clone with pET28a (+) vector to yield the final expression construct

containing *CaHID*. The primers used for amplification of the gene and the vector are listed below.

CaHID Forward: GAATTCGGATCCGCGACC

CaHID Reverse: CTCGAGCACCACCACCAC

pET28a Forward: tgggtcgcggatccgaattcATGTTAGCTGCTAGATCTTC

pET28a Reverse: cagtgggtggtggtggtgctcgagtagaatctCTAATGATATCATCTATAAC

The plasmid-containing cells were transformed into *E. coli* DH5 α and BL21 cells, and the construct was confirmed by sequencing. The optimum condition for protein expression was found to 0.1 mM IPTG at 16 °C for 20 h. The protein was purified using Ni-IMAC chromatography and pure fractions were dialyzed using dialysis buffer and store at 4 °C until use.



Figure 2.28: Agarose gel profile after PCR of the *CaHID* gene. Bands corresponding to gene (\approx 1200 bp) are shown inside the red rectangle.

Efforts are currently undergoing to characterize and crystallize these three enzymes involved in the fungal lysine biosynthesis pathway.

2.13 Conclusions and future work

Purification of target enzymes from several pathogenic microbes has been the prerequisite for initiating our structural-based drug design approaches. The pure proteins will be screened for crystallization, with these studies discussed in Chapter 3. Several approaches, such as changing the strong promoter T7 into a weaker pBAD promoter, purifying the proteins from inclusion bodies using different chaotropes such as guanidium hydrochloride under denaturing conditions, and using tuner cells to optimize the IPTG concentration are the next approaches that will be examined to purify ASADH from *T. gondii*. Fragment library screening approaches will be performed against each of the purified enzymes, and initial hits will be optimized following appropriate SAR studies.

Chapter 3

Structural studies of fungal ASADHs

3.1. Introduction

The aim of this project is to find selective and potent inhibitors against our representative enzyme forms. In order to study the effect of the inhibitors to an enzyme, it is essential to know the nature and type of interactions, the inhibitor is interacting to that enzyme. This can be achieved by X-ray and neutron crystallography, small angle x-ray scattering, docking and molecular dynamics studies. X-ray diffraction is the best method for structural analysis of macromolecules and is widely being used to identify the mechanism of inhibition and the mode of binding against different target enzymes. X-ray crystallography will reveal complete three-dimensional structure of an enzyme whereas neutron crystallography is able to identify most of the hydrogens atoms as well. Small angle x-ray scattering is powerful tool to estimate the aggregation of the protein sample and also to identify the oligomeric state of the macromolecule. Computational techniques such as docking and molecular dynamics are key tools in estimating the *in-silico* binding of an inhibitor to an enzyme and validating the stability of the inhibitor to its receptor molecule.

3.2. Pre-crystallization test (PCT) and initial crystal screening

To identify the conditions for crystallization for each of the protein, Pre-Crystallization Test (PCT) was performed at 14 mg/ml for *CnASADH* and *AfASADH*, and at 10 mg/ml for *BdASADH*. Each PCT reagent (500 μ L) were added as a precipitant, along with 1 μ L each of protein and precipitant, set up as a crystallizing drop. Light granular precipitate was observed after 24 hours from all three protein samples, suggesting that these protein concentrations are in a reasonable range for crystal screening. The initial screening for crystallization of each of these apo-enzymes was carried out using a commercially available sparse matrix screening kits, Jena Bioscience Basic screening and Index screening from Hampton Research, with a total of 96 conditions each. The screening trays were set-up by mixing an equal volume (1 μ L) of the protein with the reservoir solution in a 96-well sitting drop tray and incubating at 293 K. Initial hits were obtained from a few conditions, followed by extensive optimization of the protein concentration, precipitant, temperature, and pH in order to get diffraction quality crystals. The incorporation of other additives in the crystallization conditions were also evaluated.

3.3 *CnASADH* crystal screening:

(Text and figures in this section are adapted from Dahal et. al., Acta Cryst F., 2015)

Initial screening of crystallization conditions for the apo form of *CnASADH* were performed in 24-well plates using commercial crystallization kits from Jena Bioscience as well as in-house custom screening kits. The JB screen basic 2 combination C4 was found to be the best hit, with conditions as 10% PEG 8000, 8% ethylene glycol, 100 mM HEPES, pH 7.5, with 1:1 protein to precipitant solution using the hanging drop vapor diffusion method. This initial crystal hits were extensively optimized, and the best crystals were

grown at 293 K using a 2:1 ratio of protein solution (9 mg/ml) to well solution. Rod-shaped crystals (Figure 3.1) were obtained after 48 h using 10% PEG 8000, 6% ethylene glycol, 0.1 M HEPES, pH 7.5, for the well solution. In parallel, the recombinant enzyme was co-crystallized with the cofactor NADP at 4 mM final concentration using the same conditions as for apo-enzyme, and a few moderate inhibitors at 10 mM in order to find the mode of binding with NADP and the inhibitors.

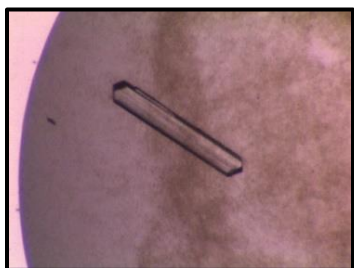


Figure 3.1: Initial hits of *Cn*ASADH from Jena Bioscience screening kit. Conditions were: 10% PEG 8000, 6% ethylene glycol, 0.1 M HEPES, pH 7.5, [P] = 9 mg/ml.

3.3.1 Crystal seeding

The apo-enzyme of *Cn*ASADH crystals grew to a small size, which were not sufficient for soaking experiments. In order to get larger crystals a seed stock of small crystals were prepared by crushing them and vortexing at high speed with a bead. The stock solution was made using 1:1 mixture of crushed crystal and cryo solution (25% ethylene glycol in mother liquor). Serial dilution of 1:10, 1:100 and 1:1000 solutions were prepared for optimizing crystal nucleation, with 0.2 μ l of each solution added to successive drops that had been equilibrated overnight. A seeding technique using a fine brush fiber was also performed by dipping the brush into the stock seed solution and streaking the coarse brush surface on the drops and proceeding horizontally through the drops from the middle in order to set up a decreasing concentration gradient of the stock solution.

Unfortunately, each of these seeding techniques did not improve the size of crystals despite using different concentration of seeds, different time point of adding seeds and different seeding techniques. Testing conditions with only PEG8000 as the precipitant didn't yield any crystals, demonstrating that ethylene glycol was necessary in order to get at least small crystals. Various molecular weight PEGs (from 1500 to 8000) were tried as precipitants, but these conditions didn't improve crystal quality or crystal diffraction.

3.3.2 Additive screening

After extensive optimization of precipitant, protein concentration, pH and different crystallization methods including seeding, only small crystals of *CnASADH* were obtained. Both microseeding and macroseeding didn't help to obtain larger quality crystals. Additive screening, which contains a library of reagents that can affect the solubility of macromolecules has been shown to improve the crystal size and quality in some cases. These additive reagents contain multivalent ions, salts, amino acids, dissociating agents, linkers, polyamines, osmolytes, chaotropes, co-factors, reducing agents, chelating agents, polymers, carbohydrates, non-detergent amphiphiles, detergents, non-volatile and volatile organic solvents. The crystal tray setup was exactly the same used to yield small size crystals, and the 96 drops were setup with 0.5 μ L of 100 mM additives added to each of the crystallizing drops. Each drop was monitored after 24, 48, 72, and 42 h to observe the possible changes in size and quality of *CnASADH* crystals. The additive screening produced some drops with immediate precipitates, some clear drops, and some of the additives helped in increasing the initial crystal size at least 2-fold. Strontium chloride hexahydrate, lithium chloride, sodium bromide and EDTA were each found as additives that helped to increase the crystal size.

3.3.3 Data collection and processing

The optimized crystals from the additive screens were cryoprotected by briefly soaking in the crystallization buffer containing 25% (v/v) ethylene glycol and were flash-frozen in liquid nitrogen. Because *CnASADH* crystals grew at 10% PEG8000, a thick skin of PEG was found covering the drops, requiring several techniques in order to remove the skin. These crystals were preliminarily screened in-house with a Rigaku FR-E rotating anode generator equipped with R-AXIS IV image plate detector. The crystal diffracted to 2.6 Å in house, and were further subjected to data collection at a synchrotron X-ray source. A diffraction image from the in-house Rigaku diffractometer is shown in Figure 3.2.

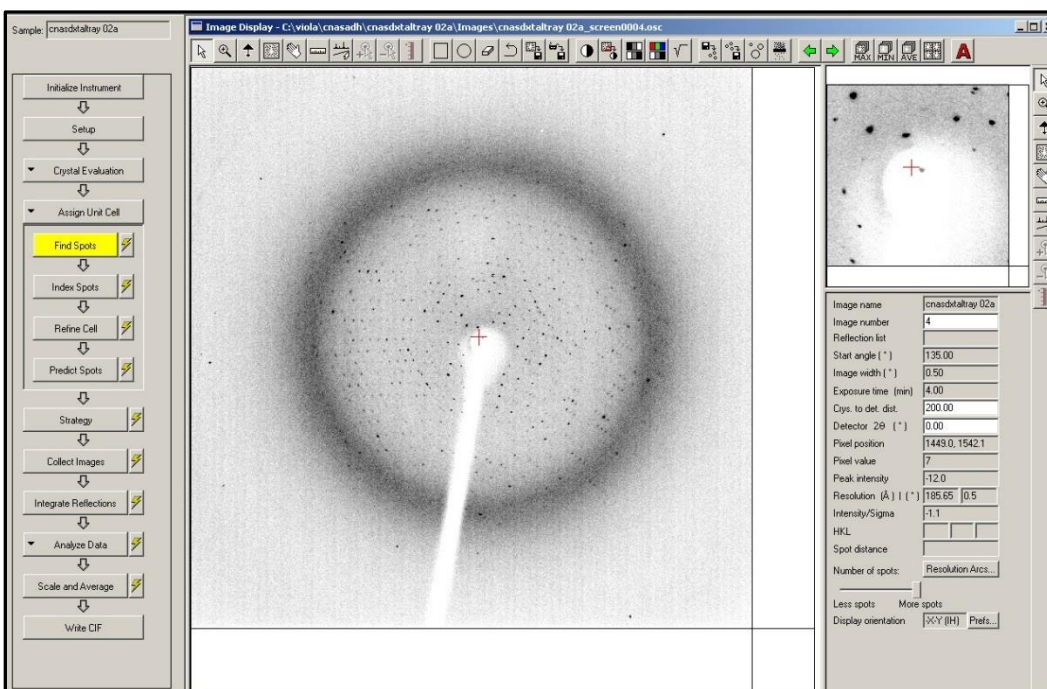


Figure 3.2: A diffraction image of *CnASADH* crystal at Rigaku FR-E source

A complete data set was subsequently collected from a single cryofrozen crystal of *CnASADH* at 100 K using the beamline 21-ID-G of LS-CAT at the Advanced Photon Source (Argonne National Laboratory). The diffraction images were processed and scaled using iMosflm⁶⁵ and AIMLESS from the CCP4 suite⁶⁶. Data collection statistics for this

data set are summarized in Table 3.1.

Table 3.1 Data collection, processing and refinement statistics of *CnASADH*

Data collection and processing	
Diffraction source	APS beamline 21-ID-G
Wavelength (Å)	0.9786
Temperature (K)	100
Detector	MAR mosaic CCD
Crystal-detector distance (mm)	250 mm
Rotation range per image (°)	1
Total rotation range (°)	360
Space group	P2 ₁
a, b, c (Å)	76.59, 130.96, 91.94
α, β, γ (°)	90, 92.87, 90
Resolution range (Å)	66.05 – 2.60
Total No. of reflections	405413
No. of unique reflections	55730
Completeness (%)	100 (100)
R _{merge}	0.094 (0.445)
Redundancy	7.3 (7.1)
⟨ I/σ(I) ⟩	15.2 (4.1)
Overall B factor from Wilson plot (Å ²)	39.1
Structure Refinement Statistics	
Resolution range (Å)	66.05–2.60 (2.67–2.60)
Completeness (%)	100.0 (100.0)
No. of reflections, working set	52836 (3875)
No. of reflections, test set	2849 (234)
Final R _{cryst}	0.181 (0.248)
Final R _{free}	0.220 (0.337)
No. of non-H atoms	
Protein	10796
Ligand	4
Solvent	619
Total	11419
R.m.s. deviations	
Bonds (Å)	0.012
Angles (°)	13
Average B factors (Å ²)	45.0
Ramachandran plot	
Most favored region (%)	97.0
Allowed region (%)	2.8
Outlier region (%)	0.2

Values for the outer shell are given in parentheses

3.3.4 Structure solution and refinement

CnASADH shares 54% sequence identity with the ASADH from *Candida albicans* (PDB code: 3hsk) ²³ with a BLAST score of 395. The atomic coordinates of *CaASADH* were used as the search model for molecular replacement using *Phaser* ⁶⁷ to determine the initial phases. Deleting chain B from the coordinates of this search model gave a solution with a translational-rotational function (TFZ) score of 16.8. This resulting model was then subjected to 20 cycles of rigid-body refinement using the medium resolution data to 3.5 Å using REFMAC5 ⁶⁸, followed by restrained body refinement at the highest resolution (2.6 Å). This refinement gave an initial R_{work} and R_{free} value of 0.31 and 0.37, respectively. The density was further modified with *Parrot* and the structure was built using *Buccaneer* ⁶⁹, an automated protein model building program in the CCP4 suite. The program automatically located most of the protein residues and the model that was generated showed improvement in R values ($R_{\text{work}} = 0.26$ and $R_{\text{free}} = 0.32$). The structure was further built by a combination of iterative rounds of restrained refinement after manual building in COOT ⁷⁰. The stereochemical quality of the final model was checked by PROCHECK. The final structure was visualized and analyzed using PyMOL ⁷¹ and surface calculations were conducted using PDBePISA ⁷². Atomic coordinates and structure factors have been deposited in the Protein Data Bank with accession code 5cef after revalidation with PDB_REDO ⁷³. The final refinement statistics are summarized in Table 3.1.

3.3.5 Results and discussion

3.3.5.1 Overall structure of *Cryptococcus neoformans* ASADH

Full length *CnASADH* contains 365 amino acids, and the enzyme crystallized in the

monoclinic space group $P2_1$ with four molecules in the asymmetric unit, giving a Matthews coefficient of $2.96 \text{ \AA}^3 \text{ Da}^{-1}$ and a solvent content of $\sim 58\%$. The final electron density map was of good quality and allowed nearly complete building of the structure from residues 4-189 and 193-365 for each monomer. Each monomer lacked interpretable electron density for the first three amino acids and for residues 190-192. The four monomers in the asymmetric unit represent the functional dimer of dimers for this enzyme (Figure 3.3a). These dimers are nearly identical, with an r.m.s.d. of 0.19 \AA between chains A and B and 0.11 \AA between chains C and D. This oligomeric assembly has been further supported by native PAGE electrophoresis (Figure 3.3 b) which suggest a molecular weight of about 160 kDa that is consistent with this assembly. The structure of *Cn*ASADH belongs to the Rossmann-fold superfamily of pyridine-linked dehydrogenases, sharing the same overall monomeric structural features as the other ASADHs whose structures have been determined. Each monomer is composed of an *N*-terminal coenzyme binding domain assembled from residues 1-154 and 346-361, and a *C*-terminal catalytic and dimerization domain consisting of residues 155-345. The NADP binding domain consists of mixed β -strands flanked on both sides with α -helices, with 7 β -strands, 5 α -helices and two 3_{10} helices, while the *C*-terminal domain consists of 6 β -strands 6 α -helices and a single 3_{10} helix that represent the catalytic site and the dimerization interface. This fungal ortholog most closely resembles the ASADH structure from *Candida albicans*²³, with an overall r.m.s.d. of 0.85 \AA for the backbone atoms and only some minor structural differences⁴¹ (Figure 3.3c).

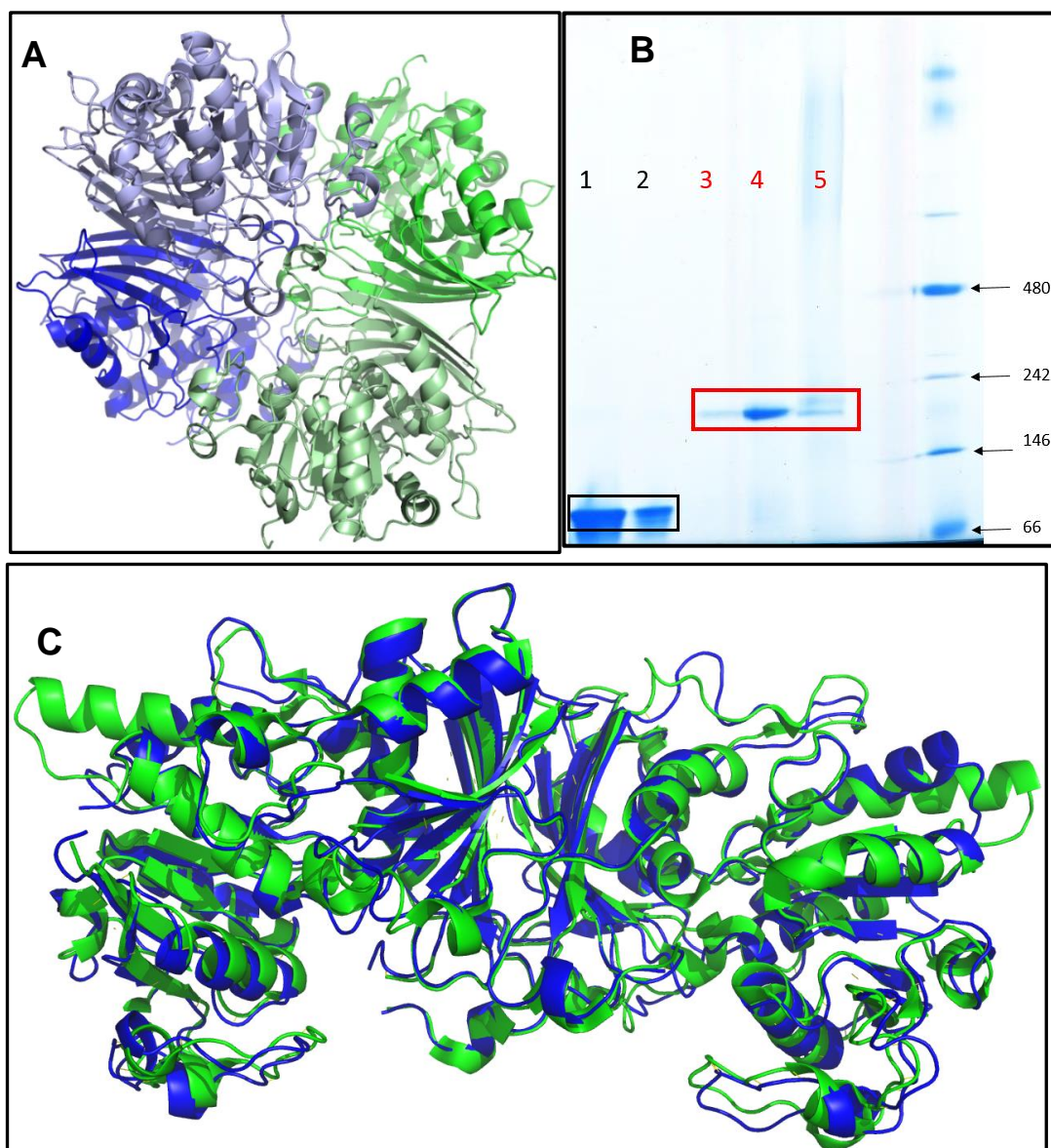


Figure 3.3: (a) Overall structure of aspartate semialdehyde dehydrogenase from *Cryptococcus neoformans*. Each monomeric unit is shown in dark and light colors, with the dimers colored blue and green. b) Native PAGE electrophoresis of different ASADHs on 3-12% bis-tris gel. Lane 1 and 2 corresponds to bacterial ASADHs *S. pneumonia* and *V. cholera* ASADH respectively. Lane 3, 4 and 5 represents fungal ASADHs that corresponds to *A. fumigatus*, *C. albicans* and *C. neoformans* ASADH respectively. The rightmost lane shows the molecular weight marker in kDa. (c) Superposition of a dimer of *Cn*ASADH (blue) with the *Ca*ASADH (green) structure.

3.3.5.2 Secondary structure arrangement and comparison

The structure of the coenzyme binding domain in *Cn*ASADH starts with a beta strand followed by an alpha helix connected to two short beta strands (β_1 - α_1 - β_2), representing the β - α - β motif of a Rossmann fold present in the typical ASADH family (Figure 3.4). This motif is then linked to a 45 residue connecting region composed of two short helices, α_2 and α_3 , one short beta strand, β_3 , and a 3_{10} helix, η_1 , located primarily on the surface and also involved in cofactor binding (Figure 3.4). There is a second β - α - β motif after this surface loop (β_4 - α_4 - β_5) that is highly conserved among all ASADHs. The *Cn*ASADH also contains a third β - α - β motif (β_6 - η_2 - α_5 - β_7), where an extra 3_{10} helix, η_2 , is present between β_6 and α_5 , and this motif is less conserved in different ASADHs. This β_7 sheet is then connected to a conserved helix α_6 and is directed towards the first β -strand (β_8) of the dimerization domain.

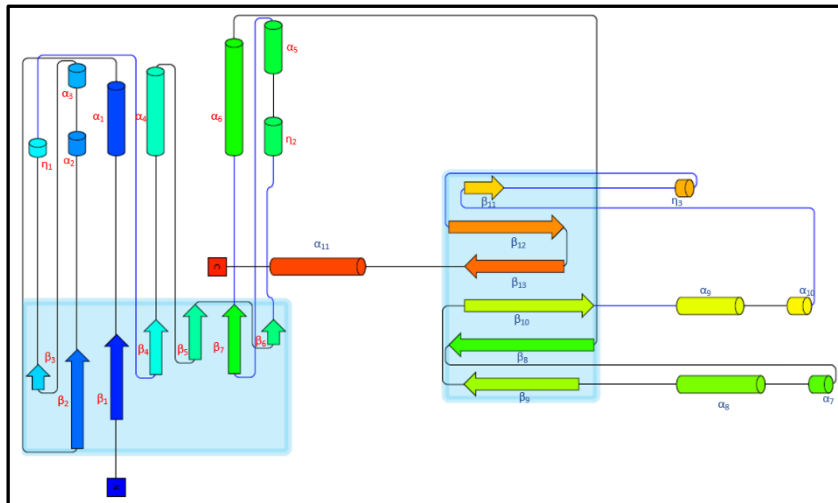


Figure 3.4: Topology diagram showing the secondary structural arrangement of a *Cn*ASADH monomer with the β -sheets inside light blue shaded boxes and the α -helices outside. Each β -sheet and α -helix is numbered in increasing order starting from the N-terminal.

The helical subdomain found in bacterial ASADHs (helix-turn-helix)^{24, 27} is absent in *Cn*ASADH (Figure 3.5) and this region is replaced by two residues without significant electron density suggesting the presence of a somewhat flexible region. This flexible region is followed by two helices, $\alpha 7$ and $\alpha 8$, that are similar to the *Ca*ASADH structure. The helix $\alpha 8$ is connected to an 18 residue surface linker which is structured into two short beta strands in *Ca*ASADH, and the remaining structural arrangement is similar to *Ca*ASADH with minor difference in the length of the helix and the beta strands.

3.3.5.3 Comparison to related ASADHs structures

There has been only a single published structure of a fungal ASADH with bound cofactor²³ and, despite significant effort to grow NADP-bound crystals and few moderate inhibitor soaked crystals of *Cn*ASADH, none of these crystals diffracted to better than 5 Å. The loop that was not modeled into this structure of *Cn*ASADH because of missing density was also absent in the previously determined *Ca*ASADH structure, suggesting that this is an intrinsically flexible and disordered region in the absence of bound substrate. The $\alpha 5$ helix in *Cn*ASADH is four residues shorter than the comparable helix in *Ca*ASADH but is similar in length to the other bacterial and archaeal orthologs. The active site cysteine nucleophile in *Cn*ASADH is found to be present in a single conformation, positioning at the end of a conserved helix ($\alpha 5$) similar to the orientation observed in the bacterial ASADHs. In contrast, in the other fungal ASADH from *C. albicans* this nucleophile is seen to be more flexible and is present in multiple conformations in that structure.

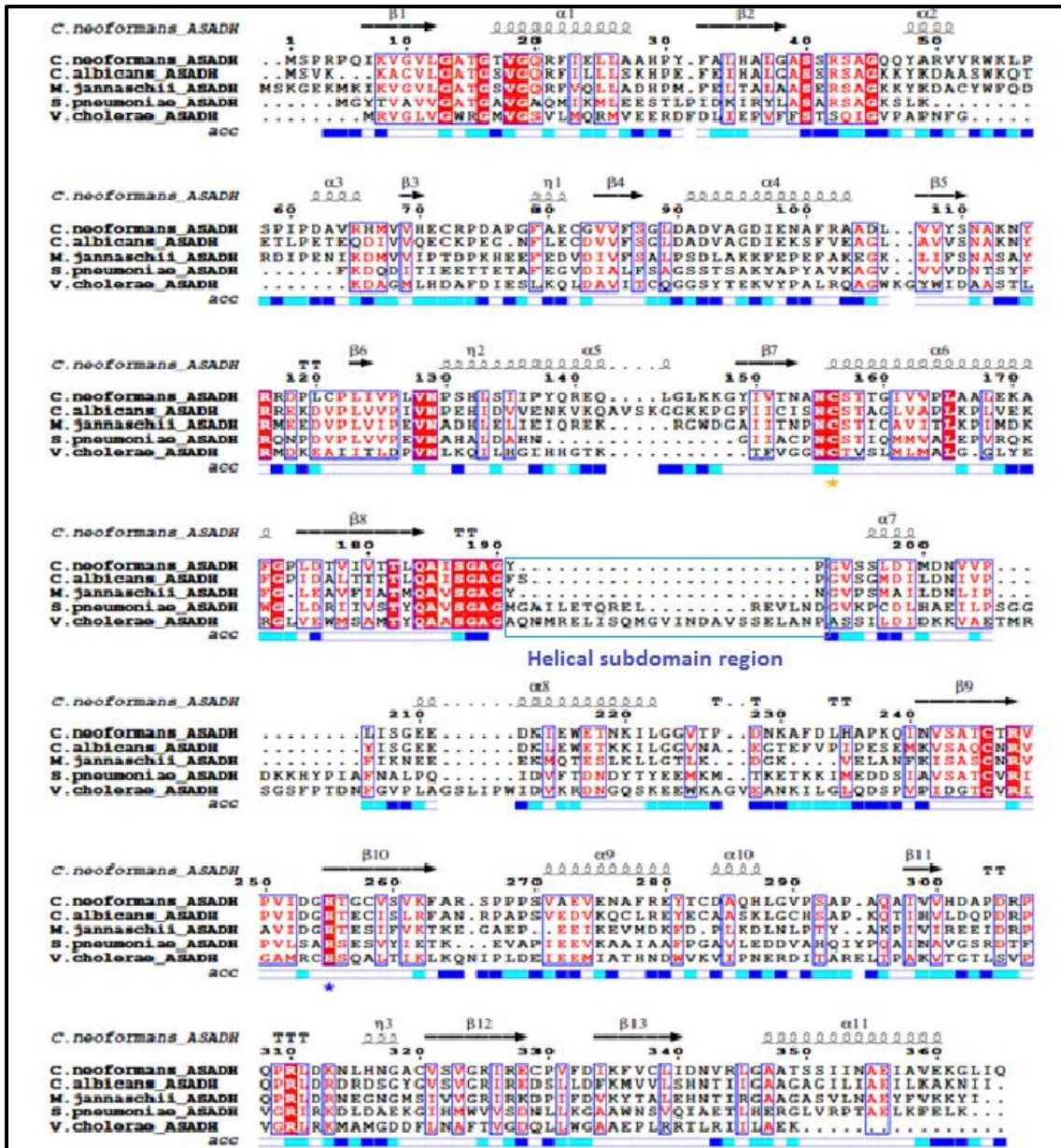


Figure 3.5: Sequence alignment of representative ASADH enzymes from fungal (*C. neoformans*), yeast (*C. albicans*), archaeal (*M. jannaschii*), Gram-positive (*S. pneumoniae*) and Gram-negative (*V. cholerae*) bacterial species. Fully conserved residues are shown in red boxes, residues with conservative mutations are shown in yellow boxes, and active site residues are marked with orange (Cys156) and blue (His255) stars. The helical subdomain region found in the bacterial ASADHs is shown inside a blue rectangle.

3.3.5.4 Positioning of the conserved active site residues

The identity of the critical catalytic functional groups are highly conserved among the

different members of the ASADH family. Superposition of the residues around the *Cn*ASADH active site with the yeast *Ca*ASADH shows that these conserved residues are each located in essentially the same position (Figure 3.6).

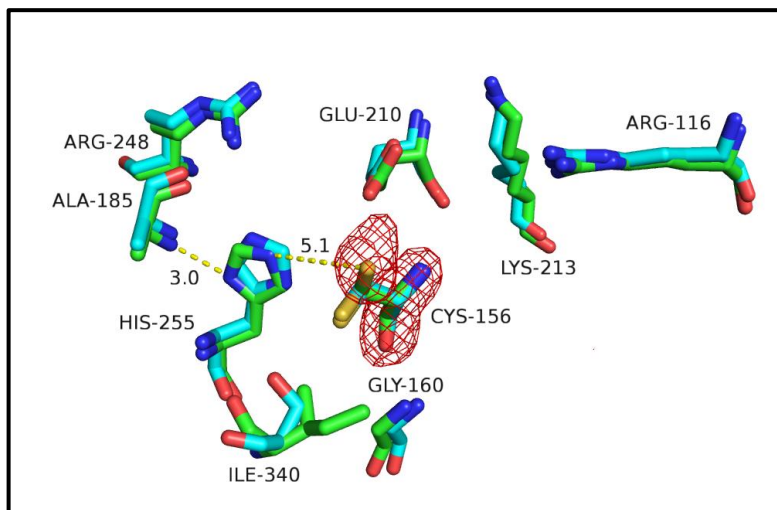


Figure 3.6: Superposition of the active site residues involve in substrate binding and catalysis between *Cn*ASADH (cyan) and *Ca*ASADH (green). Unlike in the *C. albicans* structure, a single conformation was observed for the active site cysteine of *Cn*ASADH, with a greater distance between the sulfur atom of the cysteine nucleophile and the N^ε atom of the histidine acid/base catalyst. Electron density of the cysteine (Cys 156) residue is shown in red.

The only significant active site differences in the apo-enzyme are the orientation of the cysteine nucleophile in a single conformation in *Cn*ASADH and the Ser341 of *Ca*ASADH is replaced by an isoleucine in this new structure. The distance between the sulfur atom of Cys156 nucleophile and the N^ε atom of the His 255 is 5.1 Å in this *Cn*ASADH structure (Figure 3.6), whereas these same atoms are reported to be about 2 Å closer in *Ca*ASADH²³. This increased distance in the *C. neoformans* structure suggests the need for a greater conformational change in the active site in response to substrate binding that would be required to move these active site residues into an optimal position to catalyze this reaction.

While Ser341 has been replaced by isoleucine in this fungal enzyme form, this residue is involved in making the same hydrogen bonding interaction between its backbone amide group and the backbone carbonyl O atom of His255 as was observed in *Ca*ASADH.

3.3.5.5 Binding of an exogenous ligand

The apo-form of *Cn*ASADH was crystallized, and the structure was subsequently determined in the absence of added ligands. However, after final refinement of structure the difference Fourier map at 3σ level showed additional unassigned electron density near the active site base His255, but only in chain A. A search among possible solution components identified ethylene glycol (EG) as the most likely bound ligand, and this density nicely accommodates this molecule. The EG could have come from the crystallization precipitant (6% EG) or from the cryoprotectant solution (25% EG) during flash cooling for data collection. This ligand is anchored at the active site through hydrogen bonding interactions between its oxygen atom and the carbonyl oxygen of His255, and also with the sulfur atom of Cys338 (Figure 3.7). In addition, there are several hydrophobic interactions with other residues in the active site cavity. The B factors for the bound EG are double those for the interacting enzyme side chains, and this is not unexpected for the fortuitous binding of a non-optimized ligand. However, the nature of the ligand interactions within active site can serve as an additional guide for inhibitors designed against the fungal ASADHs. In fact, a structurally related molecule, 3-bromopyruvate, was found to be a selective and moderate inhibitor for only a fungal ASADH, with a K_i value of 0.34 mM for

*Ca*ASADH and no inhibition observed for the bacterial ASADHs²².

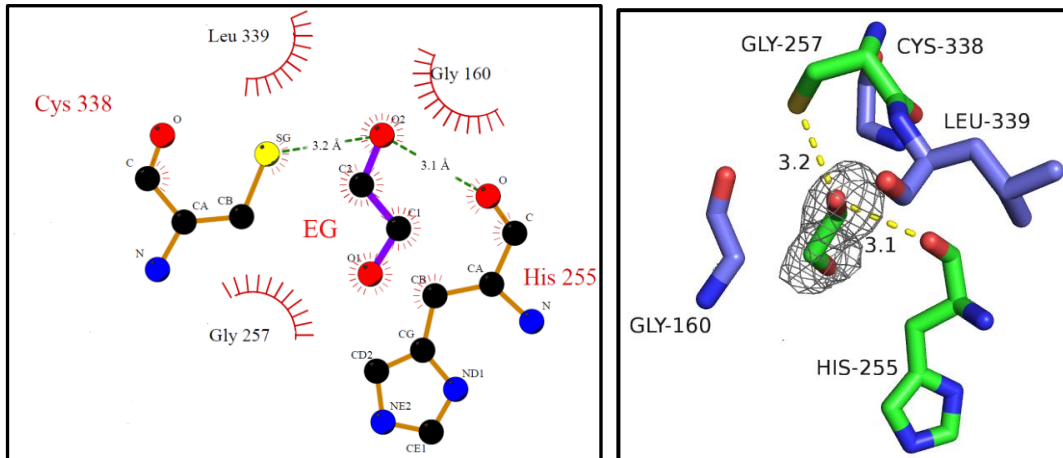


Figure 3.7: (Left) Schematic representation of the interaction made by ethylene glycol (EG) bound at the active site. Residues that make direct hydrogen bonds with the ligand are shown in green dotted lines with their appropriate distance. Residue that forms hydrophobic interactions with the ligand are displayed as labeled arcs with radial spokes that point towards the ligand atoms with which they interact. Right) Representative electron density (grey mesh) of ethylene glycol bound near the active site of *Cn*ASADH.

3.3.5.6 Tetramer interface and oligomeric arrangement

*Cn*ASADH has been shown to exist as a tetramer in solution, similar to that observed for the fungal ASADH from *T. rubrum*³¹. The four molecules in the asymmetric unit share an extensive contact interface that buries a total of 9940 Å² of surface area, utilizing 36 residues within each dimer (A:B and C:D) that can provide up to 14 hydrogen bonds and 3 salt bridges between chains A and B, and a similar set of contacts between chains C and D. There are also cross interactions between chains A and C, with 8 residues making 4 hydrogen bonds, whereas chains B and D interact in a different fashion with 9 residues from chain B interacting with 11 residues from chain D, producing 1 salt bridge and 4 hydrogen bonding interactions. The three pairs of salt bridges, Glu211-Arg325, Glu211-

Arg327 and Glu215-Lys335, that are formed between chains A-B and chains C-D, as well as an additional salt bridge between Lys55 (chain B) and Asp198 (chain D) are not present in the *Ca*ASADH structure. This suggests that the additional salt bridge interactions from different chain assist in the formation and stabilization of the dimers of dimers found in the *Cn*ASADH structure.

3.3.6 Conclusions

*Cn*ASADH is a potential antifungal drug target. The structure of *Cn*ASADH in complex with ethylene glycol has been determined to 2.6 Å resolution. *Cn*ASADH possess similar overall structure to the most closed related yeast ASADH (*Ca*ASADH). However, there is a difference in biological assembly between *Cn*ASADH (dimer of dimer) and *Ca*ASADH (dimer), and this information will be helpful in designing antifungal drug targeting the interface of the dimers.

3.4 *Af*ASADH crystal screening

(Text and figures in this section are adapted from Dahal et. al., Acta Cryst F., 2015)

Preliminary screening of crystallization condition for *Af*ASADH (14 mg/ml) was carried out in 48-well Hampton VDX plates using Hampton Index screening, as well as in-house customized crystallization kits. The hanging drops in the initial crystallization screening consisted of 1 µL of protein solution plus 1 µL of reservoir solution, with each reservoir solution consisting of 200 µL of the unique reagents from each screening kit. Crystals were obtained from condition 3 of Hampton Index Screen 1 after 48 h, which consisted of 2 M ammonium sulfate, 100 mM bis-tris, pH 6.5. This initial hit was further optimized by varying the concentration of ammonium sulfate (from 1.5 to 2.5 M), pH (Tris HCl, pH 5.5, HEPES, pH 7.5, Tris-HCl, pH 8.5) and buffer concentration (50 to 100 mM).

The drops were found to be precipitated at 2.2 M or higher concentration of ammonium sulphate, with clear drops below 2.2 M, whereas pH plays a vital role with immediate precipitate at both pH 5.5 and 8.5 but crystals appeared at pH 6.5 and 7.5. Changing the concentration of protein didn't show a significant effect on crystal growth, with growth of crystals at both 10 mg/ml and 30 mg/ml. Well-formed, hexagonal crystals (~ 40 μ m, Figure 3.8) grew from the 1.9 M ammonium sulfate and 100 mM bis-tris, pH 6.5, at 293 K. The crystals were either soaked or co-crystallized with 5 mM NADP (cofactor), and also with several moderate inhibitors that were identified from fragment library screening.

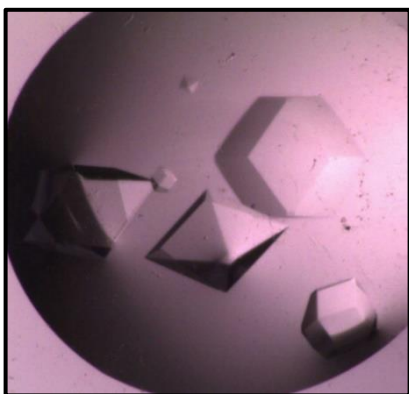


Figure 3.8: Initial hits from Index screening from *AfASADH* at 14 mg/ml under 2 M ammonium sulphate and bis-tris, pH 6.5.

3.4.1 Data collection and processing

The crystals from *AfASADH* (apo-form and ligand-soaked form) were cryoprotected with the reservoir solution containing 20% (v/v) ethylene glycol. The soaking experiments performed in this cryosolution contained 20 mM final concentrations of the cofactor and each inhibitor, with soaking for 1 min and then flash freezing in liquid nitrogen. Several crystals diffracted between 2.8 – 3.2 Å on our in-house Rigaku FR-E diffractometer equipped with an R-Axis IV image plate detector. Six complete data sets, from the apo-form, the cofactor soaked and four moderate inhibitor soaked crystals were

subsequently subjected to data collection at the SBC 19-BM beamline at Argonne National Lab using a MAR 335 detector. Each data set consisting of 220 frames was collected with a crystal-to-detector distance of 250 mm, an oscillation width of 0.5° and an exposure time of 1 s per frame (Table 3.2). The diffraction data was integrated and scaled using iMOSFLM⁶⁵ and AIMLESS from CCP4 suite⁷⁴ and data cutoff was analysed using the signal to noise ratio at the highest resolution shell.

3.4.2 Structure solution and refinement

The apo-form of the *AfASADH* structure was solved by molecular replacement using Phaser with our published structure of *Candida albicans* ASADH (PDB code: 3hsk)²³ as the search model. The search model gave a solution with a TFZ score = 17.1 using a monomer of *CaASADH*, an enzyme that shares 55% sequence similarity with *AfASADH*. The initial R_{work} and R_{free} was found to be 0.34 and 0.39, respectively, after 25 cycles of rigid body refinement to a medium resolution of 3.5 Å, followed by a restrained body refinement at 2.38 Å using REFMAC5⁶⁸. The model was rebuilt using the program BUCCANEER which automatically built most of the residues. The final model was built using numerous cycle of restrained refinement in REFMAC and manual rebuilding in COOT. The final R_{work} and R_{free} was found to be 0.20 and 0.25, respectively, and the stereochemical quality was checked using PROCHECK⁷⁵. Ramachandran outliers were observed to be considerably high due to poor electron density at the flexible loop region and also some amino acids being next to proline residues. Pymol⁷¹ was used to visualize the final structure and PDBePISA⁷² was used for surface calculations. The final model was deposited in the Protein Data Bank (<http://www.rcsb.org>),⁷⁶ with PDB accession code 5JW6. The phasing and final refinement statistics are shown in Table 3.2.

Table 3.2 Data collection, processing and refinement statistics of AfASADH

Values for the outer shell are given in parentheses.

Data collection and processing	
Diffraction source	APS 19-BM beamline.
Wavelength (Å)	0.9792
Temperature (K)	100
Detector	Mar 335CCD
Crystal-detector distance (mm)	250
Space group	$P3_121$
a, b, c (Å)	94.50, 94.50, 202.14
α, β, γ (°)	90, 90, 120
Mosaicity (°)	0.19
Resolution range (Å)	75.86 – 2.39
Total No. of reflections	264962
No. of unique reflections	42496
Completeness (%)	100 (99.9)
Redundancy	6.2 (5.0)
$\langle I/\sigma(I) \rangle$	9.2 (3.2)
R_{merge}	0.060 (0.224)
Overall B factor from Wilson plot (Å ²)	34.1
Refinement statistics	
Completeness (%)	100.0
No. of reflections, working set	40287 (2906)
No. of reflections, test set	2141 (184)
Final R_{cryst}	0.201 (0.240)
Final R_{free}	0.250 (0.284)
No. of non-H atoms	5598
Protein	5466
Ligand	25
Solvent	107
R.m.s. deviations	
Bonds (Å)	0.018
Angles (°)	1.92
Average B factors (Å ²)	39.0
Protein	39.4
Ligand	47.6
Solvent	35.3
Ramachandran plot	
Most favored (%)	95.0
Additionally allowed (%)	3.9
Outliers (%)	1.1

3.4.3 Results and discussion

3.4.3.1 Overall structure

The crystal structure of *Af*ASADH was determined at 2.38 Å resolution by molecular replacement using *Ca*ASADH²³ as the search model. The entire sequence (363 amino acid full length) was fitted into electron density, except for amino acids 1-3 and 189-190 from each monomer that lacked interpretable electron density. *Af*ASADH displays as a crystallographic dimer (Figure 3.9) in its crystalline state similar to *Ca*ASADH²³. However, this enzyme is functionally active as a dimer of dimers in solution, consistent with the other fungal ASADHs^{31,41}. Each asymmetric unit contains two monomers, and a comparison of the monomer structures yields an rmsd value of 0.254 Å, indicating that the monomers are nearly identical. Similar to other dehydrogenases, *Af*ASADH belongs to the Rossmann-fold superfamily of pyridine-linked dehydrogenases and shares similar overall structural features to those of other ASADHs. Each monomer is comprised of an *N*-terminal coenzyme binding domain (residues 1-152 and 346-359) and a *C*-terminal catalytic and dimerization domain (residues 153-345).

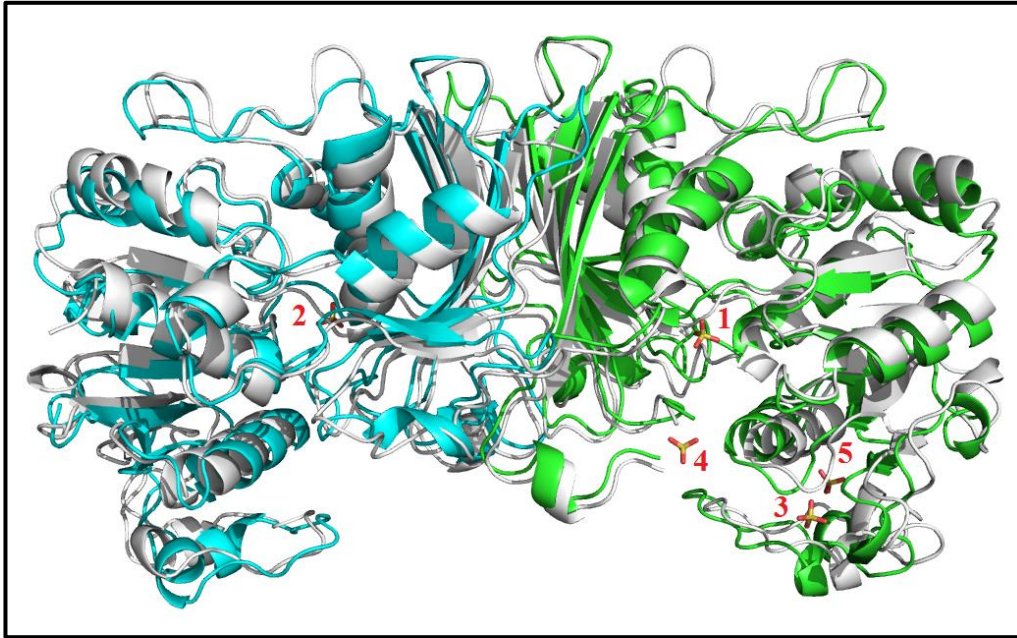


Figure 3.9: Overall structure of aspartate semialdehyde dehydrogenase from *A. fumigatus*. The monomers of this crystallographic dimer are shown in green and blue, with the bound sulfate molecules (numbered 1-5) in yellow and pink. The structure of *AfASADH* is superimposed over the *CnASADH* structure (in grey). The overall structure is similar, with only minor differences in the orientation of some secondary structural elements.

3.4.3.2 Absence of cofactor and inhibitor binding

Despite crystallization in the presence of excess concentrations of the cofactor NADP and four different moderate inhibitors, no electron density was found corresponding to either NADP or the inhibitors in any of these solved structures. Instead, five sulfate molecules were found bound near the substrate binding site and also near the cofactor binding sites (Figure 3.9). Because the crystallization solution contains nearly 2 M ammonium sulfate, this high concentration of sulfate anion likely competes with and prevents either the cofactor or the inhibitors from binding at their respective sites. Attempts to lower this sulfate competition by decreasing the sulfate concentration yielded only clear crystallization drops at sulfate concentrations lower than 1.8 M. Switching to different

anions of ammonium salts such as phosphate, chloride, fumarate did not support crystal growth, suggesting that the presence of sulfate helps to stabilize this crystal form. Microseeding of apo-*Af*ASADH crystals into precipitation solutions containing different molecular weight PEGs instead of ammonium sulfate also did not produce any crystal growth.

3.4.3.3 Secondary structural arrangement

The *N*-terminal domain of *Af*ASADH starts with a β -strand followed by an α helix and two short β -strands (β_2 and β_3) completing the β - α - β motif of the Rossmann-fold (β_1 - α_1 - β_2 - β_3 , aa 7-39) that supports the NADPH binding site in this dehydrogenase family (Figure 3.10). This highly conserved motif is connected to a long surface loop (aa 40-81) consisting of two 3_{10} helices (η_1 , η_2) and two short α helices (α_2 , α_3) that are primarily involved in cofactor binding. This surface loop is connected to a second β - α - β motif (β_4 - α_4 - β_5) region (aa 82-108) which is also highly conserved in the ASADH family. The third, less conserved β - α - β motif is replaced in *Af*ASADH by a long α helix (α_5) and a short β strand (β_6). This region is connected by a long conserved helix (α_6 , aa157-170), followed by the first β strand (β_7) of the dimerization domain. The helical subdomain, consisting of a helix-turn-helix, that is found in many bacterial ASADHs ²⁷ is absent in *Af*ASADH (Figure 3.11) and is replaced by two residues (aa 189-190) with no significant electron density, consistent with the other fungal ASADH structures. The catalytic and dimerization domains of *Af*ASADH are more similar to the other fungal ASADHs than to the bacterial ASADHs, with mixed groups of parallel β -strands assembled with flanking α -helices on both sides. There is a slight variation in the length of each α -helices and β -strands in each

secondary structure compared to other fungal ASADHs, but the overall structural arrangement is similar among all fungal ASADHs.

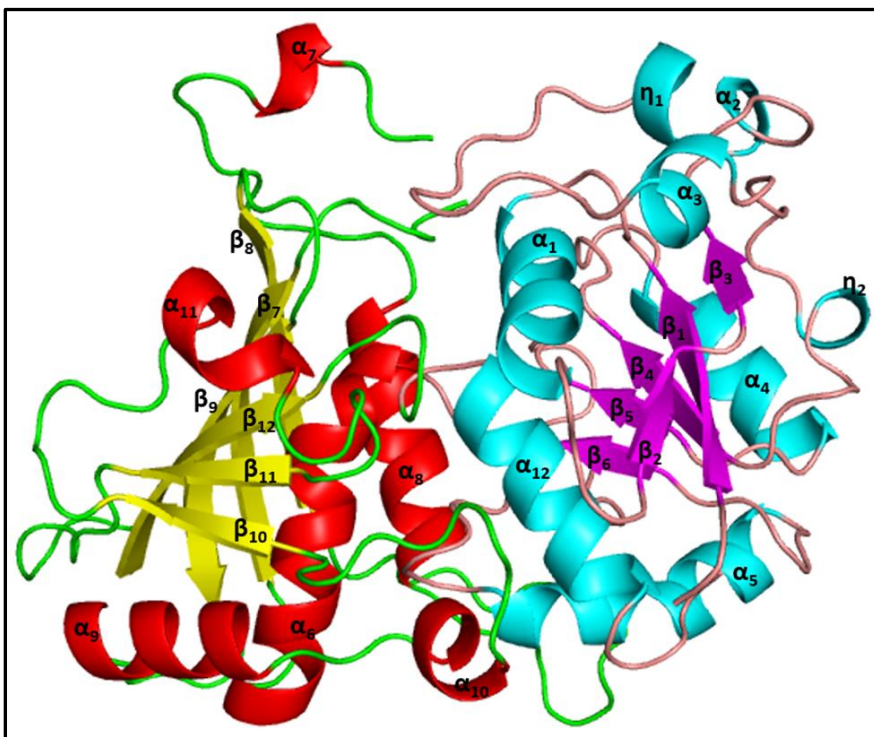


Figure 3.10: *Af*ASADH monomer showing the secondary structural arrangement. The N-terminal domain β -sheet regions are shown in purple, and the α -helices are shown in cyan. For the C-terminal domain the β -sheet regions are shown in yellow, and the α -helices are shown in red, with numbering in increasing order starting from the N-terminus.

3.4.3.4 Comparison with related structures

Only three prior structures of ASADHs have been determined from pathogenic fungal species; i.e., *Cryptococcus neoformans* (*Cn*ASADH), *Candida albicans* (*Ca*ASADH), and *Trichophyton rubrum* (*Tr*ASADH). Two of these fungal enzyme forms, *Ca*ASADH and *Tr*ASADH, have been solved with the cofactor NADP bound. In an attempt to determine the structure of different inhibitors bound to *Af*ASADH we have collected and processed several data sets from crystals that have been either soaked or co-crystallized with the cofactor NADP and with several moderate inhibitors. Unfortunately,

all of these data sets showed electron density corresponding to sulfate ions bound at both the active site and the cofactor binding site, but with no electron density for any of these ligands. Superposition of the *Af*ASADH dimer with the dimer of *Cn*ASADH shows no significant difference in the overall structure, with only slight differences in the orientation and length of some α -helices and β -sheets (Figure 3.10). The segment containing amino acids 189-190 with missing electron density was also missing in the other fungal ASADH structures, with the exception of a modelled loop in *Tr*ASADH, suggesting that this loop is highly mobile and quite flexible. The conformation of this loop plays an important role in NADP binding. The formation of a dimer of dimers in these fungal ASADHs helps to stabilize this loop in a productive conformation to assist in binding the cofactor³¹. The rmsd value between the aligned *Af*ASADH structure and the other fungal ASADH structures was found to be 1.79 Å for *Cn*ASADH and 1.64 Å for *Ca*ASADH, based on 716 C α aligned residues. However, this difference is only 0.62 Å for the alignment with *Tr*ASADH, showing that the *Af*ASADH structure is more closely related to this enzyme form.

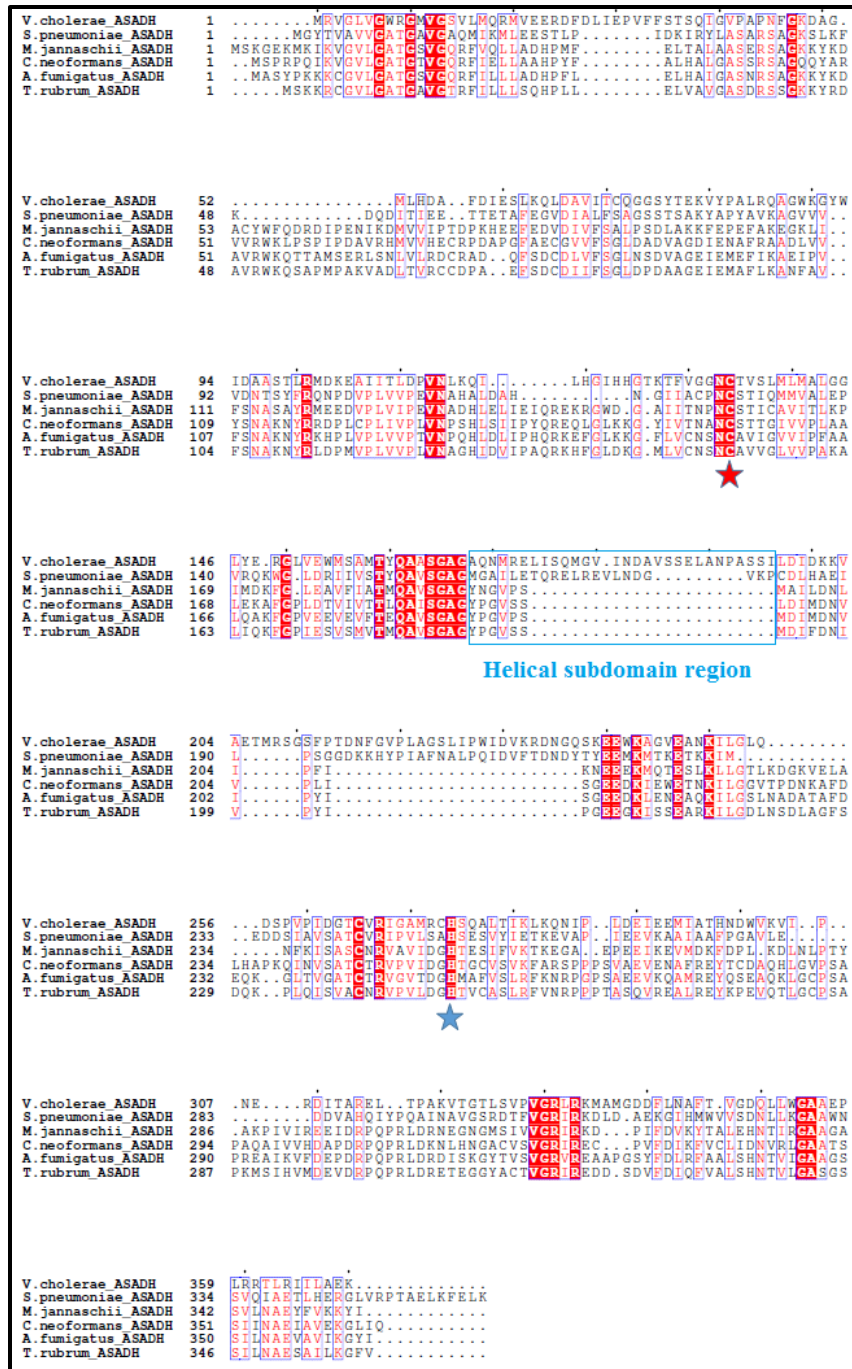


Figure 3.11: Multiple sequence alignment of ASADH enzymes from fungi *Aspergillus fumigatus*, *Cryptococcus neoformans*, and *Trichophyton rubrum*, bacteria *Streptococcus pneumoniae*, and *Vibrio cholera* and archae *Methanocaldococcus jannaschii*. Fully conserved residues are shown with a red background, conserved residues are shown with red letters and active site residues are marked with red and blue stars. The helical subdomain of the bacterial ASADHs is outlined in a blue rectangle.

3.3.3.5 Active site comparison

The active sites of ASADHs are highly conserved, with an identical constellation of functionally essential amino acids found among the different members of this enzyme family. Superposition of the active site of *Af*ASADH with *Cn*ASADH shows these conserved catalytic residues are each located in the same general positions, but with some changes in the intra-residue distances (Figure 3.12). The sulfur atom of the active site cysteine nucleophile (Cys154) is found in single conformation, as opposed to the multiple conformations seen in *Ca*ASADH²³. This cysteine is positioned at the end of a conserved helix in *Af*ASADH, while in the active site of *Tr*ASADH the cysteine is located in a flexible loop before the helix. The distance between the sulphur atom of Cys154 and N^δ of His251 (acid/base catalyst) is only 3.6 Å in *Af*ASADH, compared to 7.0 Å in the *Cn*ASADH structure (Figure 3.12). Also, the distance between this sulfur atom and O^ε of Glu208 (a substrate binding residue) is 4.0 Å in *Af*ASADH and 7.7 Å in the *Cn*ASADH structure. The distance between each of the other fully conserved residues responsible for substrate binding (Lys211, Arg114, Arg244) are also several angstroms closer in *Af*ASADH compared to the *Cn*ASADH structure. These closer distances between the catalytic residues show that the active site in *Af*ASADH is pre-positioned to make more favorable interactions upon the initial encounter with the substrate at the active site. An active site isoleucine (Ile339) in *Cn*ASADH is replaced by a serine in *Af*ASADH, but this polar residue does not make any new hydrogen-bonding interactions that would contribute to the more compact active site structure in this apo-enzyme.

Several amino acid residues surrounding the active site are altered among different fungal ASADHs. Ala155 in *Af*ASADH is replaced with Ser157 in *Cn*ASADH and

*Ca*ASADH, Ile344 in *Af*ASADH is replaced with a leucine in *Cn*ASADH and *Tr*ASADH. Similarly, Thr342 is replaced with Val343, Leu212 with Ile214, and His340 with Asp341 in *Cn*ASADH. These minor changes in residues around the active site may contribute to the small differences in catalytic properties among these fungal ASADHs. There are also some minor differences in active site structures between *Af*ASADH and both *Ca*ASADH and *Tr*ASADH, but the overall organization of each active site is found to be quite similar among these fungal ASADHs.

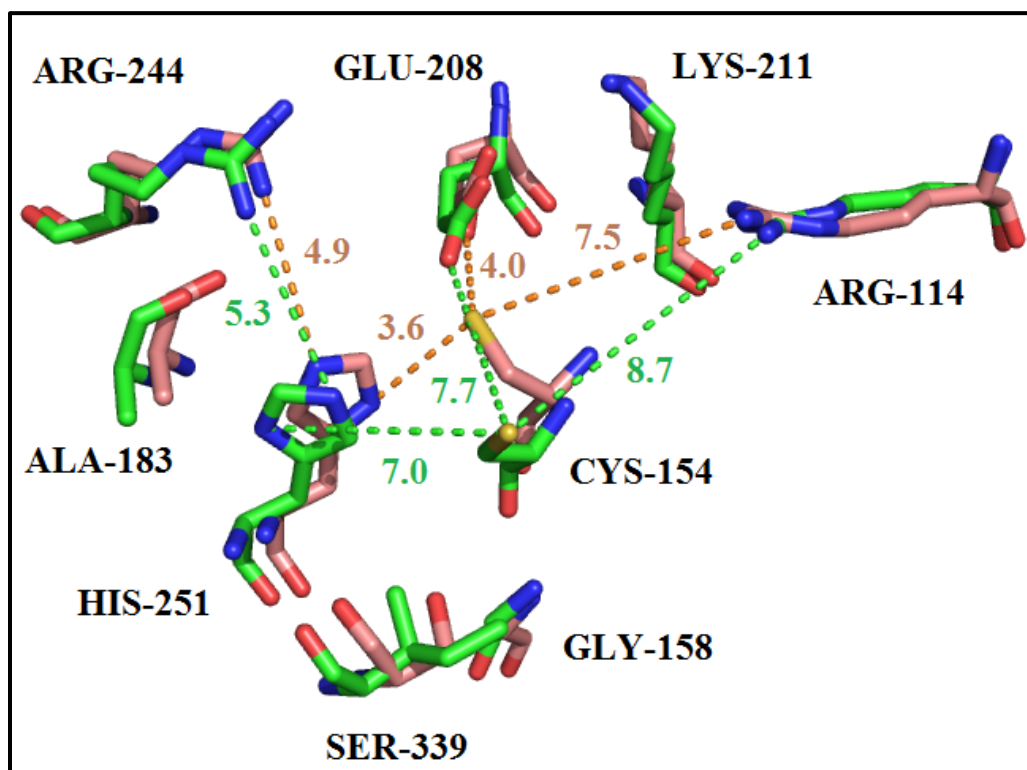


Figure 3.12: Superposition of the residues in the active site of *Af*ASADH (pink) and *Cn*ASADH (green). Each critical catalytic residue is further apart in the *Cn*ASADH structure, while they are found to be several angstroms closer in the *Af*ASADH structure.

3.3.3.6 Binding of an exogenous ligand

The apo form of *Af*ASADH was crystallized in the presence of 1.9 M ammonium sulfate as the precipitant. After final refinement of the structure, the difference Fourier

maps at 3σ level showed some additional unassigned density near the active site of each monomer as well as in the cofactor binding site of chain A. Initial speculation that the unassigned density corresponds to sulfate molecules proved accurate, with an excellent fit into the electron density. These anions are most likely bound at these sites because of the high concentration of sulfate in the crystallization precipitant. The sulfate ion fits nicely in the electron density with an average B factor of 26.5\AA^2 at the active site of each monomer and an occupancy of one (Figure 3.13 a). Each bound anion makes several hydrogen bonding interactions with active site residues and with residues in the cofactor binding site. The O₃ oxygen atom of sulfate 1 in chain A, and sulfate 2 in chain B, each have hydrogen bonding interactions with the S^γ atom and N atom of the active site cysteine (Cys154) molecule in each monomer, with a distance of 3.25 Å and 2.88 Å, respectively (Figure 3.13, panel A). The other oxygen atoms of this bound sulfate (O₂ and O₄) make hydrogen bonding interactions with additional residues around the active site, including Asn153, Arg114 and Lys211. The sulfate molecule bound near the cofactor binding site (sulfate 3) hydrogen bonds with residues Thr15, Ala39, Ser40, and Ser43 (Figure 3.13, panel B), while sulfate 4 makes similar interactions with Ser17, Ala186 and Ala187 (Figure 3.13, panel C). Another sulfate molecule is found bound on the surface, interacting with Ser61 and Arg63 (Figure 3.13, panel D). All of these sulfate molecules are bound to both subunits, except for sulfate 2 which is bound only to chain B. The B factor for the sulfates bound at active site was found to be 25.81\AA^2 and 27.3\AA^2 for chain A and B, respectively and the B factor for the other sulfate molecules are 52.8\AA^2 and 64.5\AA^2 . The surface-bound sulfate also has a higher B factor of 67.4\AA^2 , which is not unusual for non-optimized ligand binding through only two hydrogen-bonds at a surface site. Superposition of the bacterial *Streptococcus*

pneumoniae ASADH (*Sp*ASADH) structure with this *Af*ASADH structure shows that the acetate moiety from the crystallization buffer that is bound near the active site of this bacterial ASADH⁵¹ is in the same location and makes similar interaction to those with the sulfate bound at the active site of *Af*ASADH. This sulfate molecule bound to *Af*ASADH superimposes perfectly with the sulfate bound at the active site in *Tr*ASADH structure³¹.

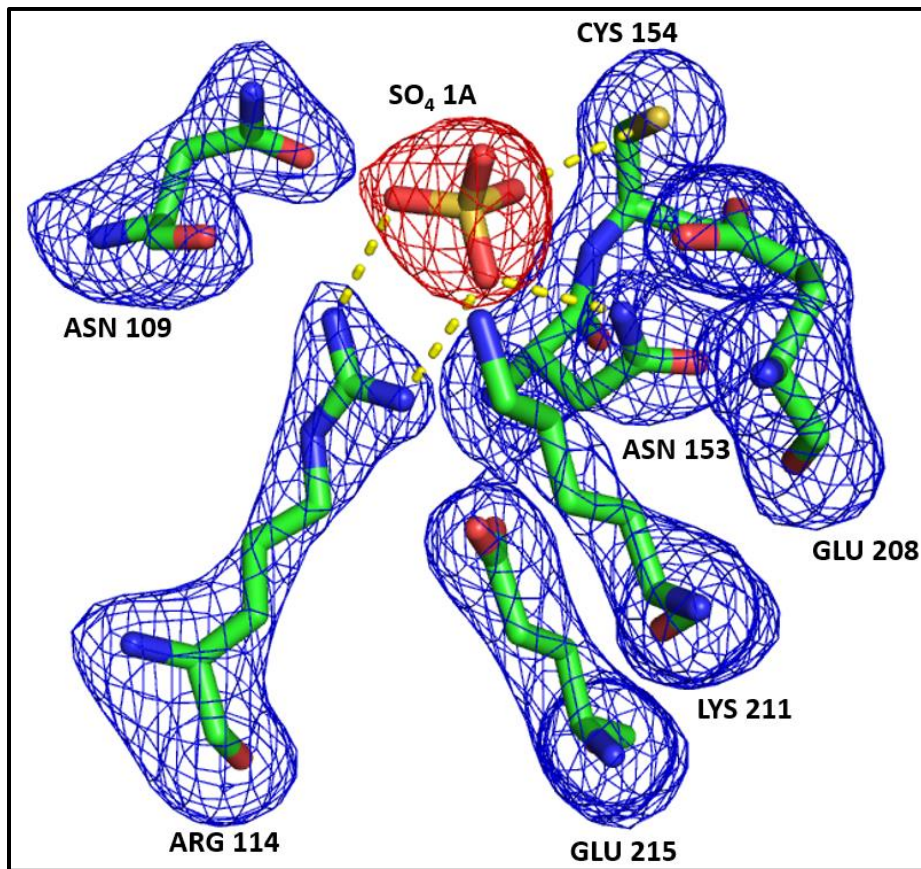


Figure 3.13: a) Representative electron density and modelling of amino acid side chains and sulfate ion bound near the active site.

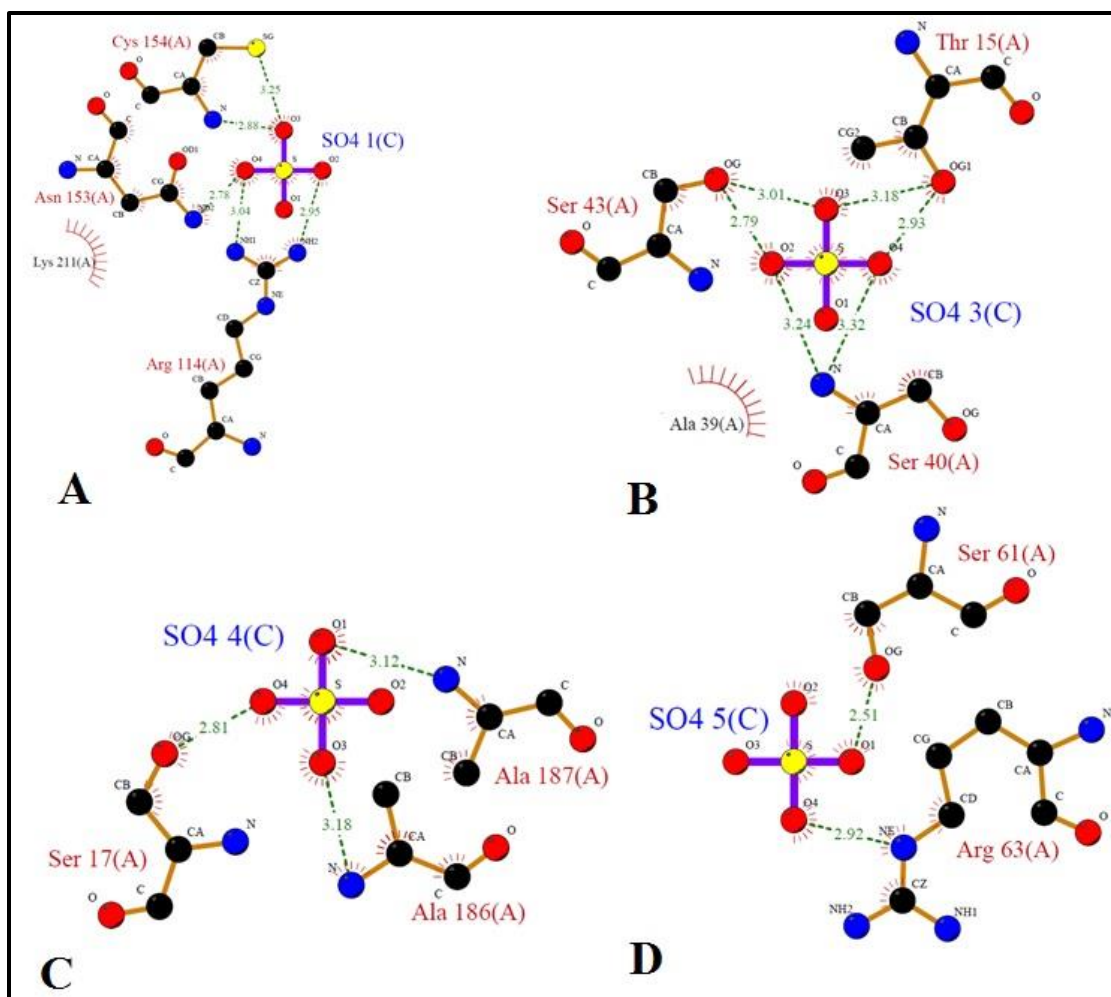


Figure 3.13 b) Ligplot diagram of sulfate molecule bound at the substrate binding site (A), cofactor binding sites (B and C) and on the surface (D) of *AfASADH*. Each sulfate molecule has both hydrogen bonding and hydrophobic interactions with active site residues in each monomer. Direct hydrogen bonds are shown in green dotted lines with their appropriate distance, and hydrophobic interactions are displayed as labelled arcs with each sulfate molecule labelled in increasing order.

3.4.3.7 Differences in oligomeric arrangement

There are two monomers in the asymmetric unit in this crystal form of *AfASADH*, similar to what was observed in *CaASADH*. By contrast, in the other fungal enzyme forms

*Cn*ASADH has four monomers and *Tr*ASADH has six monomers in the asymmetric unit in their corresponding crystal forms. However, despite these crystallographic differences the oligomeric state of *Af*ASADH has been found to be a dimer of dimers in solution, confirmed by native gel electrophoresis³¹. The change in oligomeric structure is required to produce an active enzyme in these fungal species; mutations that cause dissociation into dimers results in loss of activity³¹. Crystal packing interactions were analysed using the program PDBePISA⁷², the results of which also concluded that *Af*ASADH likely organizes into a dimer of dimers. The larger buried surface area and higher free energy of dissociation each show the strength of subunit interaction in this *Af*ASADH structure. For the subunit interaction surface in *Af*ASADH 35 residues from monomer A interact directly with 33 residues in monomer B, forming 31 hydrogen-bonding interactions, along with a total of 275 non-bonded contacts. There are also six pairs of salt bridges, with the participation of Glu177 – Arg334, Asp199 – Arg309, Glu209 – Arg321 from chain A to chain B and the corresponding residues from chain B to chain A within each dimer. The higher free energy of subunit dissociation in *Af*ASADH results from a larger buried surface area and a greater number of productive contacts across the subunit interface. This fungal form of ASADH has the largest number of hydrogen-bonding and non-bonding contact among the structurally characterized fungal enzyme family (Table 3.3). The *C. albicans* enzyme has nearly the same number of these interactions, but the absence of any electrostatic bonds between the subunits leads to a lower energy of dissociation. This ensemble of interactions across the dimer interface contribute to the stabilization of the *Af*ASADH structure.

Table 3.3 Buried surface area and energetics of ASADH subunit dissociation

fungals ASADH forms	PDB code	Buried surface area (Å ²)	Free energy of dissociation (ΔG ^{diss}) (kcal/mol)	Salt bridges	Hydrogen bonds	Non-bonding contacts
<i>Af</i> ASADH	5jw6	12660	52.7	6	31	275
<i>Tr</i> ASADH	4zhs	12360	17.9	6	21	212
<i>Cn</i> ASADH	5cef	9940	13.4	6	28	202
<i>Ca</i> ASADH	3hsk	11940	14.8	0	31	261

3.4.4 Conclusions

We presented the first structure of ASADH from the pathogenic fungi *A. fumigatus*, along with a structural and functional comparison between the fungal and bacterial ASADH orthologs. The structure of *Af*ASADH was found to be more similar to that of the other fungal orthologs, but with some critical differences in the orientation of active site functional groups and in the subunit interface region. Structural analysis suggests that the differences observed in biochemical activity among the ASADH enzyme family can be correlated with changes in oligomeric assembly, differences in the strength of subunit interactions, and variations in the interatomic distances between catalytic residues in the active sites of different fungal ASADHs. This expanded structural information of the fungal ASADHs will be useful in structure-guided drug design against fungal pathogens.

3.4.5 Re-screening of *Af*ASADH crystals

Since the crystal structure of *Af*ASADH with the cofactor or the most potent ligand bound didn't show any electron density for the ligands, additional crystal screening was performed to obtain new crystal conditions. The *Af*ASADH crystals were screened against JB screening kit, Hampton index screening and wizard screening kit. Out of 192 conditions,

two condition showed crystalline material which, upon further optimization, yielded diffraction quality crystals. The final optimum conditions are: a) 0.2 M ammonium sulfate, 0.1 M HEPES, pH 7.5, 25% w/v PEG 3350, and b) 35% w/v tacsimate, pH 7.0. These crystals were either soaked or co-crystallized with the inhibitors, and then flash frozen in liquid nitrogen for X-ray data collection.

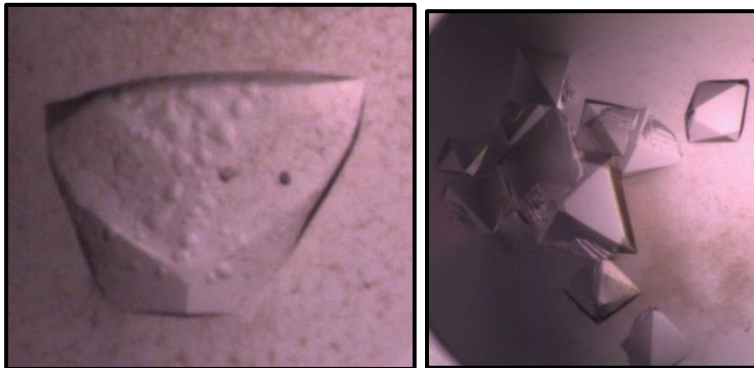


Figure 3.14: Re-screening hits of *AfASADH* sample left) 0.2 M ammonium sulfate, 0.1 M HEPES, pH 7.5, 25% w/v PEG 3350 & right) 35% w/v tacsimate, pH 7.0.

3.5 *BdASADH* crystals screening

Preliminary crystallization screening of *BdASADH* (12 mg/ml) was carried out by hanging drop vapor-diffusion in 48-well plates using both Hampton Index and in-house customized crystallization screening. Initial screening produced several crystals forms, with one condition yielding long rod-shaped crystals after 48 h. After optimization a large number of well-formed rod-shaped crystals (Figure 3.15) were obtained from a single well containing 0.2 M ammonium citrate, pH 7.0, and 18% PEG 3350. The concentration of precipitant (0.1 to 0.3 M), with PEG concentration (10% to 30%), PEG molecular weight (1500 to 8000) and protein concentration (8 mg/ml and 15 mg/ml) were varied in order to obtain diffraction quality crystals. After extensive optimization, the best conditions yielded a large number of long, rod-shaped crystals in a single drop with final condition as 10

mg/ml under 0.2 M ammonium citrate tribasic, pH 7.0, 20% w/v PEG 3350. These crystals were either soaked or co-crystallized with 5 mM NADP, and also with several moderate inhibitors identified from fragment library screening.

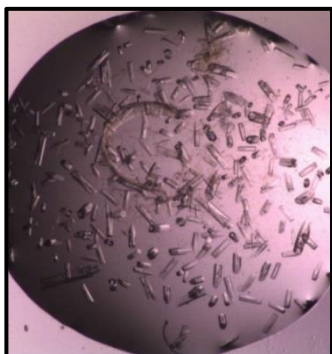


Figure 3.15: Initial hits from Index screening for *BdASADH* at 10 mg/ml under 0.2 M ammonium citrate tribasic, pH 7.0, 20% w/v PEG 3350.

3.5.1 Data collection and processing

The crystals from *BdASADH* (apo-form and ligand-soaked forms) were cryoprotected with the reservoir solution containing the final crystallization components plus 15% (v/v) ethylene glycol and 5 mM NADP as well as each inhibitor at 10 times their K_i concentrations, with soaking for 1 min and then flash freezing in liquid nitrogen. Crystals that diffracted to moderate resolution on our in-house Rigaku FR-E diffractometer, including the apo-form, cofactor-soaked, and inhibitor-soaked forms, were subsequently subjected to data collection at the GM/CA 23-ID-B beamline at Argonne National Lab. The diffraction data was integrated and scaled using XDS⁷⁷ and AIMLESS from CCP4⁷⁴ suite. The structure of the *BdASADH* structure was solved by molecular replacement using Phaser with our published structure of *Candida albicans* ASADH (PDB code: 3hsk)²³ as the search model (Table 3.4). The final model was built using numerous cycle of restrained refinement in REFMAC⁶⁸ with the stereochemical quality checked using PROCHECK.⁷⁸ Pymol⁷⁹ was used to visualize the final structure and PDBePISA⁷² was used for surface calculations. The final models were deposited in the Protein Data

Bank (<http://www.rcsb.org>), with PDB accession codes 6C85 and 6C8W for the inhibitor complex and the NADP complex, respectively.

Table 3.4 Data collection, processing and refinement statistics of *Bd*ASADH

enzyme-ligand complex	<i>p</i> -benzoquinone	NADP
Data collection and processing		
Diffraction source		GM/CA 23ID-B
Wavelength (Å)		1.0332
Temperature (K)		100
Detector		Dectris Eiger-16m
Crystal-detector distance (mm)		300
Rotation range per image (°)		0.5
Total rotation range (°)		360
Exposure time per image (s)		1
Space group		<i>P</i> 3 ₂ 21
<i>a</i> , <i>b</i> , <i>c</i> (Å)	107.35, 223.10	107.35, 107.46, 223.07
α , β , γ (°)	90, 90, 120	90, 90, 120
Mosaicity (°)	0.35	0.25
Resolution range (Å)	85.82 – 2.40	47.84-2.60
Total No. of reflections	571657	453368
No. of unique reflections	59024	46669
Completeness (%)	99.84 (99.59) ^a	100 (100)
Redundancy	9.7 (9.7)	9.7 (10.5)
$\langle I/\sigma(I) \rangle$	15.7 (2.96)	9.1 (2.09)
R_{merge}	0.049 (1.09)	0.148 (1.133)
Overall <i>B</i> factor from Wilson plot (Å ²)	52.2	61.0
Refinement statistics		
No. of reflections, working set	58931	46657
No. of reflections, test set	2885	2365
Final $R_{\text{cryst}}/R_{\text{free}}$	0.195/0.238	0.203/0.231
No. of non-H atoms protein/ligand/solvent	5296/16/102	5335/96/86
R.m.s. deviations bonds (Å)/angles (°)	0.008/1.00	0.009/1.07
Average <i>B</i> factors (Å ²) protein/ligand/solvent	65/74/55	63/76/57
Ramachandran plot (%) most favored/additional/outliers	95.9/4.0/0.1	96.1/3.8/0.1
PDB accession code	6C85	6C8W

3.5.2 Result and Discussion

3.5.2.1 Overall structure of a fungal ASADH

The structure of ASADH from *B. dermatitidis* has been determined in presence of its cofactor NADP, as well as in complex with *p*-benzoquinone, a moderate fungal enzyme inhibitor. The entire sequence (362 amino acids) was fitted into electron density, except for amino acids 1-4, 90-91 and 189-190 that lacked interpretable density. Each ASADH monomer consists of two distinct domains, an *N*-terminal coenzyme binding domain (residues 1-152 and 346-359) and a *C*-terminal catalytic and dimerization domain (residues 153-345). *Bd*ASADH displays as a crystallographic dimer (Figure 3.16) similar to the other fungal orthologs, *Af*ASADH⁵⁶ and *Ca*ASADH.²³ However, consistent with other fungal ASADHs,^{31, 41} this enzyme is functionally active as a dimer of dimers. Each asymmetric unit contains two nearly identical monomers, with an rmsd of 0.169 Å (302 Cα atoms). Superposition of the ligand-bound and cofactor-bound structures shows an rmsd of 0.27 Å (489 Cα atoms) with two unstructured loops in the ligand complex that are stabilized into short helices (residues 184-186 and 341-344) due to cofactor binding. The formation of a dimer of dimers in these fungal ASADHs stabilizes these loops in a productive conformation to assist in NADP binding.

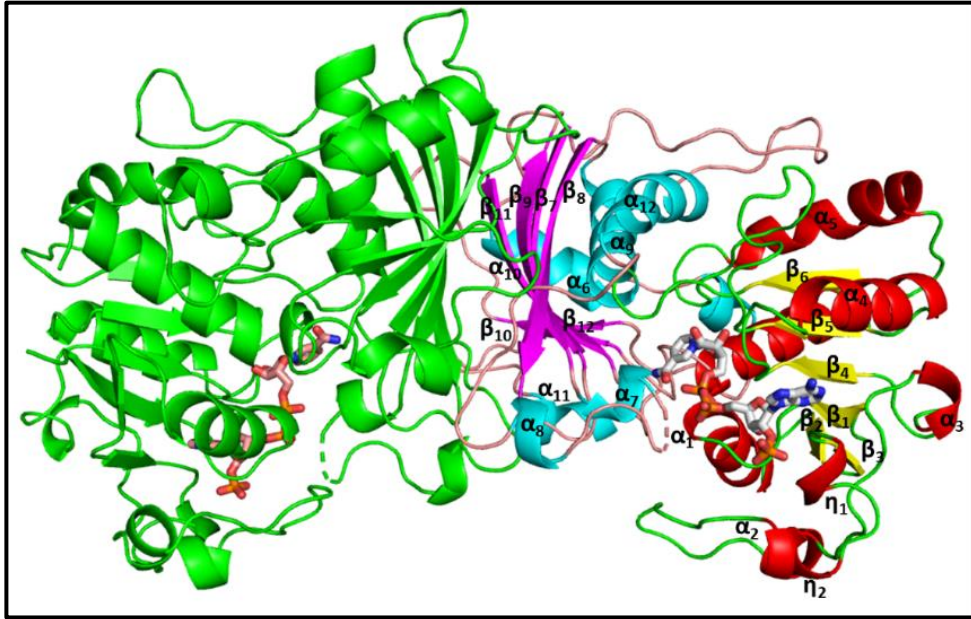


Figure 3.16. Overall structure of aspartate semialdehyde dehydrogenase from *B. dermatitidis* with NADP bound in both subunits. The secondary structure is shown in green (α -helices), magenta (β -sheets) and orange (loops), with the bound NADP (stick model) in green backbone.

3.5.2.2 Domain organization and secondary structural arrangement

The *N*-terminal domain of *Bd*ASADH begins with the β - α - β motif of the conserved Rossmann-fold (β_1 - α_1 - β_2 - β_3 , aa 7-38) that encompasses the NADPH binding site in this dehydrogenase family (Figure 3.16). This motif is connected *via* a long surface loop (aa 39-80) to a second β - α - β motif (β_4 - α_4 - β_5) region (aa 81-108) which is also highly conserved. The third motif is less conserved and is replaced in *Bd*ASADH by a long α -helix (α_5) and a short β -strand (β_6), connected by a long conserved helix (α_6 , aa157-170), followed by the first β -strand (β_7) of the dimerization domain. The helical subdomain, consisting of a helix-turn-helix found in many bacterial ASADHs,²⁷ is absent in *Bd*ASADH

and is replaced by two residues (aa 189-190) with no significant electron density, supporting the flexibility of this loop and is consistent with other fungal ASADH structures. The only exception is a modelled loop in *Tr*ASADH.³¹

3.5.2.3 Comparison with related structures

*Bd*ASADH belongs to the Rossmann-fold superfamily of pyridine-linked dehydrogenases, and shares similar overall structural features to the other structurally characterized fungal ASADHs. A search using the DALI⁸⁰ server identified four prior structures of ASADHs from pathogenic fungal species; i.e., *Cryptococcus neoformans* (*Cn*ASADH),⁴¹ *Candida albicans* (*Ca*ASADH),²³ *Trichophyton rubrum* (*Tr*ASADH)³¹ and *Aspergillus fumigatus* (*Af*ASADH).⁵⁶ Two of these fungal enzyme forms, *Ca*ASADH and *Tr*ASADH, have the cofactor NADP bound.

Here we report the first ligand-bound structure of a fungal ASADH, as well as a structure with complete electron density for the cofactor NADP. Superposition of the *Bd*ASADH dimer with those of other fungal ASADHs shows only slight differences in the orientation and length of some α -helices and β -sheets. The rmsd between the aligned *Bd*ASADH structure and the other fungal ASADH structures is 0.64 Å for *Af*ASADH (659 C α atoms), 1.48 Å for *Ca*ASADH (623 C α atoms), 1.63 Å for *Cn*ASADH (648 C α atoms). However, this difference is only 0.41 Å (586 C α atoms) for the alignment for more closely related structure from *Tr*ASADH.

3.5.2.4 Active site comparison

The sequence similarity among the ASADHs range from 90% to 10%, but the active sites are all highly conserved, with an identical set of functionally involved amino acids. Superposition of *Bd*ASADH with other fungal ASADH structures shows that these

catalytic groups are located in the same position with only minor changes in intra-residue distances. The sulphur atom of the active site cysteine nucleophile (Cys154) is in a dual conformation similar to that in *Ca*ASADH,⁹ but is located in the middle of a flexible loop similar to *Tr*ASADH rather than at the end of conserved helix as in *Af*ASADH and *Cn*ASADH. These changes in secondary structure allow some differences in the positioning of this nucleophile relative to the substrate binding groups, in some cases requiring greater conformational changes upon substrate binding to set up the active site for catalysis. As a consequence *Ca*ASADH, the fungal ASADH that requires the largest movements, also has the lowest k_{cat} among these enzymes.

3.5.2.5 Cofactor binding and conformational changes

The co-crystallization of NADP with *Bd*ASADH results in continuous electron density for the entire NADP molecule in both subunits, unlike other fungal ASADH structures in which no electron density was observed for the nicotinamide ring. The cofactor binding pocket (Figure 3.17) includes residues from three conserved loops (Ser40-Ser43, Gly86-Ala91, and Thr14-Val18). Cofactor binding causes conformational changes as these loops close around the bound NADP. The position of this mobile nicotinamide ring is constrained in this structure through hydrogen bonds from Gly186 and Asn340, as well as by hydrophobic interactions with Pro89, Asn109, Ala110, and Ala345 (Figure 3.17). The effect of these loop movements on the overall structure was investigated by analyzing the protein interface *via* PDBePISA⁷² server. The buried surface area increases from 11520 Å² in the apo-enzyme to 16360 Å² in NADP bound structure, consistent with NADP binding stabilizing the dimers of dimers observed in fungal ASADHs. The

orientation of the nicotinamide moiety near the active site cysteine also places it in an optimal position for hydride transfer from NADPH to the enzyme-bound intermediate during the catalytic cycle.⁸¹

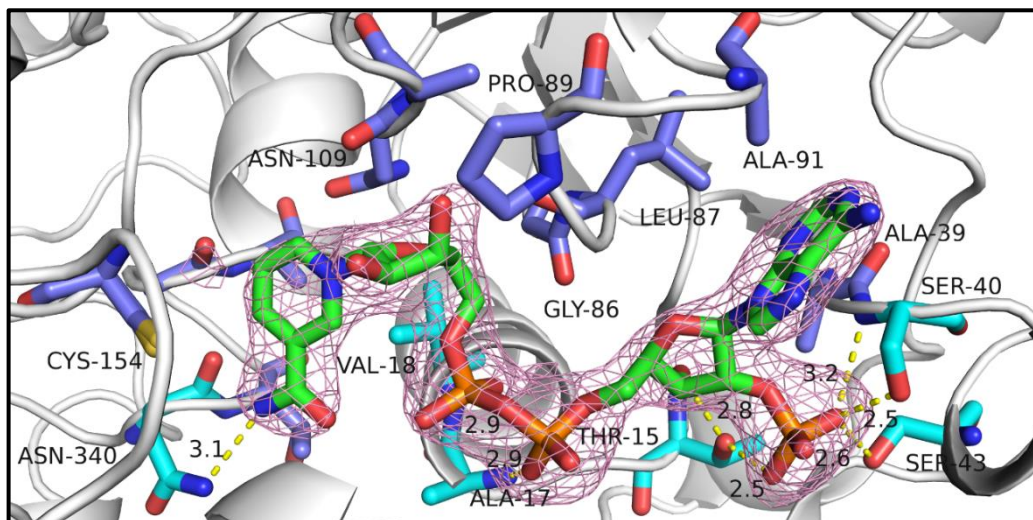


Figure 3.17: Electron density (pink mesh) of NADP bound to *BdASADH* in the cofactor binding site, showing the secondary structural arrangement in white and the hydrogen bonding (yellow dashed lines) and hydrophobic interactions (blue backbone) made by NADP in subunit A.

3.4.2.6 Binding of an active site inhibitor

Crystals of *BdASADH* were soaked with an inhibitor, *p*-benzoquinone, to form a binary complex, with additional electron density in the active site of each subunit corresponding to the shape of this inhibitor. This compound is a relatively weak inhibitor of *BdASADH* ($K_i = 126 \pm 14 \mu\text{M}$), but its competitive mode of inhibition is consistent with its observed binding in the active site. The carbonyl oxygens of the inhibitor each participate in hydrogen bonds, one with the ϵ -nitrogen of Lys211 and the guanidine nitrogen of Arg114 (substrate binding residues), and the other with the thiol of the Cys154 nucleophile (Figure 3.18). There are also hydrophobic interactions with Asn153. While the position of these

carbonyl groups are fixed, the aromatic ring adopts a different orientation in subunit A (Figure 3.18A) and in subunit B (Figure 3.18B).

No density corresponding to *p*-benzoquinone was observed when crystals of the NADP complex were soaked with inhibitor. The nicotinamide ring of NADP occupies a large segment of the active site region, and cofactor binding shared a common binding interaction (Gly186) that likely blocks the binding of this aromatic inhibitor. The binary complex with *p*-benzoquinone is the first structure of an inhibitor bound to the active site of a fungal ASADH. Using this initial information we are conducting *in silico* docking studies, SAR analysis, and structure-guided synthesis to improve the potency and selectivity of these fungal ASADH inhibitors.

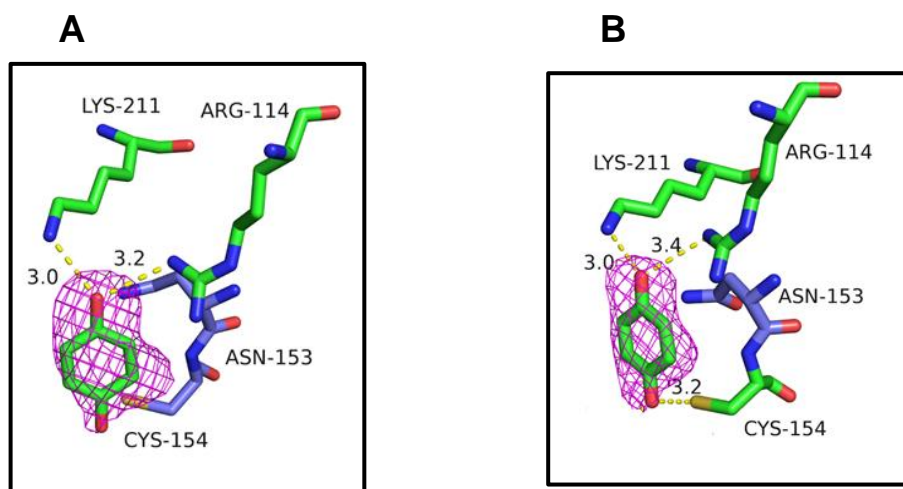


Figure 3.18: Representative electron density and modelling of amino acid side chains of *p*-benzoquinone bound near the active site of *BdASADH*. Hydrogen bonding (yellow dashed lines) and hydrophobic interactions made by *p*-benzoquinone bound to *BdASADH*. Hydrogen bonding residues are shown in green backbone and hydrophobic residues are shown in blue backbone. (A) Inhibitor binding in subunit A. (B) Inhibitor binding in subunit B.

3.5.3 Conclusions

The first inhibitor-bound and cofactor-bound structures of ASADH from the pathogenic fungi *B. dermatitidis* have been determined, along with a structural and functional comparison to other ASADH family members. The structure of *BdASADH* is similar to the other fungal orthologs, but with some critical differences in the orientation of some active site functional groups and in the subunit interface region. The presence of a bound ligand revealed new details about inhibitor binding, and the flexible orientation of the aromatic ring provides helpful insights into the design of more potent and selective antifungal compounds.

3.6 Crystallization of *TgASADH*

Initial screening for crystallization of the *TgASADH* apo-enzyme was carried out with commercially available sparse matrix screening kits (Jena Bioscience Basic screening) with a total of 96 conditions. The screening trays were set-up by mixing equal volumes (1 μ L) of the protein (4.5 mg/mL) with the reservoir solution, with a total of 50 μ L well solution in a 96-well sitting drop tray and incubated at 293 K. Initial crystallization attempts using JB screening kits showed that most of the drops remained clear after 72 h. A few drops showed mild precipitate, with a few drops as floccules in the center of the drop. This suggests that either the protein concentration needs to be increased, or screening with other kits with different types and concentration of precipitants should be used. Initial screening with MBP and GST fusion constructs of *TgASADH* (12 mg/ml) with JB Basic screening kit gave a few hits with crystals of different morphology. From these initial hits, optimization of precipitants, buffer, pH, temperature, and additives is currently under way to achieve diffraction quality crystals.

3.7 Crystallization of *Ca*HDH

Since no apo-enzyme crystal structure has been solved for any of the fungal HDHs, initial attempts were targeted on solving an apo-enzyme crystal structure, which will give a snapshot of the enzyme before catalysis. Crystallization trials for *Ca*HDH have been performed using Hampton Index screening at a protein concentration of 10 mg/ml. The hanging drop method was used in 48 well Hampton trays with protein and precipitant in a 1:1 ratio. Initial crystallization trials yielded about 60% of precipitated drops and 40% clear drops after a week. Among the crystal drops, many of them precipitate after two to three weeks and some of the drops showed little crystalline precipitate but none of them yielded crystal-like growth for further optimization. A typical clear drop from condition 0.2M Ammonium acetate, 0.1M HEPES pH 7.5, 25 % w/v PEG 3,350, (Figure 3.19, left) and precipitated drop from condition 0.1M bis-tris pH 6.5, 0.5M Magnesium formate dihydrate (Figure 3.19, right) obtained is shown in Figure 3.19 after Index screening.

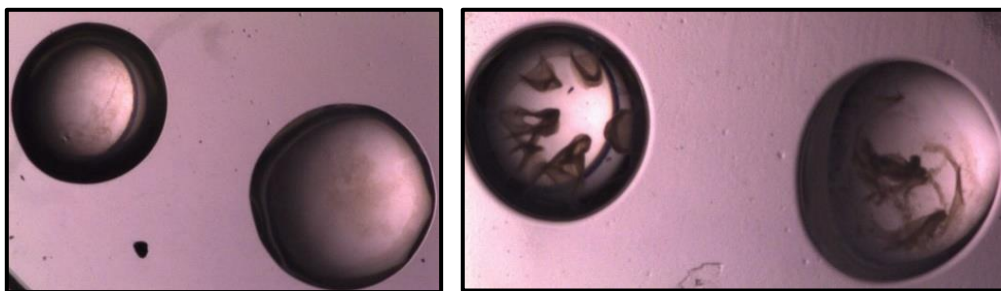


Figure 3.19: Crystallization of *Ca*HDH at 10 mg/ml using Hampton index screening

3.8 Neutron crystallography

We have solved high resolution X-ray crystal structures of ASADH from different pathogenic fungi and bacteria, both in apo- and ligand-bound forms^{23, 31, 41, 56}. The kinetic mechanism of ASADH has been proposed to proceed through formation of a covalent acyl enzyme intermediate and hydride transfer from NADP to the thioester intermediate to form the product. However, the detailed mode of hydride transfer from NADPH to thioacyl

enzyme intermediate to form the tetrahedral enzyme intermediate, the position of hydrogens in the tetrahedral intermediate, and the protonation state of the imidazole nitrogen of the active site histidine of ASADH have not yet been determined. Solving neutron structures will elucidate the detailed mechanism of proton transfer and the position of hydrogens throughout the catalytic cycle in ASADH, which will assist in the design of mechanism-based inhibitors. The crystals of *Af*ASADH diffracted to 2.3 Å in P3₁21 space group with the longest unit cell being 202 Å. The crystals of *Sp*ASADH diffracted to 1.6 Å in X-ray and belonged to the P21 space group with longest unit cell of 98 Å. We are scheduled to use beamtime at Oak Ridge National Lab to screen our *Af*ASADH and *Sp*ASADH crystals for initial neutron diffraction studies. The crystals were grown in a nine-well sitting drop sandwich box setup (Figure 3.19, left). The crystal volume was setup with 400 µl each of protein and precipitant, with the protein concentration at 50 mg/ml. The tray was incubated at 293K and 277 K to slow the nucleation and growth. The crystals (4.5 x 1.9 x 0.2 mm³ in size) (Figure 3.19, right) were mounted in a quartz capillary with both ends sealed with clay. Depending upon the nature of initial diffraction, additional crystals co-crystallized with the native substrate will be subjected to neutron diffraction.

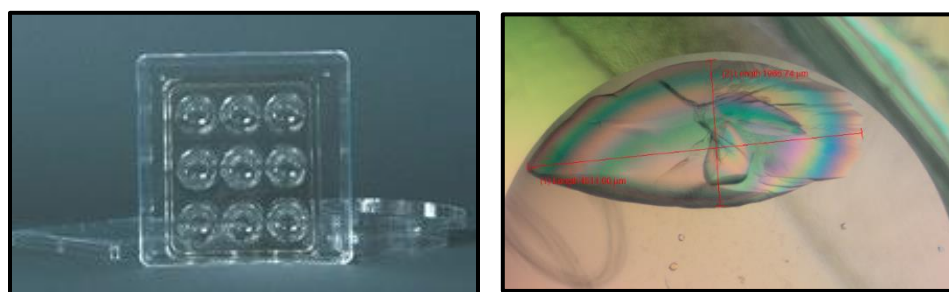


Figure 3.20: A) a typical sandwich box crystal tray B) *Af*ASADH crystals C) A single large crystal of *Af*ASADH obtained from the condition 2 M ammonium sulphate and 0.1 M bis-tris, pH 6.5.

Chapter 4

Computational studies of different ASADHs

4.1 Docking studies

(Text and figures have been adapted from Dahal et. al., SLAS Discovery., 2018)

Shape-based virtual screening⁸², molecular docking⁸³, molecular modelling⁸⁴ and pharmacoinformatics⁸⁵ analysis have each been carried out in an attempt to identify bacterial ASADH inhibitors. *In silico* studies with phytochemicals⁸⁶ against fungal aspartate pathway enzymes has been recently carried out, but not much information is available regarding pathogenic fungal ASADHs. Autodock⁸⁷, Auto Dock Vina⁸⁸ and Coot⁷⁰ are excellent tools to model the binding of new ligands to an enzyme target. The purpose of the docking experiments is to find the global minimum in the interaction energy between a ligand and the receptor, exploring all available degrees of freedom for the system⁸⁹. Autodock uses a grid-based energy evaluation and several different methods to search the torsional freedom, and uses a scoring function to predict the binding affinity⁹⁰. Each evaluation includes Van der Waals bonding, hydrogen bonding, electrostatic interaction and desolvation energy⁸⁹. Autodock Vina (Vina for short) is a newly developed docking software with improved speed and accuracy of docking, with a new scoring function, efficient optimization and multithreading⁸⁸. Each docked conformation will

enable us to predict the possible electrostatic and Van der Waal's type interactions which are critical in selecting drug molecules.

4.1.1 Ligand preparation for docking studies

All of the inhibitors were prepared with *Ligprep* software, which generates low energy tautomers and enumerates realistic protonation states at physiological pH. Each ligand was optimized for equilibrium geometry in vacuum using the HF/6-31+G* level basis set. Proper charges were assigned when necessary before optimization. Calculations were carried out using *Spartan'14* (*Spartan'14* Wavefunction, Inc. Irvine, CA). The minimized ligands were prepared for docking using the ADT tools by adding polar hydrogen atoms, merging non-polar hydrogen atoms, adding atom-type parameters, and defining rotatable bonds.

4.1.2 Protein structure preparation for docking studies

Four structures of different fungal ASADHs are currently available in the Protein Data Bank (PDB) ⁷⁶. The *CaASADH* structure has the best resolution (PDB id: 3hsk, 2.2 Å), and molecular docking studies were performed with the best inhibitors into the active site of *CaASADH* using *AutoDock Vina*.⁸⁸ Water molecules were removed and coordinates of NADP were transferred into the enzyme structure in its binding site. The grid box was set to 30*28*30 Å with grid spacing of 1.00 Å. The box was centered in the active site region, ensuring coverage of the residues involved in substrate and cofactor binding. *AutoDock Vina* was performed at exhaustiveness level 16 with the number of binding modes set to 20. The top 20 docking poses were generated, with the lowest energy pose of each docked ligand used to analyze the interactions of the ligand at the active site of the enzyme. The Python scripts in MGL tools package were used to analyze the docking

results, and images were generated using *Pymol*.⁷¹ An example of Autodock vina configuration file for the ligand 2,3-dichloro-1,4-naphthoquinone is shown in Appendix A1.

4.2 High-throughput docking

AutoDock Vina runs much faster⁹¹ and is capable of docking larger ligands more accurately than the previous software versions. For virtual high throughput screening (VHTS) the ZINC library⁹² was selected because it contains a large collection of drug-like molecules in pdbqt format and also because it allows the purchase of library compounds. A subset of about 70,000 compounds were screened, selected from the “Full_nci_ALLTAUTOMERS” and “NCI_DiversitySet2” (<http://zinc.docking.org/pdbqt/>) folders for virtual high throughput screening. VHTS was downloaded using VSDK⁹³ codes with slight modifications and Cygwin was downloaded from (<https://www.cygwin.com/>). VS01.bash of VSDK codes was modified to perform iterative docking for several ligands and extract binding energy into binary files. The lowest binding energy conformation in the first cluster was considered as the most favorable docking pose. This was further validated by analyzing the ligand interactions by using the program *Ligplot*.⁹⁴ An example of modified vs01.bash for virtual high throughput screening and result analysis syntax is shown in appendix A2 and A3.

4.3 Inhibitor docking and binding affinities

To explore the binding mode of the more potent inhibitors of *CaASADH*, and to provide guidance for additional inhibitor optimization, a comprehensive molecular docking study was performed to identify the most plausible and accurate pose of these ligands bound at the active site of fungal ASADHs⁹⁵. The binding orientation of the most potent quinone derivative, 2-chloro-3-methoxynaphthoquinone (Figure 4.1, top) and that of a

moderately potent derivative, 2-chloro-3-phenoxy-naphthoquinone (Figure 4.1, bottom), were compared to identify any significant changes that could explain these affinity differences. For the most potent inhibitor the carbonyl oxygen at position-4 of the naphthoquinone ring is predicted to make hydrogen bonds with Asn107 and Arg112 (a group involved in substrate binding), and the oxygen atom of the 3-methoxy group is hydrogen bonded with Lys211 (another substrate binding residue) (Figure 4.1). In addition to these key interactions, this inhibitor also makes hydrophobic interactions with several residues in the active site, including the cysteine nucleophile and additional residues (Asn155 and Glu211) that are involved in substrate binding. There is also a cation- π interaction between Arg18 and the aromatic naphthoquinone ring, with these multiple interactions contributing to the high affinity of this inhibitor towards *CaASADH*.

Some additional naphthoquinone derivatives, with various hydrophobic and hydrophilic functional group substitutions at positions 2 and 3, were also found to be inhibitors against *CaASADH*. The 45-fold decrease in potency when the 3-methoxy group in 2-chloro-3-methoxynaphthoquinone is replaced by a 3-phenoxy group is most likely due to loss of an important hydrogen bond between the oxygen atom of the phenoxy derivative and the amine nitrogen of Lys214, and the failure of any additional interactions with the phenyl ring to overcome this loss. This decreased potency is observed despite docking results that predict the retention of the hydrogen bonding network to the carbonyl oxygen at C-4 (Figure 4.1B). Replacing the 2-chloro group in 2,3-dichloro-1,4-naphthoquinone with a hydroxyl, ethylamino, or dimethylamino group at this position leads to a complete loss of potency. Docking studies suggest that the oxygen or nitrogen heteroatom in these functional groups are no longer able to make this productive hydrogen bond with Lys214,

and a resulting shift in the orientation of the naphthoquinone ring disrupts the hydrogen bonding network to the C-4 carbonyl oxygen.

While there is not an exact correlation between the calculated binding energies and the experimental K_i values for a range of *Ca*ASADH inhibitors from different structural classes, and there are a few outliers, a general trend is observed in which the most potent inhibitors (average K_i of 28 μM for nine compounds) are predicted to have stronger binding affinities, while the weakest inhibitors examined (average K_i of 250 μM for seven compounds) have the lowest predicted binding affinities (Table 4.1). Given the differences in conditions (solution measurements *vs.* gas phase calculations) and in enzyme forms (enzyme-substrate complex *vs.* enzyme-NADP complex docking) the lack of a perfect correlation between calculated and measured values is not unexpected. However, in the absence of available enzyme-inhibitor structures, these docking results can be used to guide improvements in inhibitor potency by *in silico* manipulations of both the position and the identity of different functional groups around these core structures.

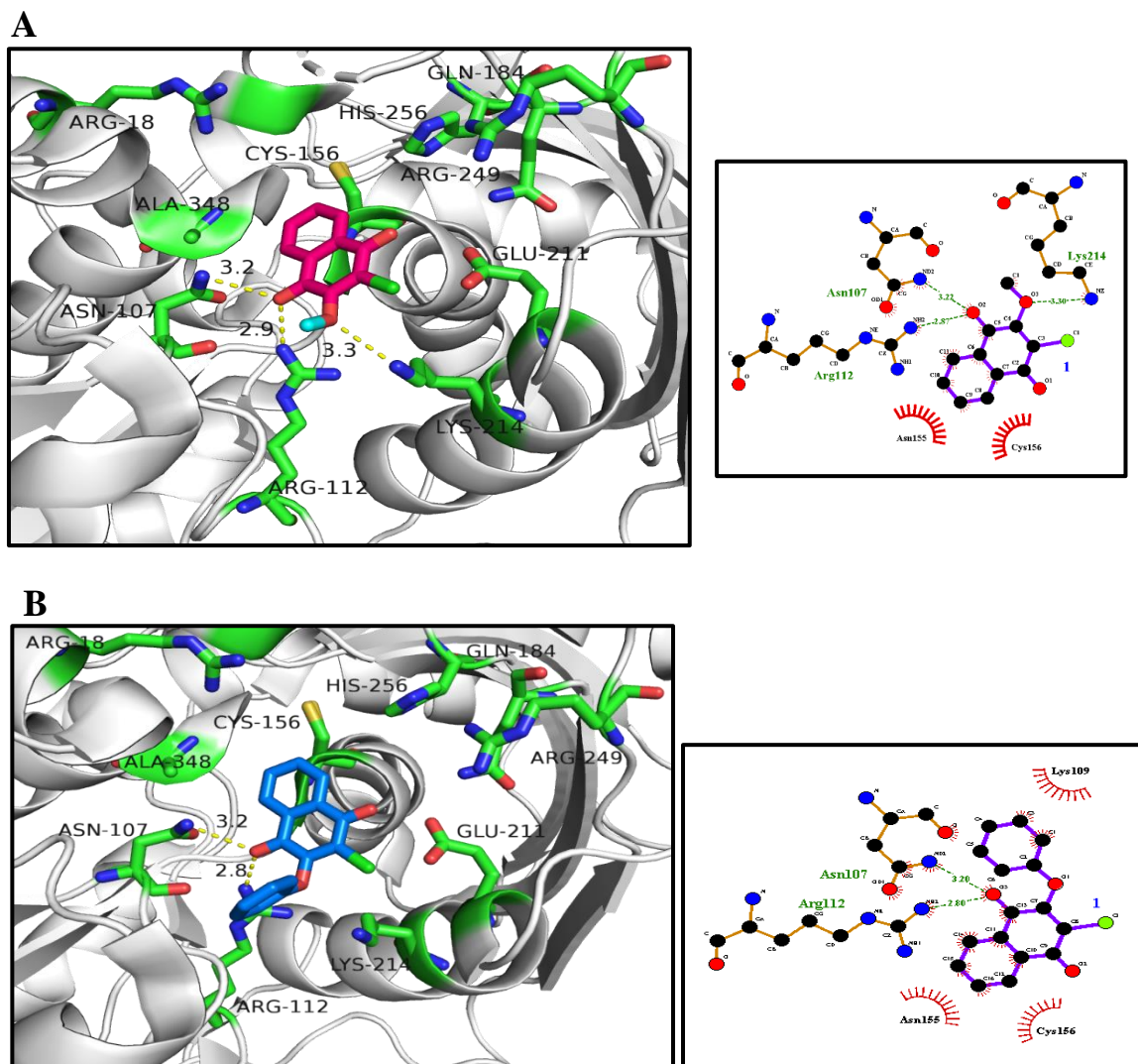


Figure 4.1. Predicted binding mode of 1,4-naphthoquinone derivatives binding in the active site of *CaASADH*. Residues in the active site of *CaASADH* are shown as sticks, hydrogen bonds are indicated by dashed lines with bond distances, active site residues involved in hydrogen bonding interactions are labeled, and each type of interaction is also shown on the *ligplot* diagram (right). These docked structures suggest an essential binding role for the carbonyl oxygen moiety. (A) binding pose of the more potent 2-chloro-3-methoxy-1,4-naphthoquinone. (B) binding pose of the less potent 2-chloro-3-phenoxy-1,4-naphthoquinone.

Table 4.1. Predicted affinities and measured inhibition constants of *Ca*ASADH inhibitors

fungus ASADH inhibitors	Predicted affinity ^a (kcal/mol)	<i>C. albicans</i> ASADH K _i (μM)
2-chloro-3-phenoxy-1,4-naphthoquinone	-6.7	73 ± 11
2-chloro-3-acetamido-1,4-naphthoquinone	-6.7	15.4 ± 1.6
2-chloro-3-methoxy-1,4-naphthoquinone	-5.8	1.6 ± 0.2
2,3-dichloro-1,4-naphthoquinone	-5.8	6.5 ± 0.3
dichloro, dicyano-1,4-benzoquinone	-5.8	58 ± 7
naphthalene-2,3-dialdehyde	-5.7	45 ± 8
tetrahydroxy- <i>p</i> -benzoquinone	-5.5	45 ± 7
2-chloro-1,4-naphthoquinone	-5.5	4.1 ± 0.7
2-bromo-1,4-naphthoquinone	-5.4	6.1 ± 1.1
1,4-naphthoquinone	-5.1	62 ± 4
tetrachloro-1,4-benzoquinone	-4.7	66 ± 10
L-thiazolidin-2-one-4-carboxylic acid	-4.5	225 ± 24
catechol	-4.4	121 ± 17
3,4,5-trichloropyridazine	-4.4	453 ± 81
benzene-1,3,5-triol	-4.3	440 ± 110
<i>p</i> -benzoquinone	-4.2	73 ± 11
<i>cis</i> -1,2-diaminocyclohexane	-3.9	287 ± 26
cyclohexyl iodide	-3.7	154 ± 28

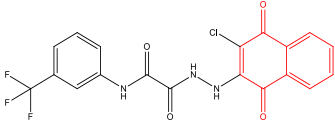
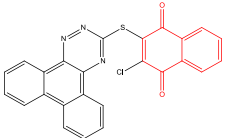
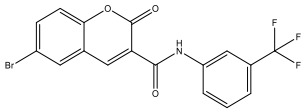
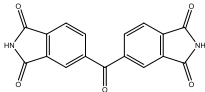
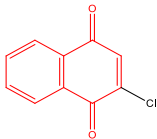
^aCompounds with predicted affinities of -5.4 kcal/mol or greater (upper group) were classified as stronger inhibitors, while those with affinities of -4.5 kcal/mol or less (lower group) were classified as weaker inhibitors.

4.4 Zinc library virtual screening

To expand the coverage of chemical space diversity *AutoDock Vina* was used to screen about 70,000 commercially available ZINC library⁹² selected for virtual screening, to identify various chemotypes that are potent and specific to our fungal target. The result

of this screening is a ranked list of library molecules from highest to lowest predicted affinity scores. High throughput docking of this subset of selected ZINC library compounds yielded promising hits showing predicted binding energy as high as -8.9 kcal/mol. Ultimately, a set of these compounds were selected for experimental testing (K_i determination), with the compounds obtained from the NCI Developmental Therapeutics Program (DTP) repository. Because the difference in docking scores among the top ranked molecules fell in a narrow range, a final list of compounds to be tested was selected by visual inspection of their structures, using productive interactions made by these compounds at the ASADH active site, and availability for purchase as the selection criteria. Some compounds were eliminated as potential candidates due to limited solubility but, of the eight compounds tested, three were non-inhibitors and five showed K_i values ranging from about 450 μM to as low as 4 μM (Table 4.2). As seen before, there is not a strong correlation between the affinity score and the experimental K_i values. Three of these potent hits contain a naphthoquinone sub-structure (highlighted in red), one is a phthaldehyde-related analog (00056857) and one has a heterocyclic ring (00934413), consistent with the structures identified from previous fragment library hits. The identification of compounds from the ZINC library with similar structural moieties to those of already identified inhibitors demonstrates that high-throughput docking can be a powerful tool for computer-aided drug design, especially for the generation of initial hits for targets when there are no preliminary *in vitro* screening results or with no known enzyme-inhibitor structures.

Table 4.2 Compounds showing high affinity scores with K_i values against *Ca*ASADH.

ZINC Compound ID ^a	Structure	Predicted affinity (kcal/mol)	<i>C. albicans</i> ASADH K_i (μ M)
01574202		-8.9	14.3 ± 0.63
01573832		-8.8	242 ± 34
00934413		-8.7	448 ± 48
00056857		-8.5	301 ± 44
00901831		-5.6	4.1 ± 0.7

^a These compounds were selected based on their affinity scores and measured K_i values, with the naphthoquinone sub-structure highlighted in red.

The compound ZINC01574202 was further docked into the active site of *Ca*ASADH and this inhibitor was predicted to make a number of interactions with the residues at the active site. Each functional group in the inhibitor is interacting with catalytic residues, such as Arg112, Lys214, Glu211 and His256 (Figure 4.2a) through hydrogen bonding interactions. The inhibitor also has a number of interactions with other residues at the active site, such as Arg249, Asn107, Gln184, Asn155, Ala87, and Lys109, which corroborates its high predicted binding affinity. The inhibitor also shows drug-like properties consistent with most of the criteria of Lipinski's rules⁹⁶.

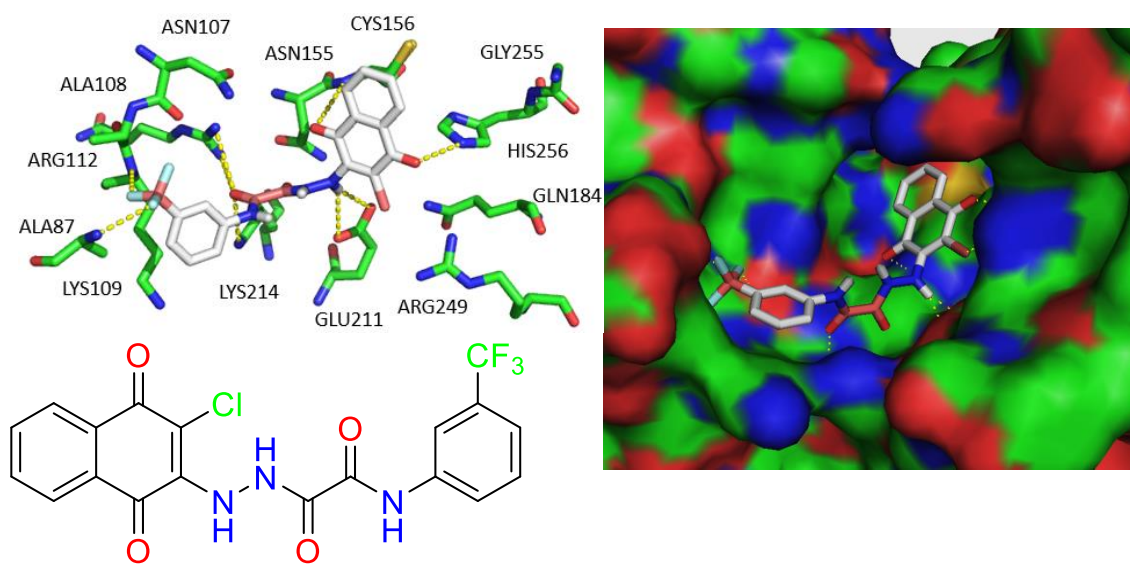


Figure 4.2: a) best binding pose and H-bonding interactions of ZINC01574202 in the active site of *CaASADH*, with yellow dotted line showing the H-bonding interactions, b) surface view of active site pocket interacting with ZINC01574202 c) structure of ZINC01574202

4.5 Molecular dynamics

In order to study the stability of the ligand bound at the enzyme active site, Molecular Dynamics (MD) simulation was performed using the *SpASADH* crystal structure (PDB code:4r3n) for setting the initial benchmark. Molecular dynamics simulation was performed for 4 ns using the software NAMD and the system was prepared using the program VMD. The 3D structure was embedded in a cubical solvent box containing TIP3 water molecules. The water molecules were placed 5 Å around the protein molecule and the C-terminal and N-terminal end was capped. In order to mimic the physiological environment equivalent sodium ions were added to the system for neutralization. The cut-off for van der Waals interaction was set to be 12 Å, switching

distance for smoothing was 10 Å and non-bonded pairlist distance was 14 Å. The NPT ensemble was maintained with a Langevin thermostat and isotropic Langevin Piston. Each system was minimized for 10,000 steps using conjugate gradient and the line search algorithm. This was followed by 4000 ps equilibration at 300 K. A time step of 2 fs was employed in the Verlet algorithm. Production runs of 4 ns were completed with an average temperature of 300 K. The SHAKE algorithm was used to constrain hydrogen bond length. MD simulations were performed on a 6 core Linux machine taking ~72 h CPU time for each 4 ns simulation. The simulations were performed using NAMD v2.11 using CHARM 22 force field with CMAP correction. A detailed description of the configuration file for minimization and equilibrium can be found in appendix B.

4.5.1 Results and Discussion

The plot of RMSD over the backbone C α over the time frame used for analysis shows that the system minimized for first 10,000 steps and showed an initial increase in RMSD and then plateau after around 50 frames and then stabilized until 400 frames. The system then started equilibrating for 2,000,000 steps and there is slight variation in the RMSD values until the completion of 4 ns dynamics profile (Figure 4.3). The results showed that the system has not completely equilibrated over the 4 ns time frame. The experiment need to be performed for longer time frame in order to equilibrate the system so that MD simulations can be performed with ligand bound structures in order to evaluate the stability of the ligand.

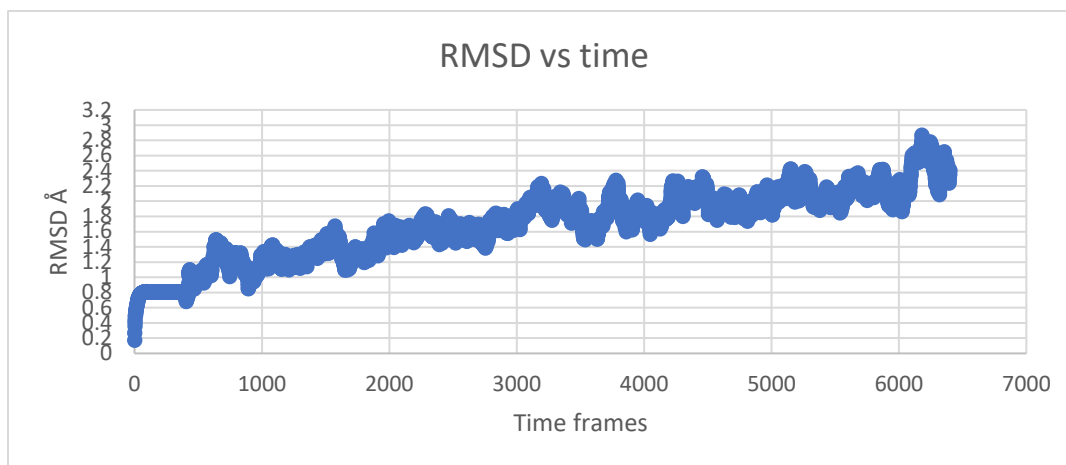


Figure 4.3: RMSD variation versus the simulation time after 4 ns MD simulation

4.6 Dynamic light scattering (DLS)

DLS experiment were performed on Anton Paar DLS instrument at various protein concentration (1 mg/ml, 4 mg/ml and 8 mg/ml). *AfASADH* protein sample was subjected to dynamic light scattering, and the scattering profile was monitored to obtain the particle size distribution and polydispersity. Samples were performed in replicates at 293 K and the correlation function was plotted against the standard curve with our sample curve. A detailed description of DLS parameters can be found in appendix A2.

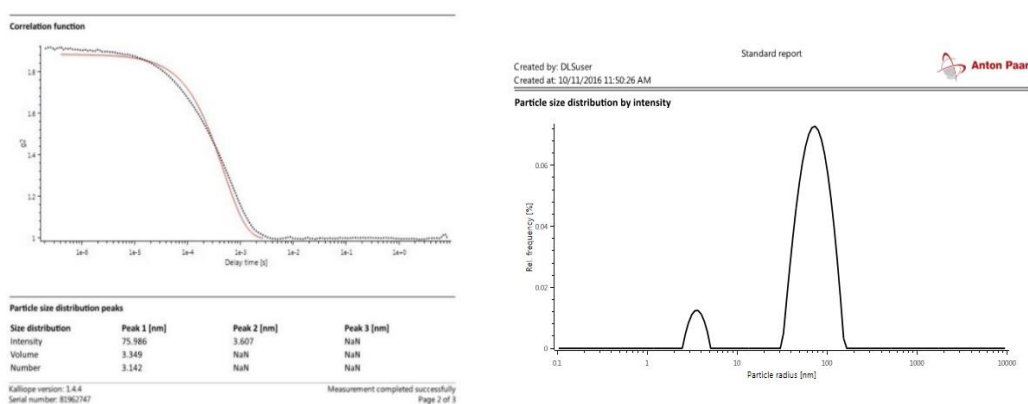


Figure 4.4: DLS analysis of *AfASADH* sample a) correlation function analysis with particle size radius b) major peak distribution profile with particle radius of *AfASADH* sample.

The DLS studies shows that *Af*ASADH sample has about 20% polydispersity with two intense peaks (Figure 4.4) for particle size distribution. The lower polydispersity value suggested that the protein sample in the current buffer has less aggregation and therefore has a higher probability of producing initial crystal hits. The correlation function plot matches well with the theoretical correlation function curve (Figure 4.4, left), and the particle size of the most intense peak was found to be 3.67 nm which is similar to what was observed from SAXS analysis (Radius of gyration values around 35 Å) (Table 4.3). Although DLS is not able to determine the exact molecular weight, the improved polydispersity and the approximate particle size supports the stability and purity of the protein sample for subsequent studies.

4.7 Small angle x-ray scattering (SAXS)

In order to identify the shape, size and molecular weight of our protein of interest, we performed the SAXS experiment of different fungal ASADHs. SAXS sample were analyzed at Oak Ridge National Lab with RIGAKU FR-E X-ray source. The SAXS analysis was carried out at three different protein concentrations (1 mg/ml, 4 mg/ml and 8 mg/ml) with subtraction of accurate buffer blank as well. Guinier plot, pair distance distribution function, and several other parameters are calculated using Biosis software suite.

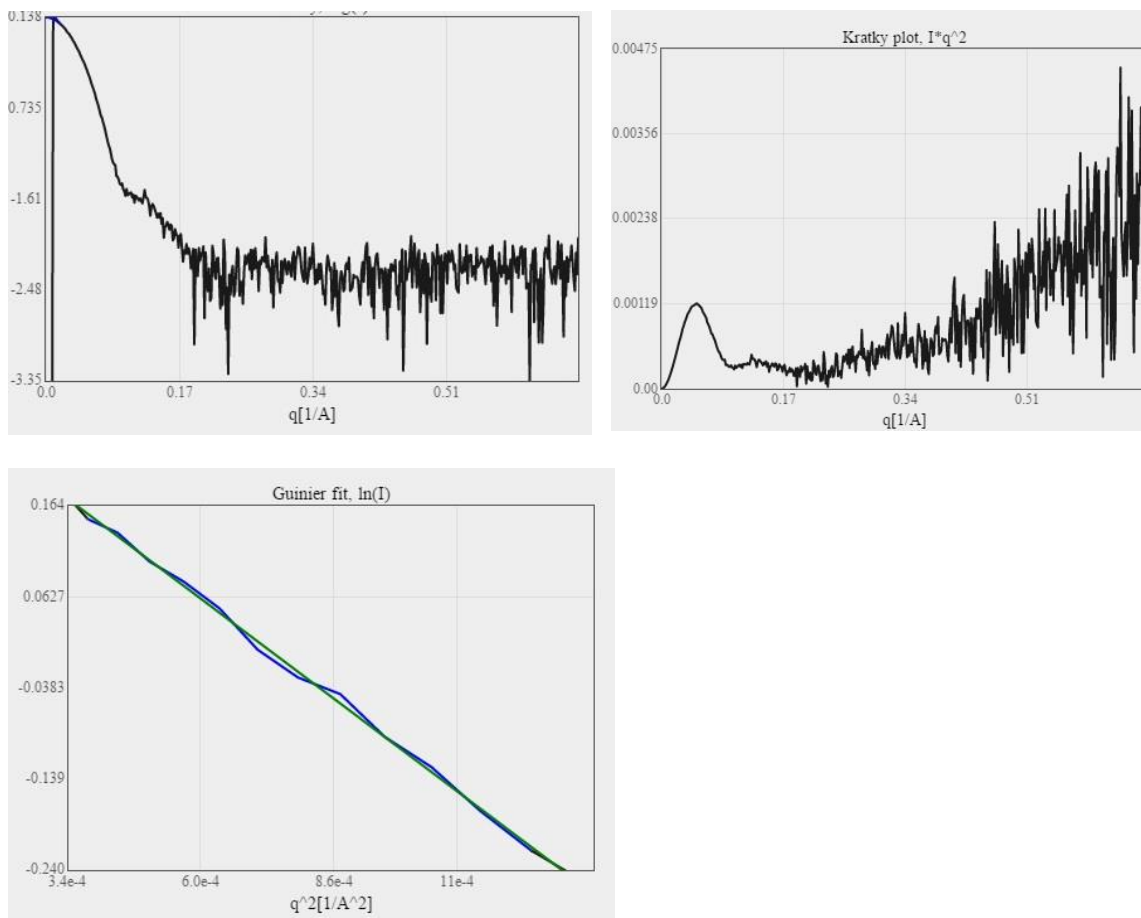


Figure 4.5: a) log Iq vs q profile of AfASADH b) Kratky plot of AfASADH sample c) guinier plot analysis at low q region

From SAXS studies of ASADH sample, it was found that all ASADH were soluble globular protein with minimal aggregation (Figure 4.6) while both mouse and human ANAT samples were found to have significant aggregation from the log Iq vs q profile and the Kratky plot. The guinier plot analysis yielded the experimental Rg values (Figure 4.5) in the range of 35 Å for AfASADH and CnASADH sample while the Rg values obtained from X-ray crystal structure from dimer and tetramer model yielded Rg values around 31 Å and 35 Å respectively (Table 4.3). This also supports our previous conclusion of fungal ASADH existing as a tetramer in solution.

Table 4.3 Radius of gyration distribution of different ASADHs sample with theoretical and experimental Rg parameters

ASADHs	Theoretical Rg (Å)		Experimental Rg (Å)
	Dimer Model	Tetramer Model	
<i>C. neoformans</i>	31.02	35.70	35.96
<i>T. rubrum</i>	31.29	35.84	38.78
<i>A. fumigatus</i>	30.50	N/A	35.95
<i>C. albicans</i>	30.66	N/A	36.42

4.8 Conclusions

Docking and molecular dynamics has widely been used in structure-based drug design community and has potential to predict the binding affinity and SAR properties of a ligand to its receptor however both of these tools rely heavily on molecular mechanics (MM) not on the quantum mechanics (QM) so the predicted binding energies or binding poses will not be accurate. We aim to perform QM/MM study for the most potent inhibitors with the active site treated with QM methods while the rest of the molecule will be performed by MM studies. Some of the ASADH inhibitors (phthaldehyde) has shown noncompetitive mode of inhibition by disrupting the dimers of dimers of fungal ASADHs into inactive dimers and SAXS studies will be performed with the protein sample incubated with the protein-protein interaction (PPI) inhibitors and their effect in change of oligomeric state will be validated.

Chapter 5

Cell based screening of ASADH inhibitors against *Candida albicans*

5.1 Introduction

Candida albicans is a common, opportunistic human fungal pathogen that can cause both mucosal and deep tissue infections¹⁵ and is the most frequently isolated fungus from clinical settings⁹⁷. This dimorphic fungus, being the predominant causative agent of human candidiasis⁹⁸, inhabits the human body as a commensal organism and can cause wide range of infections ranging from oral thrush and vaginitis to potentially life threatening infections; especially in immunocompromised patients, such as organ transplant recipients, patients receiving cancer chemotherapy, and HIV/AIDS patients⁹⁷. Despite the addition of new classes of antifungals to combat these pathogenic fungal infections, our current armamentarium of antifungal agents is limited compared to vast array of antibacterial agents. This may be due to fungi, being eukaryotic, possess similar metabolic targets compared to mammalian host, making it difficult to develop a specific antifungal aimed only at the specific targets of the pathogen. This poses a serious challenge in developing new treatment therapies against these fungal infections. Also, the majority of available antifungal drugs are fungistatic rather than fungicidal, and possess relatively

high toxicity⁹⁹. Concurrently, antifungal drug resistance is increasing significantly in recent years, even against newly developed antifungals, with biofilm formation increasing responsible for antifungal drug resistance. Biofilms are organized, highly-structured surface-associated cell aggregates with an upper layer made up of hyphal cells that are enclosed within a protective extracellular matrix¹⁵⁻¹⁶. These biofilms are responsible for rendering the fungus significantly more resistant to drugs, and it is estimated that about 65% of all human infections are related to biofilm formation. Also, the developing antifungal drug resistance is now paralleling that of antibacterial resistance, and previously benign fungi are now the cause of systemic fungal infections. This suggests that there is an urgent need to develop novel antifungal agents that are more effective and less toxic than those currently available. The *Candida* genus, by itself, includes about 20 different *Candida* species that are known to be etiological agents of human infections¹⁵. These different species of *Candida* respond to antifungal drugs to a variable degree even within the same species, and certain species can develop resistance to common prescribed antifungal agents¹⁰⁰. Due to these serious issues, there is an urgent need of an extensive research program, against new and previously untested drug targets, to develop new antifungal drug candidates.

Amino acid biosynthesis pathways have been widely used as an antifungal drug target for various fungal pathogens¹⁰¹. In Chapter 1, we discussed the screening of ASADH against diverse library compounds and described the identification of initial hits that are effective inhibitors at lower micromolar levels. We have also optimized the initial hits based on two different core structures of phthaldehyde and *p*-benzoquinone. These compounds are the first set of sub-micromolar inhibitors against fungal ASADH that have

been identified to date. The focus of this chapter is to evaluate the anti-*Candida* properties of these small molecule inhibitors against a pathogenic strain of *Candida*.

5.2 Materials and methods

5.2.1 General reagents

The following compounds; MTT, amphotericin B, menadione, and ampicillin were purchased from Sigma Aldrich (St. Louis, MO). Protein purification buffers and DMSO were obtained from Thermo Fisher Scientific (Waltham, MA). The compounds were dissolved in varying concentrations of DMSO depending upon their solubility. All other reagents were of the highest quality available and obtained from a wide variety of commercial sources.

5.2.2 Growth media

Yeast peptone dextrose broth (YPD) and YPD agar (1% w/v yeast extract, 2% w/v peptone, 2% w/v dextrose, 1.5% agar) were purchased from Difco Laboratories (Detroit, MI), and RPMI 1640, supplemented with L-glutamine, Dulbecco's Minimum Essential Medium (DMEM) supplemented with high glucose and L-glutamine, Dulbecco's Phosphate-Buffered Saline (DPBS), and Fetal Bovine Serum (FBS) were purchase from Thermo Fisher Scientific (Waltham, MA). All culture media were prepared and used as per the manufacturers' protocol and were solubilized in distilled water and sterilized by autoclaving at 121 °C, 1.0 atm. for 20 min.

5.2.3 Inoculum preparation

The *Candida* species (*Candida albicans* ATCC[®] MYA-2876, strain CAF2-1), used in this study was purchased from the American Type Culture Collection (ATCC) (Manassas, VA). The candidal stock, frozen in glycerol at -70 °C was thawed at room

temperature and then aseptically dispensed in 20 ml of Yeast Peptone Dextrose (YPD) broth and incubated overnight at 30 °C. The overnight culture was centrifuged at 3200 rpm (4 °C) for 5 min to harvest the *Candida* cells. The supernatant was discarded and the pellet was vortexed vigorously and washed twice with phosphate buffered saline (PBS) and then re-suspended in 5 ml of YPD broth. The turbidity of the suspension was adjusted and standardized spectrophotometrically to produce a 0.5 McFarland standard density giving a 1 to 5×10^6 CFU/ml suspension, and the yeast cell numbers were determined using a hemocytometer.

5.2.4 Microbial susceptibility against yeast and hyphal forms

The *Candida* strains were inoculated with YPD broth culture medium and grown overnight at 30 °C with shaking at 180 rpm for performing Minimal Inhibitory Concentration (MIC) and Minimal Fungicidal Concentration (MFC) tests. MIC was determined by broth microdilution method¹⁰². The overnight broth was diluted and counted using a hemocytometer with initial cell density of 4×10^6 cells/mL. Next, 100 µL of these *Candida* cells were incubated in the YPD medium containing two-fold serial dilutions of each ASADH inhibitor in the 96-well microtiter plates for 48 h at 30 °C. The final concentrations of all compounds ranged from 1 µg/mL to 320 µg/mL. MIC is defined as the lowest concentration of the compound that prevents the visible growth of the microorganisms. Once MIC values were determined, 10 µL aliquots were taken from the wells corresponding to MIC, 2x MIC and 4x MIC, and inoculated onto YPD agar plates supplemented with ampicillin (100 µg/ml) and additionally supplemented with 10% FBS for hyphal growth of *Candida*. The plates were incubated at 30 °C for yeast form (Figure 5.1A) and 37 °C for hyphal forms (Figure 5.1B) and fungal colonies were counted after 48

h of incubation. These *Candida* colonies were inspected under a light microscope and imaged using a EVOS FL cell imaging system (Thermo Fisher Scientific). Control wells with only YPD broth without the presence of fungal inoculum was performed to check the sterility of the YPD media used. All experiments were performed in triplicate, amphotericin B was used a positive control, DMSO was used as negative control and the final concentration of DMSO in susceptibility assays never exceeded 0.06%.

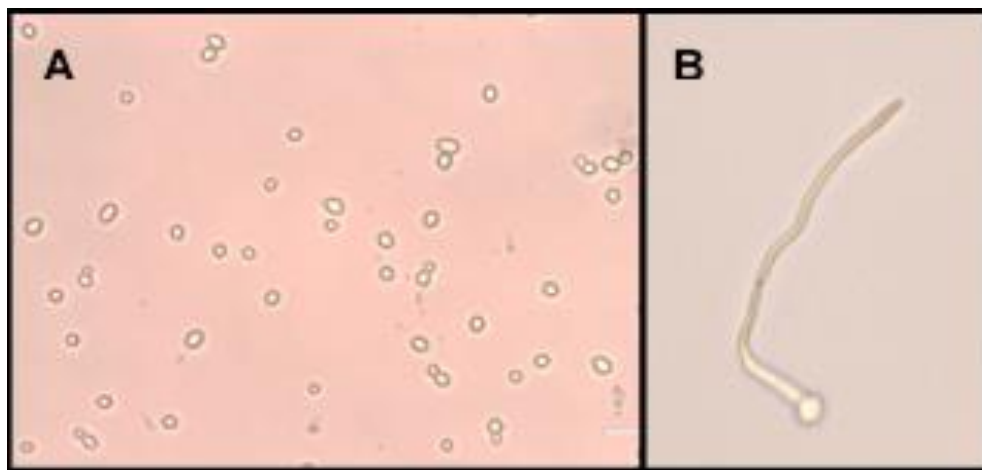


Figure 5.1: Growth of the CAF2-1 wild-type strain of *C. albicans*. (A) Growth at 30 °C to produce the yeast form. (B) Growth at 37 °C to produce the hyphal form that is more resistance to anti-fungal agents.

5.2.5 The growth curve of *C. albicans*

A single colony of *Candida* from a YPD agar plate was inoculated into the 50 ml YPD agar broth and grown overnight at 30 °C for a starter culture. The overnight culture was sub-cultured into 1600-fold dilution into fresh 20 mL of YPD broth medium and incubated with each compound at varying MIC values (MIC, 2x MIC, 0.5x MIC, 0.1x MIC). Each experiment was performed in triplicates and DMSO was used as a control. The increase in OD values was recorded for every hour and OD values were plotted against time.

5.2.6 Effect of small molecule inhibitors on biofilm formation

The effect of each compounds on biofilm formation was tested in 96-well polystyrene flat bottomed microtiter plates. The *Candida* culture were grown overnight on YPD broth medium at 30 °C. The overnight culture (25 mL) was centrifuged at 3200 rpm for 5 min and washed with PBS twice. The cells were vortexed and resuspended with 10 mL of RPMI 1640 medium. The cells were diluted from 1:100 to 1:1000 fold, and counted under a hemocytometer and adjusted to a final cell density of 1×10^6 cells/mL *Candida* suspension. Next, 100 μ L of suspension were aliquoted into 96-well plates, sealed with parafilm and incubated at 37 °C for 24 h. The next day, formation of biofilm was observed under the light microscope. The RPMI media was aspirated without disturbing the biofilm and washed carefully with PBS three times. The resulting biofilm was treated with each inhibitor in two-fold serial dilution concentration and incubated for 12 h at 37 °C. The resulting culture was discarded, washed with 2x PBS and the biofilm was treated with 40 μ L of MTT, 2 μ L of menadione and 158 μ L of PBS and incubated for 2 h in the dark. Metabolically active live cells have ability to reduce tetrazolium salt (MTT) to water-soluble, orange-colored formazan due to mitochondrial dehydrogenase activity that can be measure spectrophotometrically in a microtiter plate reader. The colorimetric absorbance of formazan was monitored at 490 nm using a UV VIS spectrophotometer and MBIC (minimum biofilm inhibitory concentration) values was calculated according to the results obtained. MBIC was defined as the lowest antifungal concentrations at which the value of A_{490} was comparable to the control biofilm formed by the same fungal isolate in the absence of antifungal agents. Each experiment was performed in duplicate. Due to the wide variations in absorbance of formazan at 490 nm of control samples, we are still optimizing

the final biofilm assay protocol to obtain the consistent and reproducible absorbance results.

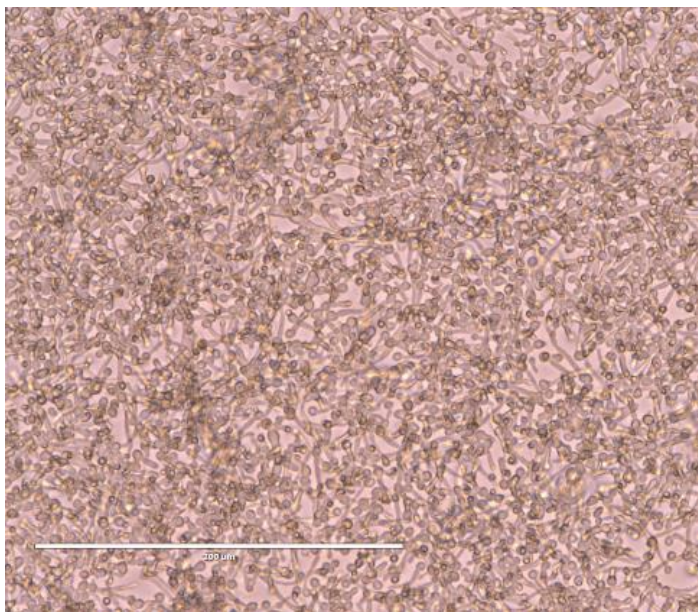


Figure 5.2: *Candida albicans* biofilm observed under a light microscope at 10x magnification

5.3 Results and discussion

5.3.1 Antifungal susceptibility bioassay

The top hits from library screening were evaluated *in vitro* against *Candida albicans*, but only those compounds that showed inhibition constant (K_i) values lower than $\sim 200 \mu\text{M}$ were considered potent and are shown in Table 5.1. The microbroth dilution assay showed that some of these benzoquinone derivatives (Figure 5.4) inhibited growth of this *Candida* strain with an MIC value ranging from $12.5 \mu\text{M}$ (2,3-dichloro-1,4-naphthoquinone) to $250 \mu\text{M}$ (p-hydroquinone). There was no inhibition of growth from the DMSO controls, confirming that inhibition was exclusively from our tested compounds. Uninhibited growth of *C. albicans* in the control wells without antifungals confirmed the viability of the fungal

inoculum. Also, there was no growth on the control without the fungal inoculum, confirming that the YPD broth used was not contaminated by microorganisms. The best inhibitors from this dilution assay were selected for further studies on the effect of a change in micromorphology from the yeast form to the hyphal form. Some of the compounds tested were found to be two-fold more active against the yeast form (naphthalene-2,3-dialdehyde, p-hydroquinone), while some are equally effective growth inhibitors against both the yeast and hyphal forms. The best inhibitor, the dichloro derivative of 1,4-naphthoquinone (MIC = 2.28 $\mu\text{g}/\text{mL}$, $K_i = 12.5 \mu\text{M}$) was found to be nearly as potent as the positive control, amphotericin B (2.5 $\mu\text{g}/\text{ml}$). This control is a related natural product analog of the parent compound shikonin, exhibited similar potency (MIC₈₀ = 2 to 8 $\mu\text{g}/\text{mL}$)¹⁰³ against *C. albicans*, suggesting that the naphthoquinone core is showing significant inhibition against *Candida* cells. Further elaboration of these initial hits has the potent to lead to potent new antifungal drug candidates. Although there is no linear, quantitative correlation between the IC₅₀ and the K_i values for these inhibitors, there is a general trend with the weaker inhibitors showing higher IC₅₀ values, and vice versa (Figure 5.3). The lack of quantitative correlation may be due to IC₅₀ values that are determined based on inhibition of whole cells of microorganisms, while K_i values are calculated by varying the inhibitor concentration against a particular purified enzyme following enzymatic kinetics using a Dixon plot analysis⁸.

Table 5.1 Effect of small molecule inhibitors against *Candida albicans*, with their measured K_i values against the purified enzyme, MIC, and IC_{50} values against cell growth

Screening of <i>Candida albicans</i> growth inhibitors			
ASADH inhibitors	K_i (μM)	fungal susceptibility	
		IC_{50} (μM)	MIC (μM)
2-chloro-1,4-naphthoquinone	4.1 ± 0.7	16.4 ± 2.0	25
2-bromo-1,4-naphthoquinone	6.1 ± 1.1	19.0 ± 2.9	25
2,3-dichloro-1,4-naphthoquinone	6.5 ± 0.3	9.8 ± 1.0	12.5
2,3-dichloro-5,8-dihydroxy-1,4-naphthoquinone	11.5 ± 1.3	21.1 ± 1.8	25
naphthalene-2,3-dialdehyde	45 ± 8	58.2 ± 4.8	62.5
dichloro,dicyano-1,4-benzoquinone	57.6 ± 6.5	149 ± 22	250
<i>p</i> -hydroquinone	65 ± 9	139 ± 19	250
tetrachloro-1,4-benzoquinone	66 ± 10	85.1 ± 9.5	125

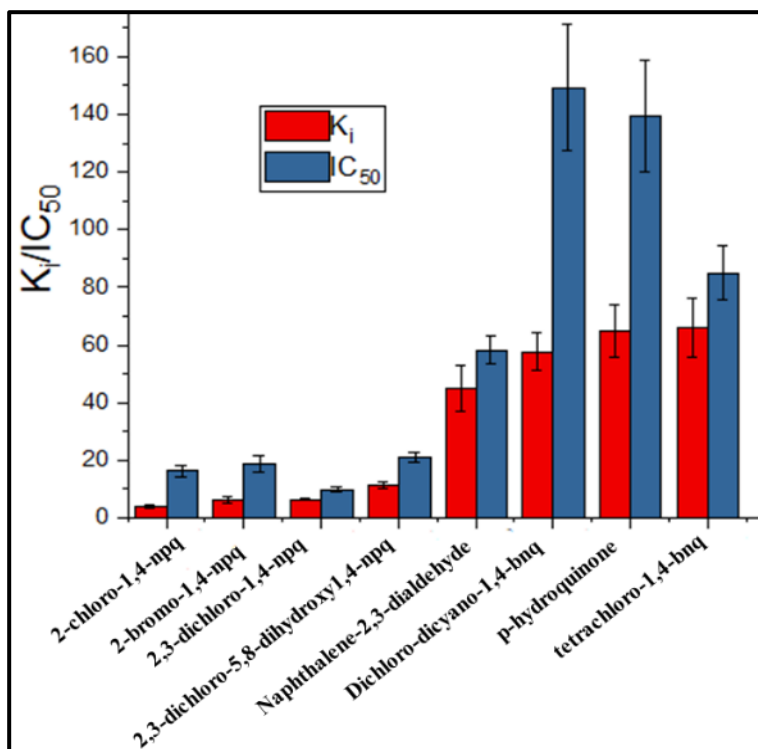


Figure 5.3: Relationship between K_i (*in vitro*) vs. IC_{50} (*in vivo*) values of small molecule inhibitors against *C. albicans*

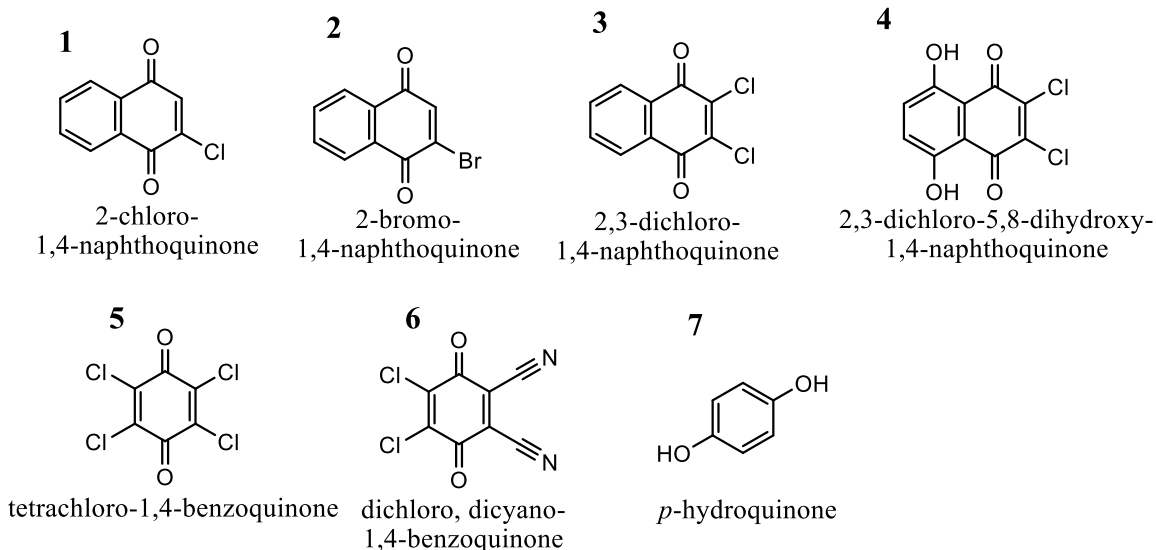


Figure 5.4: Structures of the most potent *C. albicans in vivo* growth inhibitors and *C. albicans* ASADH *in vitro* inhibitors

5.3.2 Inhibitor effects on *C. albicans* growth curves

The efficacy of each inhibitors on the growth profiles of *C. albicans* was determined based on continuous monitoring of changes in the optical density of fungal growth culture over time (24 h). Figure 5.5 (control, 0 μ M, black sigmoidal line) displayed the normal growth curves of the *Candida*, cultured under the normal growth condition in YPD medium. Both curves (control, 0 μ M, black sigmoidal line) are sigmoidal, with clear distinctions between the lag, log and stationary phases. In general, about 3 to 5 h was required by the cells to adjust in the normal growth environment before they were ready to proliferate, i.e. lag phase (the period until the first significant change in OD) and enter the log phase. However, the pattern of growth curves of the *Candida* species showed deviations from the normal sigmoidal behavior in presence of the tested compound, i.e. 2,3-dichloro-1,4-naphthoquinone (Figure 5.5). Each tested compound also showed concentration dependent variations in durations of the lag and log phases. Although each growth phase was affected by these compounds in different ways, the most obvious change induced by

exposure of the candidal cells was observed at the ~2x MIC (20 μM) concentration, where the growth curves shifted significantly to the right (from 4 h to 8 h) due to extension of the lag phase. While the 2x MIC caused a significant effect on growth, very low concentrations of 2,3-dichloro-1,4-naphthoquinone (0.1x MIC) did not cause a measurable effect on the growth rate (Figure 5.3, green triangles), suggesting that these compounds might be inhibiting the ASADH enzyme from *C. albicans*, and are showing similar concentration-dependent effects *in vivo*. Because our analysis was limited to a single strain of *Candida*, there is always the possibility of difference in growth inhibition from these compounds against different *Candida* species, since different species in the genus *Candida* can have different patterns of inhibitor sensitivity.

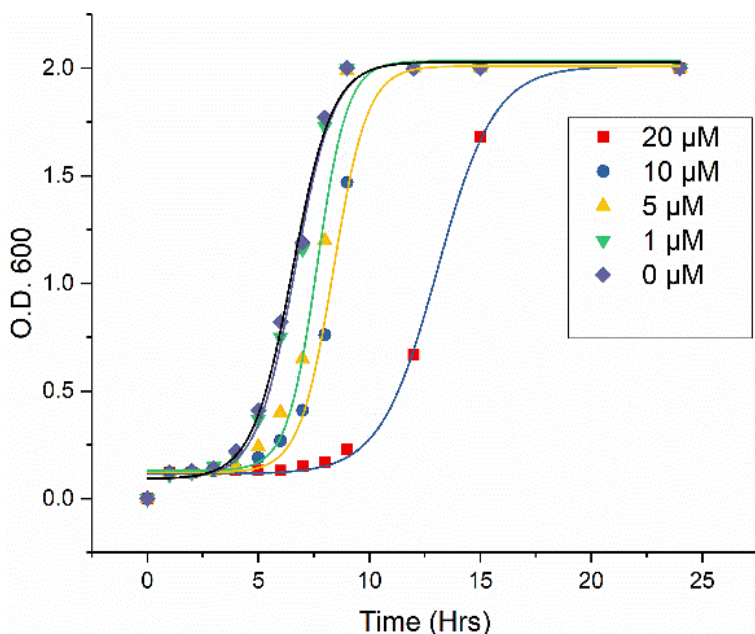


Figure 5.5: Effect of various concentrations of 2,3-dichloro-1,4-naphthoquinone ($K_i = 6.5 \pm 0.3 \mu\text{M}$, MIC = 12.5 μM) on the growth of *C. albicans*

5.4 Conclusions and future work

The most significant outcome of these studies is the observation that some of our potent fungal ASADH inhibitors also showed excellent antifungal activity against *C. albicans*. However, we will need additional tests with other pathogenic *Candida* strains, and more extensive pre-clinical studies in order to translate the potent antifungal activity of these compounds into antifungal drugs. Although a larger number of diversified structures and more compounds testing is required, the dichlorinated-1,4-naphthoquinones and their corresponding monosubstituted and related analogs display significant antifungal activity against *Candida albicans*, suggesting that this set of inhibitors could be useful as lead compounds for the development of simple and new antifungal drugs, especially against *Candida* spp. Also, the formazan based biofilm assay will need to be optimized for improved reproducibility, and each of the benzoquinone derivatives will need to be tested for their anti-biofilm properties.

Chapter 6

The Enzymology of Canavan Disease

6.1 Introduction

Canavan disease (CD) is an autosomal recessive neurological disorder observed in infants and is caused by the deficiency of the enzyme aspartoacylase leading to progressive spongy degeneration of the white matter in the human brain¹⁰⁴⁻¹⁰⁵. CD is a type of leukodystrophy that impedes the growth and development of myelin sheath that is important for the nerve impulses transmission¹⁰⁵. Multiple mutations in the *acy2* gene that encodes for aspartoacylase (ASPA), causes the accumulation of its substrate, N-acetyl aspartate (NAA), which is the primary cause of CD. ASPA catalyzes the hydrolysis of the substrate NAA in oligodendrocytes to produce acetate and aspartate¹⁰⁶. The catalytic deficiency of ASPA leads to insufficient levels of acetate and accumulation of NAA, which is the diagnostic marker of the CD. NAA is synthesized in the neurons by the enzyme aspartate N-acetyltransferase (ANAT) from two substrates L-aspartate and acetyl-CoA, and is subsequently hydrolyzed in oligodendrocytes to L-aspartic acid and acetate¹⁰⁷ (Figure 6.1).

Several hypotheses have been proposed to account for the demyelination associated with CD. One hypothesis states that myelinating oligodendrocytes require NAA-derived

acetate in order to carry out the energy-dependent process of myelin sheath synthesis, and the lack of the NAA-derived acetate is considered to inhibit the process¹⁰⁸. The second hypothesis suggests that the cause of the demyelination in CD is not due to the lack of acetate obtained from NAA, but the accumulation of unhydrolyzed NAA¹⁰⁹. These studies suggest that the accumulation of NAA in neurons impairs antioxidant defense and induces oxidative damage to proteins, which is the likely cause of higher neurotoxicity in CD patients.

There is no treatment of CD to date, and patients are compelled to follow palliative measures. Several treatment strategies have been developed to treat CD affected patients. Enzyme replacement therapy, with replacement of the defective aspartoacylase with active engineered enzyme has shown some success in an animal model of CD. The human ASPA protein has been PEGylated specifically on the surface lysyl groups to decrease an immune response and increase its circulation half-life. There was significant enhancement in ASPA activity when PEGylated ASPA was administered to CD affected mice, which also led to decreases in the elevated levels of the substrate NAA¹¹⁰. This is a potential viable approach but can be limited for treatment of neurological diseases because of the presence of blood brain barrier which restricts the entry of macromolecules inside and outside of the brain. Gene replacement therapy has also been considered as alternative CD treatment option, where the mutated gene was replaced with a fully functional copy of the same gene¹¹¹. This therapy was performed through intraventricular injection of plasmids through the human body, but the success can be limited due to the low rates of diffusion, aggregate formation and endotoxin contamination.

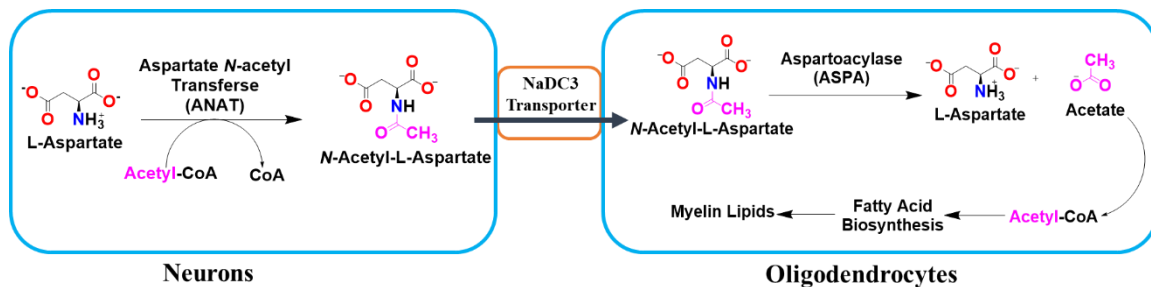


Figure 6.1: Schematic representation of the biological role of ANAT and aspartoacylase in the human brain. NAA is synthesized from L-aspartate and acetyl-CoA by ANAT in neurons. A sodium ion-dependent, NAA transporter (NaCD3), transports NAA into oligodendrocytes where L-aspartate will be regenerated, and acetate released by hydrolysis of NAA catalyzed by aspartoacylase. The resulting acetate serves as the precursor for myelin lipid biosynthesis.

For several decades, it was believed that mutation in the *acy2* gene and the resulting deficiency of acetate was the primary cause of CD. However, recently knockout studies on the *Nat8l* gene (encoding ANAT) showed normal myelination and also eliminated the leukodystrophy symptoms in a Canavan disease mouse model¹¹². ANAT belongs to the family of acetyltransferase and catalyze the conversion of L-aspartate and acetyl-CoA into NAA, one of the most abundant metabolite in the brain. In addition to the possible role of ANAT in CD, it has also been shown that overexpression of ANAT and the subsequent rise in NAA levels is linked with different life-threatening cancers such as lung cancer¹¹³ and ovarian cancer¹¹⁴.

6.2 Challenges in ANAT study

The enzyme aspartoacylase has been extensively studied, but there have been few studies regarding the enzyme aspartate N-acetyltransferase. The inherent challenge is to obtain pure ANAT enzyme, complicated by its membrane-bound nature¹¹⁵ and its

sensitivity towards detergents¹¹⁶. Several fusion constructs with different solubilization partners of the human form of ANAT have previously been studied in our lab designed to improve its solubility. These fusion constructs have been purified¹⁰⁷, however these enzyme forms have not yielded suitable crystals for structural studies. Our related efforts have been focused on purifying the mouse form of ANAT (mANAT), with an aim to improve enzymatic purity and yield in order to obtain a crystal structure.

6.3 Cloning of mANAT gene

The *E. coli* codon-optimized gene encoding aspartate N-acetyltransferase from *Mus musculus* was synthesized from Genscript (NJ, USA). The gene was subcloned into a modified pET28a (+) expression vector containing a N-terminal maltose binding protein tag and a C-terminus hexahistidine tag, using the EcoRI and XhoI restriction sites¹⁰⁷. The mANAT plasmid was then transformed into a DH5 α *E. coli* cell line and positive colonies were grown overnight. The construct was purified, and DNA sequence was confirmed by restriction digestion and by DNA sequencing. The plasmid was transformed into a BL21 DE3 derivative of *E. coli* for protein expression using a strong T7 promoter. To prepare the bulk cultures a single colony from the transformation was introduced into a 50 mL LB broth, grown overnight at 37 °C and 250 rpm shaking. This starter culture was used to inoculate four 1 L bulk cultures. The cultures were incubated at 37 °C and 250 rpm until it reaches an OD₆₀₀ of 0.6 to 0.8, after which the cultures were induced with 0.5 mM isopropyl B-D-thiogalactopyranoside (IPTG). The temperature of the incubator shaker was then reduced to 16 °C and the cells were allowed to grow for 18 h. Cells were harvested by centrifugation at 10,000 rpm for 10 min and the pellet was stored at -80 °C.

6.4 Purification of mANAT

The human form of ANAT has been expressed in a soluble and active form by using a fusion protein expression with maltose binding protein (MBP), and a similar strategy was followed for mouse ANAT purification. All protein extraction and purification steps were done at 4 °C unless otherwise specified by following the published protocol of purifying hANAT¹⁰⁷. The mANAT protein was first purified using a Ni-IMAC column, followed by an amylose column with elution with a maltose gradient. The chromatogram profile and the SDS gel obtained after Ni-IMAC (Figure 6.2 left and right, respectively) are shown below. The active fractions from mANAT after Ni-IMAC were subjected to amylose column for removing small interfering bands found lower and higher to the expected molecular weight. The active fractions from the final purification step and SDS gel (Figure 6.3 left and right, respectively) were collected, dialyzed overnight, concentrated and stored at -20 °C for further use. SDS PAGE of the eluted fractions from the final purification showed a single band corresponding to the correct molecular weight of the protein (mANAT fusion protein \approx 78kDa). The pure and active fractions from the amylose column was dialyzed overnight and concentrated to 10 mg/ml and stored at -80 °C until use. MBP fused mANAT protein was kept at 4 °C for one week and the enzyme activity was monitored every day for analyzing the stability of the enzyme. There was no significant decrease of enzyme activity after 7 days.

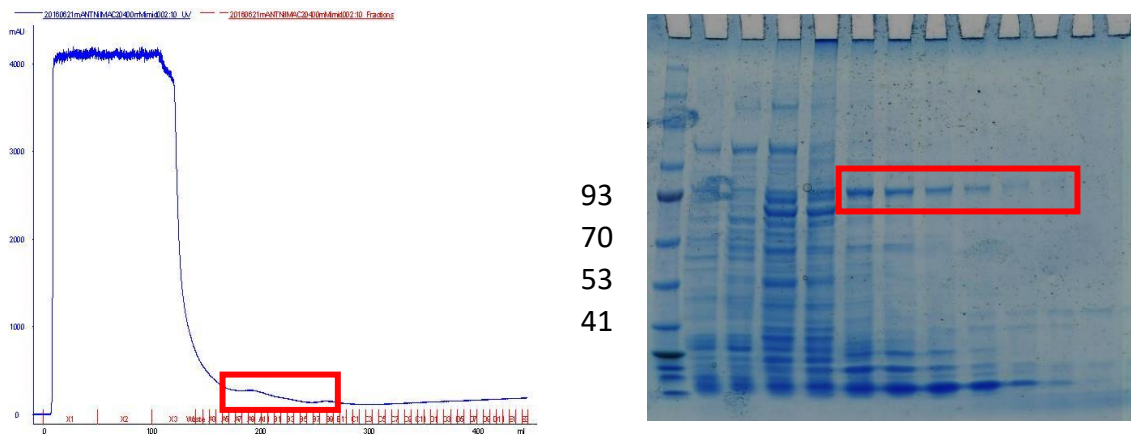


Figure 6.2: (Right) Chromatogram profile after Ni-IMAC fraction of mANAT using a 20 to 400 mM imidazole gradient. The fractions inside the red square showed activity. Left: SDS PAGE profile of eluted fractions, single band \approx 78 kDa corresponding to mANAT.

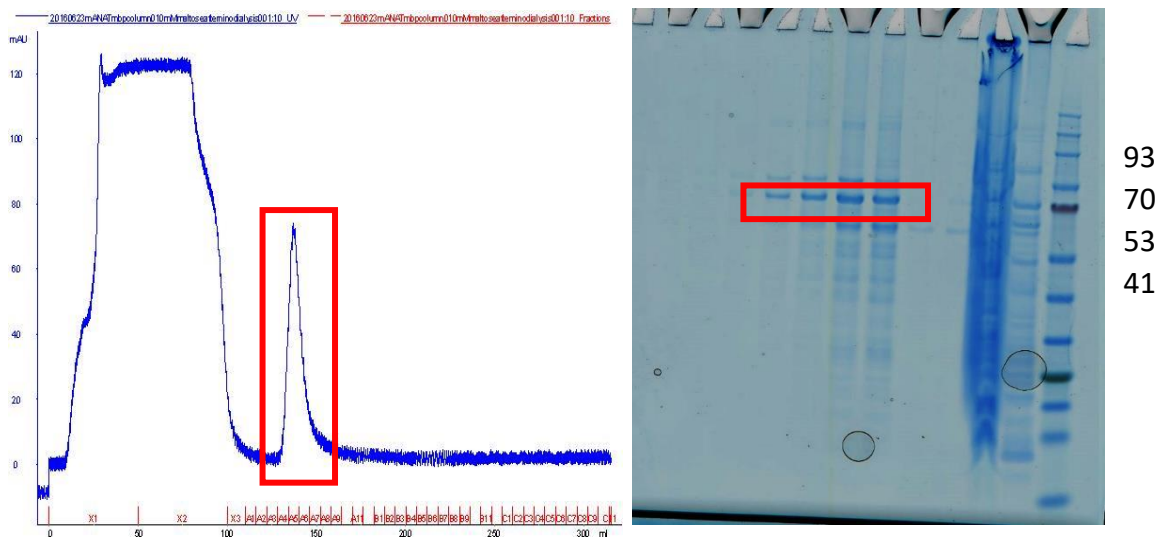


Figure 6.3 Left: Chromatogram profile after amylose column of mANAT using a 0 to 10 mM maltose gradient. The fractions inside the red square showed activity. Right: SDS-PAGE profile of eluted fractions, single band \approx 78 kDa corresponding to mANAT.

6.5 ANAT kinetic assay and biochemical properties

ANAT activity was assayed by monitoring the production of Coenzyme A with 5-(3-Carboxy-4-nitrophenyl)disulfanyl-2-nitrobenzoic acid (DTNB)¹⁰⁷, using a SpectraMax 190 spectrophotometer plate reader (Molecular Devices, CA). The DTNB based activity assay (Figure 5.4) contains 8 mM potassium phosphate, 4 mM Tris-HCl, 120 mM NaCl, 4% Glycerol, 40 μ M DTNB, 40 μ M Acetyl-CoA, and 2 mM L-aspartate at pH 7, in a total of 200 μ l reaction mixture. The increasing absorption of TNB²⁻ at 412 nm ($\epsilon = 14.15 \text{ mM}^{-1} \text{ cm}^{-1}$) was monitored for up to 15 min during the course of reaction. The biochemical properties of mANAT were analyzed using this assay and the mouse form of enzyme showed similar properties to that of human forms. The K_m for the substrate was found to be 0.25 mM, a 1.5-fold higher K_m than hANAT, and the k_{cat} was found to be 0.0062 s^{-1} , an 11-fold lower k_{cat} than hANAT. The similarity in kinetic properties is due to the high sequence similarity (93%) between the human and mouse forms of ANAT.

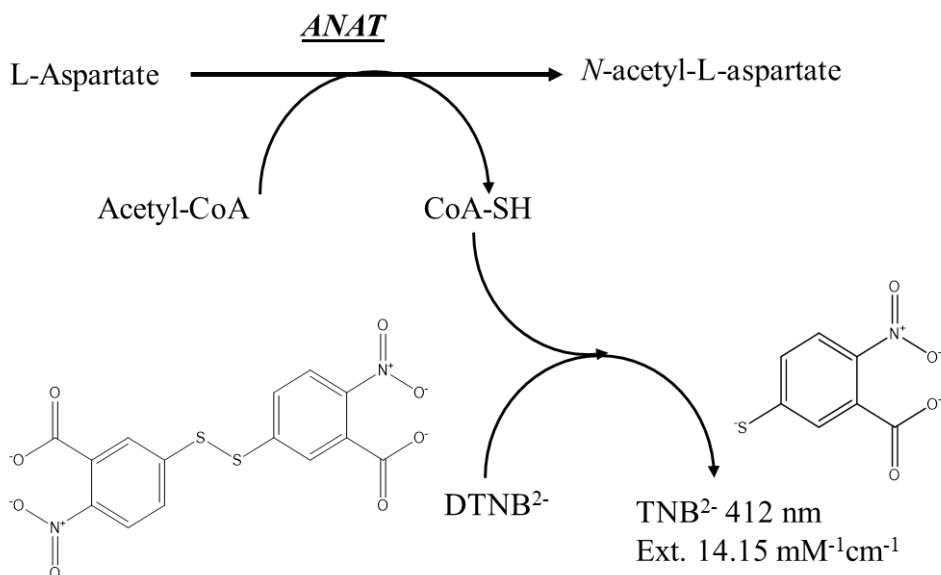


Figure 6.4 Schematic representation of DTNB assay for ANAT activity measurement

6.6 Crystallization of mANAT

In order to identify the conditions for crystallization for each of the ANAT enzymes a pre-crystallization test (PCT) was performed, at 8 mg/ml for mANAT. 500 μ L of each PCT reagent was added as precipitant, and 1 μ L protein + 1 μ L precipitant was set up as a crystallizing drop. A light granular precipitate was observed after 24 h from each protein sample suggesting optimum reasonable concentration for crystal screening. Index screening from Hampton research (Index 1 and 2) was performed with 96 unique crystallizing reagents at 6 mg/ml and 10 mg/ml enzyme concentrations for the initial index screening for mANAT. No significant hits were found from the screening, with a lot of precipitating drops observed at 10 mg/ml and mainly clear drops at 6 mg/ml. A few of the drops contained feathers, thin blades, and spherules, but most of the drops were either clear or with heavy precipitate. Since ANAT is a membrane-associated protein, it is less likely to obtain a high number of initial hits from Index screening. In order to increase the probability of initial hits, MembFrac (Hampton Research) and Wizard screening (Molecular Dimensions) were performed with mANAT at 8 mg/ml. Despite several screening trials, we didn't obtain a good starting condition for mANAT crystallization. Most of the drop from MembFrac screening precipitated while some of them remained as clear drops (Figure 6.5). The clear drops from Index screening precipitated after 2 months and the Wizard screening kit also didn't yield crystals to start further optimization.

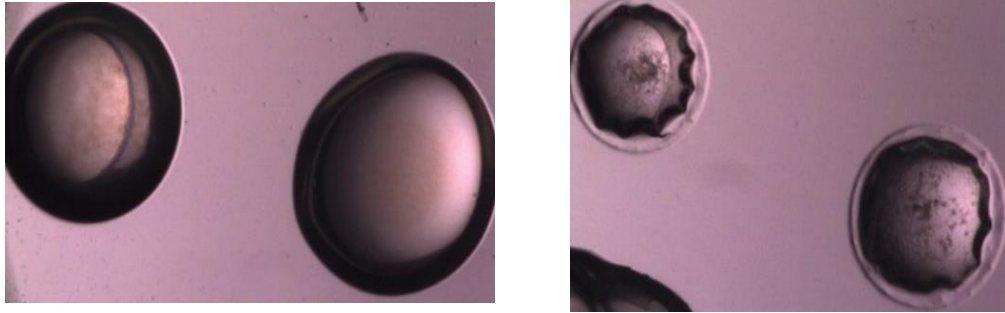


Figure 6.5: mANAT MembFrac screening results at 8 mg/ml left) clear drop from crystal condition 0.05 M Zinc acetate dihydrate, 20% w/v Polyethylene glycol 3,350. Right) precipitated drop from crystal condition 0.2 M Ammonium acetate, 0.1 M HEPES pH 7.5, 45% v/v 2-Methyl-2,4-pentanediol.

6.7 Protein engineering of ANAT

Several crystallization trials with commercial screening kits available in the lab didn't yield any starting point for crystallization optimization. Different protein engineering strategies has already been tried in order to obtain a crystallizable form of hANAT, but so far have not been successful in producing initial starting points. According to homology model ¹¹⁷, ANAT was found to have a transmembrane helix with a helix turn helix region. Several membrane associated proteins were crystallized by removing the transmembrane helical region and replacing it with small soluble proteins such as lysozyme¹¹⁸ or cytochrome C. We have tried a similar cloning strategy for mANAT, with the approach of removing the transmembrane helix and replacing it with soluble lysozyme. The lysozyme construct was purchased from Addgene (plasmid # 18111) and two sets of oligonucleotides primers for amplification of lysozyme and also removal of helical segment from mANAT were designed. The primers were used to PCR amplify the mANAT gene with deletion of the transmembrane region and also amplify the lysozyme. The

primers used for amplification of lysozyme gene with an overlap region in mouse ANAT are:

Forward primer:

5'-TTCGTGGCCTGCGTCAGCACATATTTGAAATGTTACGTATAGATGAAG-3'

Reverse primer:

5'-GCCAGGATCACCTTACGGCTCCAAGTGCCAGTTCTAAAC-3'.

An additional set of primers for deleting the helical subdomain are:

Forward primer:

5'-AGCCGTAAGGTGATCCTGGCG-3'

Reverse primer:

5'-GTGCTGACGCAGGCCACG-3'

The PCR amplified gene was gel purified and Gibson assembly was performed using 1:3 ratio of vector to insert and 1:1 ratio of the Gibson master mix with insert vector complex and was transformed in DH5 α *E. coli* cell line. Positive colonies were used for colony PCR in order to identify the correct construct. The construct was confirmed by restriction digestion and DNA sequencing. We are now optimizing the expression and purification of the enzyme from this engineered construct to get a form for use in initial crystallization screening.

6.8 Bisubstrate inhibitors of ANAT

Designing selective inhibitors against ANAT has the potential to slow the accumulation of NAA, and to be developed as a starting point for ANAT treatment strategy. A bisubstrate analog inhibitor of an enzyme possess structural features of both substrates of an enzyme. The substrates for ANAT are L-aspartate and acetyl-CoA, and

several bisubstrate analog inhibitors of ANAT have now been synthesized, with nanomolar binding affinities against this enzyme. Generally, bisubstrate analogs are synthesized to study the mechanism of an enzyme¹¹⁹, to analyze the effect of specific mutations in substrate recognition¹²⁰ or to mimic the transition state¹²¹ to understand the structural aspects of an enzyme. These bisubstrate inhibitors typically have significantly higher affinity to the enzyme since they possess structural motifs from both of the substrates.

6.9 Bisubstrate inhibitor design and screening

A series of bisubstrate analog inhibitors against ANAT have been synthesized (Mutthamsetty and Viola, unpublished results) that incorporate the structural features of both substrates, L-aspartate and acetyl CoA. Coenzyme A (CoA) functions primarily by activating different acyl groups *via* formation of a thioester for the subsequent transfer to different acceptor molecules.¹²² The extended coenzyme A structure is composed of adenosine-3'-monophosphate linked by a pyrophosphate to a pantothenate coupled in a peptide linkage to β -mercaptoethylamine, and provides the specificity and binding affinity to its enzymatic binding partners.

The direct coupling of the acetyl group of the substrate N-acetylaspartate to the thiol group of coenzyme A (second substrate) yielded a bisubstrate analog (BA1) with nanomolar binding affinity (275 nM) against hANAT, and a second analog with one more methylene group between the thiol group and the acetyl group (BA2) with even higher affinity (48 nM). However, when screened separately, the individual moieties ADP, pantothenate, and N-acetyl aspartate had little or no affinity for the enzyme (Table 6.1). These results indicate a requirement for the complete ensemble of interactions to achieve strong binding of this analog. A series of truncated versions of the bisubstrate analog

(Figure 6.6) have been synthesized and tested. The N-chloroacetyl derivative of aspartate (TA1c) shows an 8-fold improvement in binding affinity, while the N-bromoacetyl derivative of aspartate (TA1b) does not show any measurable binding affinity against hANAT (Table 6.1). When cysteamine moiety is replaced with cysteine that introduced an additional carboxyl group (TA2a), resulting in poor binding to ANAT.

The synergistic effects of different truncated bisubstrate analogs in the presence of different nucleotide analogs such as ATP, ADP and 3',5'-ADP have also been examined to test the possible effects of nucleotide binding on the affinity of the truncated bisubstrate analogs. Each of the nucleotide analogs were included in excess in the reaction ($\sim 5x K_i$) values to measure any possible effects on the analogs binding to ANAT. While the addition of excess 3',5'-ADP had no effect on truncated analog binding, both 5'-ADP and ATP did show synergistic effects on analog binding. The addition of higher concentration of ADP had a greater synergistic effect on the binding of the longer truncated analogs (TA2a), with up to a 60% improvement in the K_i value. For the shorter truncated analogs (TA1) the presence of ATP had the greater synergistic effect, leading to a 65% - 80% improvement in binding affinity for TA1 and TA1c respectively. These results suggest that as improved inhibitors are developed that optimize the potential interactions in the substrate and thiol end of the CoA binding site of ANAT, the normal cellular levels of ADP and ATP could serve to enhance inhibitor binding to this target enzyme.

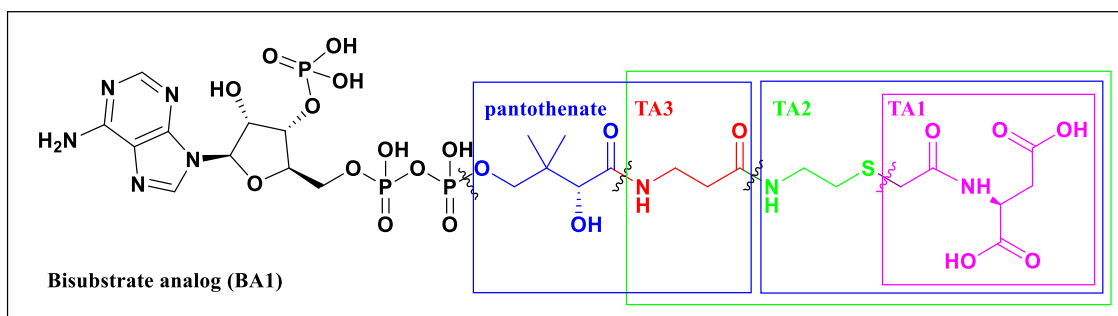


Figure 6.6: ANAT bisubstrate analog and its truncation series. The sub-structures of acetyl CoA-aspartate bisubstrate analogs are indicated, from *N*-acetyl aspartate (TA1), to the cysteamine adduct (TA2), the β -alanine adduct (TA3) and the bridging pantothenate.

Table 6.1 Kinetic evaluation of truncated analog inhibitors of ANAT

Analog number	truncated analog name	K_i (mM)
TA1	<i>N</i> -acetyl aspartate	1.60 ± 0.12
TA1c	<i>N</i> -chloroacetyl aspartate	0.200 ± 0.040
TA1b	<i>N</i> -bromoacetyl aspartate	>2
TA2	<i>N</i> -(acetylcysteaminy) aspartate	>2
TA2a	<i>N</i> -(acetylcysteinyl) aspartate	1.03 ± 0.20
TA3	<i>N</i> -(acetylcysteaminy)- β -alanyl) aspartate	2.10 ± 0.41

Table 6.2 Synergistic effect of simultaneous binding of ANAT inhibitors

Analog number	K_i (mM) (plus adenosine inhibitor)		
	none	+ 5 mM ATP	+ 5.5 mM ADP
TA1	1.61 ± 0.12	0.58 ± 0.08	0.85 ± 0.13
TA1c	0.200 ± 0.040	0.043 ± 0.005	0.170 ± 0.025
TA1b	>2	n/a	n/a
TA2	2.10 ± 0.37	1.52 ± 0.20	1.46 ± 0.19
TA2a	1.03 ± 0.20	0.66 ± 0.10	0.41 ± 0.05
TA3	2.11 ± 0.41	1.51 ± 0.15	1.48 ± 0.12

6.10 Conclusions and future work

Cloning and purification of two orthologs of a membrane bound enzyme involved in neurological disease is the first step in drug design however crystal structure determination is of utmost importance to elucidate the detailed structure of the enzyme. While screening different commercial and custom-made crystallization kit has been performed, new approaches to crystallizing difficult membrane proteins, such as the lipid cubic phase (LCP) and capillary counter diffusion methods of crystallization will be performed with an aim to obtain diffraction quality crystals. Morpheus screening (LMB, Cambridge) will be employed to screen a wider variety of crystallization conditions. Surface entropy reduction (SER) in the MBP construct, by replacing some of the charges residues on the surface of MBP into alanine such as D83A/K84A, E173A/N174A, K240A, has been shown to significantly improve its crystallizability, and this strategy will be employed to increase the probability of ANAT crystallization. The bisubstrate analogs showing nanomolar inhibition are used in co-crystallization experiments to ease the crystallization process. Replacements of the important charged and polar functional groups in the bisubstrate analog will be explored to produce more drug-like compounds and efforts will be made to design analogs that mimic the hydrophobic region of the cofactor structure that retain the high affinity and selectivity against ANAT.

References

1. Brown, G. D.; Denning, D. W.; Gow, N. A.; Levitz, S. M.; Netea, M. G.; White, T. C., Hidden killers: human fungal infections. *Science translational medicine* **2012**, *4* (165), 165rv13.
2. Lai, C. C.; Tan, C. K.; Huang, Y. T.; Shao, P. L.; Hsueh, P. R., Current challenges in the management of invasive fungal infections. *Journal of infection and chemotherapy : official journal of the Japan Society of Chemotherapy* **2008**, *14* (2), 77-85.
3. Park, B. J.; Wannemuehler, K. A.; Marston, B. J.; Govender, N.; Pappas, P. G.; Chiller, T. A., Estimation of the current global burden of cryptococcal meningitis among persons living with HIV/AIDS. *AIDS (London, England)* **2009**, *23* (4), 525-530.
4. Robbins, N.; Wright, G. D.; Cowen, L. E., Antifungal Drugs: The Current Armamentarium and Development of New Agents. *Microbiology Spectrum* **2016**, *4* (5).
5. Vandeputte, P.; Ferrari, S.; Coste, A. T., Antifungal resistance and new strategies to control fungal infections. *International journal of microbiology* **2012**, *2012*, 713687.
6. Perea, S.; Patterson, T. F., Antifungal resistance in pathogenic fungi. *Clinical infectious diseases : an official publication of the Infectious Diseases Society of America* **2002**, *35* (9), 1073-80.
7. *Antibiotic Resistance Threats in the United States*; Center for Disease Control and Prevention: **2013**.
8. Dixon, D. M.; Walsh, T. J., Antifungal agents. *Internet Baron , Medical Microbiology Textbook* (<http://gsbs.utmb.edu/microbook/ch079.htm>.) **1996**.
9. Seyedmousavi, S.; Rafati, H.; Ilkit, M.; Toloee, A.; Hedayati, M. T.; Verweij, P., Systemic Antifungal Agents: Current Status and Projected Future Developments. *Methods in Molecular Biology (Clifton, N.J.)* **2017**, *1508*, 107-139.
10. Srinivasan, A.; Lopez-Ribot, J. L.; Ramasubramanian, A. K., Overcoming antifungal resistance. *Drug Discovery Today Technology* **2014**, *11* (0), 65-71.
11. Parente-Rocha, J. A.; Bailao, A. M.; Amaral, A. C.; Taborda, C. P.; Pაცეც, J. D.; Borges, C. L.; Pereira, M., Antifungal Resistance, Metabolic Routes as Drug Targets, and

New Antifungal Agents: An Overview about Endemic Dimorphic Fungi. *Mediators Inflamm* **2017**, 2017, 9870679.

12. Ramakrishnan, J.; Rathore, S. S.; Raman, T., Review on fungal enzyme inhibitors - potential drug targets to manage human fungal infections. *RSC Advances* **2016**, 6 (48), 42387-42401.

13. Cuenca-Estrella, M., Antifungal drug resistance mechanisms in pathogenic fungi: from bench to bedside. *Clinical Microbiology Infection* **2014**, 20 Suppl 6, 54-9.

14. Costerton, J. W.; Stewart, P. S.; Greenberg, E. P., Bacterial biofilms: a common cause of persistent infections. *Science (New York, N.Y.)* **1999**, 284 (5418), 1318-22.

15. Janeczko, M.; Maslyk, M.; Kubinski, K.; Golczyk, H., Emodin, a natural inhibitor of protein kinase CK2, suppresses growth, hyphal development, and biofilm formation of *Candida albicans*. *Yeast* **2017**, 34 (6), 253-265.

16. Pierce, C. G.; Uppuluri, P.; Tristan, A. R.; Wormley, F. L., Jr.; Mowat, E.; Ramage, G.; Lopez-Ribot, J. L., A simple and reproducible 96-well plate-based method for the formation of fungal biofilms and its application to antifungal susceptibility testing. *Nature Protocols* **2008**, 3 (9), 1494-500.

17. Viola, R. E.; Faehnle, C. R.; Blanco, J.; Moore, R. A.; Liu, X.; Arachea, B. T.; Pavlovsky, A. G., The catalytic machinery of a key enzyme in amino Acid biosynthesis. *Journal of Amino Acids* **2011**, 2011, 352538.

18. Ragkousi, K.; Eichenberger, P.; van Ooij, C.; Setlow, P., Identification of a new gene essential for germination of *Bacillus subtilis* spores with Ca²⁺-dipicolinate. *Journal of Bacteriology* **2003**, 185 (7), 2315-29.

19. van Heijenoort, J., Recent advances in the formation of the bacterial peptidoglycan monomer unit. *Natural Products Reports* **2001**, 18 (5), 503-19.

20. Blanco, J.; Moore, R. A.; Faehnle, C. R.; Viola, R. E., Critical catalytic functional groups in the mechanism of aspartate-beta-semialdehyde dehydrogenase. *Acta crystallographica. Section D, Biological crystallography* **2004**, 60 (Pt 10), 1808-15.

21. Blanco, J.; Moore, R. A.; Faehnle, C. R.; Coe, D. M.; Viola, R. E., The role of substrate-binding groups in the mechanism of aspartate-beta-semialdehyde dehydrogenase. *Acta crystallographica. Section D, Biological crystallography* **2004**, 60 (Pt 8), 1388-95.

22. Gao, G.; Liu, X.; Pavlovsky, A.; Viola, R. E., Identification of selective enzyme inhibitors by fragment library screening. *Journal of Biomolecular Screening* **2010**, 15 (9), 1042-50.

23. Arachea, B. T.; Liu, X.; Pavlovsky, A. G.; Viola, R. E., Expansion of the aspartate beta-semialdehyde dehydrogenase family: the first structure of a fungal ortholog. *Acta crystallographica. Section D, Biological crystallography* **2010**, *66* (Pt 2), 205-12.
24. Blanco, J., A structural basis for the mechanism of aspartate- -semialdehyde dehydrogenase from *Vibrio cholerae*. *Protein Science* **2003**, *12* (1), 27-33.
25. Karsten, W. E.; Viola, R. E., Chemical and kinetic mechanisms of aspartate-beta-semialdehyde dehydrogenase from *Escherichia coli*. *Biochimica et biophysica acta* **1991**, *1077* (2), 209-19.
26. Blanco, J.; Moore, R. A.; Viola, R. E., Capture of an intermediate in the catalytic cycle of L-aspartate-beta-semialdehyde dehydrogenase. *Proceedings of the National Academy of Sciences of the United States of America* **2003**, *100* (22), 12613-7.
27. Faehnle, C. R.; Le Coq, J.; Liu, X.; Viola, R. E., Examination of key intermediates in the catalytic cycle of aspartate-beta-semialdehyde dehydrogenase from a gram-positive infectious bacteria. *The Journal of biological chemistry* **2006**, *281* (41), 31031-40.
28. James, C. L.; Viola, R. E., Production and characterization of bifunctional enzymes. Substrate channeling in the aspartate pathway. *Biochemistry* **2002**, *41* (11), 3726-31.
29. Hadfield, A.; Shammass, C.; Kryger, G.; Ringe, D.; Petsko, G. A.; Ouyang, J.; Viola, R. E., Active site analysis of the potential antimicrobial target aspartate semialdehyde dehydrogenase. *Biochemistry* **2001**, *40* (48), 14475-83.
30. Faehnle, C. R.; Ohren, J. F.; Viola, R. E., A new branch in the family: structure of aspartate-beta-semialdehyde dehydrogenase from *Methanococcus jannaschii*. *Journal of Molecular Biology* **2005**, *353* (5), 1055-68.
31. Li, Q.; Mu, Z.; Zhao, R.; Dahal, G.; Viola, R. E.; Liu, T.; Jin, Q.; Cui, S., Structural Insights into the Tetrameric State of Aspartate- β -semialdehyde Dehydrogenases from Fungal Species. *Scientific Reports* **2016**, *6*, 21067.
32. Rodrigues, M. L.; Alviano, C. S.; Travassos, L. R., Pathogenicity of *Cryptococcus neoformans*: virulence factors and immunological mechanisms. *Microbes and Infection* **1999**, *1* (4), 293-301.
33. Buchanan, K. L.; Murphy, J. W., What makes *Cryptococcus neoformans* a pathogen? *Emerging Infectious Disease Journal* **1998**, *4* (1), 71-83.
34. Lin, S. J.; Schranz, J.; Teutsch, S. M., Aspergillosis case-fatality rate: systematic review of the literature. *Clinical infectious diseases : an official publication of the Infectious Diseases Society of America* **2001**, *32* (3), 358-66.

35. Tymoshenko, S.; Oppenheim, R. D.; Agren, R.; Nielsen, J.; Soldati-Favre, D.; Hatzimanikatis, V., Metabolic Needs and Capabilities of *Toxoplasma gondii* through Combined Computational and Experimental Analysis. *PLoS computational biology* **2015**, *11* (5), e1004261.
36. Gautam, B.; Singh, G.; Wadhwa, G.; Farmer, R.; Singh, S.; Singh, A. K.; Jain, P. A.; Yadav, P. K., Metabolic pathway analysis and molecular docking analysis for identification of putative drug targets in *Toxoplasma gondii*: novel approach. *Bioinformatics* **2012**, *8* (3), 134-41.
37. Shevchenko, A.; Tomas, H.; Havlis, J.; Olsen, J. V.; Mann, M., In-gel digestion for mass spectrometric characterization of proteins and proteomes. *Nature Protocols* **2007**, *1* (6), 2856-2860.
38. Perkins, D. N.; Pappin, D. J. C.; Creasy, D. M.; Cottrell, J. S., Probability-based protein identification by searching sequence databases using mass spectrometry data. *Electrophoresis* **1999**, *20* (18), 3551-3567.
39. Liu, Y. C.; Roujeinikova, A., Expression, refolding, purification and crystallization of the sensory domain of the TlpC chemoreceptor from *Helicobacter pylori* for structural studies. *Protein Expression and Purification* **2015**, *107*, 29-34.
40. Zhang, J. H.; Chung, T. D.; Oldenburg, K. R., A Simple Statistical Parameter for Use in Evaluation and Validation of High Throughput Screening Assays. *Journal of Biomolecular Screening* **1999**, *4* (2), 67-73.
41. Dahal, G.; Viola, R. E., Structure of a fungal form of aspartate semialdehyde dehydrogenase from *Cryptococcus neoformans*. *Acta Crystallography F Struct Biol Commun* **2015**, *71* (Pt 11), 1365-71.
42. Moore, R. A.; Bocik, W. E.; Viola, R. E., Expression and Purification of Aspartate α -semialdehyde Dehydrogenase from Infectious Microorganisms. *Protein Expression and Purification* **2002**, *25*, 189-194.
43. Hajduk, P. J.; Greer, J., A decade of fragment-based drug design: strategic advances and lessons learned. *Nature reviews. Drug discovery* **2007**, *6* (3), 211-219.
44. Jhoti, H.; Cleasby, A.; Verdonk, M.; Williams, G., Fragment-based screening using X-ray crystallography and NMR spectroscopy. *Current Opinion in Chemical Biology* **2007**, *11* (5), 485-93.
45. Hopkins, A. L.; Groom, C. R.; Alex, A., Ligand efficiency: a useful metric for lead selection. *Drug Discovery Today* **2004**, *9* (10), 430-1.

46. Gao, G.; Liu, X.; Pavlovsky, A.; Viola, R. E., Identification of Selective Enzyme Inhibitors by Fragment Library Screening. *Journal of Biomolecular Screening* **2010**, *15*, 1042-1050.
47. Cao, J.; Forrest, J. C.; Zhang, X., A screen of the NIH Clinical Collection small molecule library identifies potential anti-coronavirus drugs. *Antiviral Research* **2015**, *114* (0), 1-10.
48. Congreve, M.; Carr, R.; Murray, C.; Jhoti, H., A 'Rule of Three' for fragment-based lead discovery? *Drug Discovery Today* **2003**, *8*, 876-877.
49. Dixon, M., The determination of enzyme inhibitor constants. *The Biochemical Journal* **1953**, *55* (1), 170-1.
50. Thangavelu, B.; Bhansali, P.; Viola, R. E., Elaboration of a fragment library hit produces potent and selective aspartate semialdehyde dehydrogenase inhibitors. *Bioorganic & Medicinal Chemistry* **2015**, *23* (20), 6622-31.
51. Pavlovsky, A. G.; Thangavelu, B.; Bhansali, P.; Viola, R. E., A cautionary tale of structure-guided inhibitor development against an essential enzyme in the aspartate-biosynthetic pathway. *Acta crystallographica. Section D, Biological crystallography* **2014**, *70* (Pt 12), 3244-52.
52. Pavlovsky, A. G.; Liu, X.; Faehnle, C. R.; Potente, N.; Viola, R. E., Structural characterization of inhibitors with selectivity against members of a homologous enzyme family. *Chemical biology & drug design* **2012**, *79* (1), 128-36.
53. Ogindo, C. O.; Khraiwesh, M. H.; George, M., Jr.; Brandy, Y.; Brandy, N.; Gugssa, A.; Ashraf, M.; Abbas, M.; Southerland, W. M.; Lee, C. M.; Bakare, O.; Fang, Y., Novel drug design for Chagas disease via targeting Trypanosoma cruzi tubulin: Homology modeling and binding pocket prediction on Trypanosoma cruzi tubulin polymerization inhibition by naphthoquinone derivatives. *Bioorganic & Medicinal Chemistry* **2016**, *24* (16), 3849-55.
54. Mostert, S.; Petzer, A.; Petzer, J. P., Evaluation of Natural and Synthetic 1,4-naphthoquinones as Inhibitors of Monoamine Oxidase. *Chemical biology & drug design* **2016**, *87* (5), 737-46.
55. Johnston, P. A., Redox cycling compounds generate H₂O₂ in HTS buffers containing strong reducing reagents--real hits or promiscuous artifacts? *Current Opinion in Chemical Biology* **2011**, *15* (1), 174-82.
56. Dahal, G. P.; Viola, R. E., Structure of a fungal form of aspartate-semialdehyde dehydrogenase from *Aspergillus fumigatus*. *Acta Crystallogr F Structural Biology Communication* **2017**, *73* (Pt 1), 36-44.

57. Thomas, D.; Barbey, R.; Surdinkerjan, Y., Evolutionary Relationships between Yeast and Bacterial Homoserine Dehydrogenases. *FEBS letters* **1993**, *323* (3), 289-293.
58. DeLaBarre, B.; Thompson, P. R.; Wright, G. D.; Berghuis, A. M., Crystal structures of homoserine dehydrogenase suggest a novel catalytic mechanism for oxidoreductases. *Nature structural biology* **2000**, *7* (3), 238-44.
59. Gibson, D. G.; Young, L.; Chuang, R. Y.; Venter, J. C.; Hutchison, C. A.; Smith, H. O., Enzymatic assembly of DNA molecules up to several hundred kilobases. *Nature Methods* **2009**, *6* (5), 343-U41.
60. Jacques, S. L.; Ejim, L. J.; Wright, G. D., Homoserine dehydrogenase from *Saccharomyces cerevisiae*: kinetic mechanism and stereochemistry of hydride transfer. *Biochimica et biophysica acta* **2001**, *1544* (1-2), 42-54.
61. Ejim, L.; Mirza, I. A.; Capone, C.; Nazi, I.; Jenkins, S.; Chee, G. L.; Berghuis, A. M.; Wright, G. D., New phenolic inhibitors of yeast homoserine dehydrogenase. *Bioorganic & Medicinal Chemistry* **2004**, *12* (14), 3825-30.
62. Zhan, D.; Wang, D.; Min, W.; Han, W., Exploring the molecular basis for selective binding of homoserine dehydrogenase from *Mycobacterium leprae* TN toward inhibitors: a virtual screening study. *International Journal of Molecular Sciences* **2014**, *15* (2), 1826-41.
63. Xu, H.; Andi, B.; Qian, J.; West, A. H.; Cook, P. F., The alpha-aminoadipate pathway for lysine biosynthesis in fungi. *Cell Biochemistry & Biophysics* **2006**, *46* (1), 43-64.
64. Zabriskie, T. M.; Jackson, M. D., Lysine biosynthesis and metabolism in fungi. *Natural Products Reports* **2000**, *17* (1), 85-97.
65. Battye, T. G.; Kontogiannis, L.; Johnson, O.; Powell, H. R.; Leslie, A. G., iMOSFLM: a new graphical interface for diffraction-image processing with MOSFLM. *Acta crystallographica. Section D, Biological crystallography* **2011**, *67* (Pt 4), 271-81.
66. Collaborative, C. P., The CCP4 suite: programs for protein crystallography. *Acta crystallographica. Section D, Biological crystallography* **1994**, *50* (Pt 5), 760.
67. McCoy, A. J.; Grosse-Kunstleve, R. W.; Adams, P. D.; Winn, M. D.; Storoni, L. C.; Read, R. J., Phaser crystallographic software. *Journal of Applied Crystallography* **2007**, *40* (Pt 4), 658-674.
68. Murshudov, G. N.; Skubak, P.; Lebedev, A. A.; Pannu, N. S.; Steiner, R. A.; Nicholls, R. A.; Winn, M. D.; Long, F.; Vagin, A. A., REFMAC5 for the refinement of macromolecular crystal structures. *Acta crystallographica. Section D, Biological crystallography* **2011**, *67* (Pt 4), 355-67.

69. Cowtan, K., The Buccaneer software for automated model building. 1. Tracing protein chains. *Acta crystallographica. Section D, Biological crystallography* **2006**, 62 (Pt 9), 1002-11.
70. Emsley, P.; Cowtan, K., Coot: model-building tools for molecular graphics. *Acta crystallographica. Section D, Biological crystallography* **2004**, 60 (Pt 12 Pt 1), 2126-32.
71. DeLano, W. L., The PyMol Molecular Graphics System. <http://www.pymol.org> **2002**.
72. Krissinel, E.; Henrick, K., Inference of macromolecular assemblies from crystalline state. *Journal of Molecular Biology* **2007**, 372 (3), 774-97.
73. Joosten, R. P.; Salzemann, J.; Bloch, V.; Stockinger, H.; Berglund, A.-C.; Blanchet, C.; Bongcam-Rudloff, E.; Combet, C.; Da Costa, A. L.; Deleage, G.; Diarena, M.; Fabbretti, R.; Fettahi, G.; Flegel, V.; Gisel, A.; Kasam, V.; Kervinen, T.; Korpelainen, E.; Mattila, K.; Pagni, M.; Reichstadt, M.; Breton, V.; Tickle, I. J.; Vriend, G., PDB_REDO: automated re-refinement of X-ray structure models in the PDB. *Journal of Applied Crystallography* **2009**, 42 (3), 376-384.
74. Winn, M. D.; Ballard, C. C.; Cowtan, K. D.; Dodson, E. J.; Emsley, P.; Evans, P. R.; Keegan, R. M.; Krissinel, E. B.; Leslie, A. G.; McCoy, A.; McNicholas, S. J.; Murshudov, G. N.; Pannu, N. S.; Potterton, E. A.; Powell, H. R.; Read, R. J.; Vagin, A.; Wilson, K. S., Overview of the CCP4 suite and current developments. *Acta crystallographica. Section D, Biological crystallography* **2011**, 67 (Pt 4), 235-42.
75. Laskowski, R. A.; MacArthur, M. W.; Moss, D. S.; Thornton, J. M., Procheck - a Program to Check the Stereochemical Quality of Protein Structures. *Journal of Applied Crystallography* **1993**, 26 (2), 283-291.
76. Berman, H. M.; Westbrook, J.; Feng, Z.; Gilliland, G.; Bhat, T. N.; Weissig, H.; Shindyalov, I. N.; Bourne, P. E., The Protein Data Bank. *Nucleic acids research* **2000**, 28 (1), 235-42.
77. Kabsch, W., Xds. *Acta crystallographica. Section D, Biological crystallography* **2010**, 66 (Pt 2), 125-32.
78. Laskowski, R. A.; MacArthur, M. W.; Moss, D. S.; Thornton, J. M., PROCHECK: a program to check the stereochemical quality of protein structures. *Journal of Applied Crystallography* **1993**, 26, 283-291.
79. DeLano, W. L. *The PyMOL Molecular Graphics System*, DeLano Scientific: San Carlos, CA, **2002**.
80. Holm, L.; Rosenstrom, P., Dali server: conservation mapping in 3D. *Nucleic acids research* **2010**, 38 (Web Server issue), W545-9.

81. Blanco, J.; Moore, R. A.; Viola, R. E., Capture of an intermediate in the catalytic cycle of L-aspartate- α -semialdehyde dehydrogenase *Proceedings of the National Academy of Science* **2003**, *100*, 12613-12617.
82. Kumar, R.; Garg, P.; Bharatam, P. V., Shape-based virtual screening, docking, and molecular dynamics simulations to identify Mtb-ASADH inhibitors. *Journal of biomolecular structure & dynamics* **2015**, *33* (5), 1082-93.
83. Luniwal, A.; Wang, L.; Pavlovsky, A.; Erhardt, P. W.; Viola, R. E., Molecular docking and enzymatic evaluation to identify selective inhibitors of aspartate semialdehyde dehydrogenase. *Bioorganic & Medicinal Chemistry* **2012**, *20* (9), 2950-6.
84. Kumar, R.; Garg, P., Molecular Modeling and Active Site Binding Mode Characterization of Aspartate beta-Semialdehyde Dehydrogenase Family. *Molecular Informatics* **2013**, *32* (4), 377-83.
85. Kumar, R.; Garg, P.; Bharatam, P. V., Pharmacoinformatics analysis to identify inhibitors of Mtb-ASADH. *Journal of biomolecular structure & dynamics* **2016**, *34* (1), 1-14.
86. Oviya, I.; Sharanya, M.; Jeyam, M., Phytocompounds from *Sphaeranthus indicus* and *Wrightia tinctoria* targeting fungal Aspartate pathway – An in silico evaluation. *Advances in Biomedicine and Pharmacy* **2015**, *2* (1), 13-21.
87. Morris, G. M.; Goodsell, D. S.; Halliday, R. S.; Huey, R.; Hart, W. E.; Belew, R. K.; Olson, A. J., Automated docking using a Lamarckian genetic algorithm and an empirical binding free energy function. *Journal of Computational Chemistry* **1998**, *19* (14), 1639-1662.
88. Trott, O.; Olson, A. J., AutoDock Vina: improving the speed and accuracy of docking with a new scoring function, efficient optimization, and multithreading. *Journal of Computational Chemistry* **2010**, *31* (2), 455-61.
89. Morris, G. M. G., D. S.; Pique, M. E.; Lindstrom, W. L.; Huey, R.; Forli, S.; Hart, W. E.; Halliday, S.; Belew, R.; Olson, A. J. , Autodock 4.2 UserGuide.
90. Morris, G. M.; Huey, R.; Lindstrom, W.; Sanner, M. F.; Belew, R. K.; Goodsell, D. S.; Olson, A. J., AutoDock4 and AutoDockTools4: Automated docking with selective receptor flexibility. *Journal of Computational Chemistry* **2009**, *30* (16), 2785-91.
91. Chang, M. W.; Ayeni, C.; Breuer, S.; Torbett, B. E., Virtual screening for HIV protease inhibitors: a comparison of AutoDock 4 and Vina. *PLoS One* **2010**, *5* (8), e11955.
92. Irwin, J. J.; Shoichet, B. K., ZINC--a free database of commercially available compounds for virtual screening. *Journal of Chemical Information & Modelling* **2005**, *45* (1), 177-82.

93. Baba, N.; Akaho, E., VSDK: Virtual screening of small molecules using AutoDock Vina on Windows platform. *Bioinformatics* **2011**, *6* (10), 387-388.
94. Wallace, A. C.; Laskowski, R. A.; Thornton, J. M., LIGPLOT: a program to generate schematic diagrams of protein-ligand interactions. *Protein Engineering* **1995**, *8* (2), 127-34.
95. Dahal, G. P.; Viola, R. E., A Fragment Library Screening Approach to Identify Selective Inhibitors against an Essential Fungal Enzyme. *SLAS DISCOVERY: Advancing Life Sciences R&D* **2018**, 2472555218767844.
96. Lipinski, C. A.; Lombardo, F.; Dominy, B. W.; Feeney, P. J., Experimental and computational approaches to estimate solubility and permeability in drug discovery and development settings. *Advanced drug delivery reviews* **2001**, *46* (1-3), 3-26.
97. Leite, M. C.; de Brito Bezerra, A. P.; de Sousa, J. P.; de Oliveira Lima, E., Investigating the antifungal activity and mechanism(s) of geraniol against *Candida albicans* strains. *Medical Mycology* **2015**, *53* (3), 275-84.
98. Lopez-Martinez, R., Candidosis, a new challenge. *Clinics in dermatology* **2010**, *28* (2), 178-84.
99. Kauffman, C. A.; Carver, P. L., Update on echinocandin antifungals. *Seminars in respiratory and critical care medicine* **2008**, *29* (2), 211-9.
100. Ellis, D., Amphotericin B: spectrum and resistance. *Journal of Antimicrobial Chemotherapy* **2002**, *49* Suppl 1, 7-10.
101. Jastrzebowska, K.; Gabriel, I., Inhibitors of amino acids biosynthesis as antifungal agents. *Amino acids* **2015**, *47* (2), 227-49.
102. Rex, J. H., *Reference method for broth dilution antifungal susceptibility testing of filamentous fungi: approved standard*. Clinical and Laboratory Standards Institute: **2008**.
103. Miao, H.; Zhao, L.; Li, C.; Shang, Q.; Lu, H.; Fu, Z.; Wang, L.; Jiang, Y.; Cao, Y., Inhibitory effect of Shikonin on *Candida albicans* growth. *Biological & pharmaceutical bulletin* **2012**, *35* (11), 1956-63.
104. Matalon, R.; Michals, K.; Sebesta, D.; Deanching, M.; Gashkoff, P.; Casanova, J., Aspartoacylase deficiency and N-acetylaspartic aciduria in patients with Canavan disease. *American Journal of Medical Genetics* **1988**, *29* (2), 463-71.
105. Ahmed, S. S.; Gao, G., Making the White Matter Matters: Progress in Understanding Canavan's Disease and Therapeutic Interventions Through Eight Decades. *JIMD Reports* **2015**, *19*, 11-22.

106. Le Coq, J.; An, H. J.; Lebrilla, C.; Viola, R. E., Characterization of human aspartoacylase: the brain enzyme responsible for Canavan disease. *Biochemistry* **2006**, *45* (18), 5878-84.
107. Wang, Q.; Zhao, M.; Parungao, G. G.; Viola, R. E., Purification and characterization of aspartate N-acetyltransferase: A critical enzyme in brain metabolism. *Protein Expression & Purification* **2016**, *119*, 11-8.
108. Moffett, J. R.; Ross, B.; Arun, P.; Madhavarao, C. N.; Namboodiri, A. M., N-Acetylaspartate in the CNS: from neurodiagnostics to neurobiology. *Progress in Neurobiology* **2007**, *81* (2), 89-131.
109. Baslow, M. H., Brain N-acetylaspartate as a molecular water pump and its role in the etiology of Canavan disease: a mechanistic explanation. *Journal of Molecular Neurosciences* **2003**, *21* (3), 185-90.
110. Zano, S.; Malik, R.; Szucs, S.; Matalon, R.; Viola, R. E., Modification of aspartoacylase for potential use in enzyme replacement therapy for the treatment of Canavan disease. *Molecular Genetics & Metabolism* **2011**, *102* (2), 176-80.
111. Leone, P.; Janson, C. G.; Bilaniuk, L.; Wang, Z.; Sorgi, F.; Huang, L.; Matalon, R.; Kaul, R.; Zeng, Z.; Freese, A.; McPhee, S. W.; Mee, E.; During, M. J., Aspartoacylase gene transfer to the mammalian central nervous system with therapeutic implications for Canavan disease. *Annals of Neurology* **2000**, *48* (1), 27-38.
112. Guo, F.; Bannerman, P.; Mills Ko, E.; Miers, L.; Xu, J.; Burns, T.; Li, S.; Freeman, E.; McDonough, J. A.; Pleasure, D., Ablating N-acetylaspartate prevents leukodystrophy in a Canavan disease model. *Annals of Neurology* **2015**, *77* (5), 884-8.
113. Lou, T. F.; Sethuraman, D.; Dospoy, P.; Srivastva, P.; Kim, H. S.; Kim, J.; Ma, X.; Chen, P. H.; Huffman, K. E.; Frink, R. E.; Larsen, J. E.; Lewis, C.; Um, S. W.; Kim, D. H.; Ahn, J. M.; DeBerardinis, R. J.; White, M. A.; Minna, J. D.; Yoo, H., Cancer-Specific Production of N-Acetylaspartate via NAT8L Overexpression in Non-Small Cell Lung Cancer and Its Potential as a Circulating Biomarker. *Cancer prevention research (Philadelphia, Pa.)* **2016**, *9* (1), 43-52.
114. Zand, B.; Previs, R. A.; Zacharias, N. M.; Rupaimoole, R.; Mitamura, T.; Nagaraja, A. S.; Guindani, M.; Dalton, H. J.; Yang, L.; Baddour, J.; Achreja, A.; Hu, W.; Pecot, C. V.; Ivan, C.; Wu, S. Y.; McCullough, C. R.; Gharpure, K. M.; Shoshan, E.; Pradeep, S.; Mangala, L. S.; Rodriguez-Aguayo, C.; Wang, Y.; Nick, A. M.; Davies, M. A.; Armaiz-Pena, G.; Liu, J.; Lutgendorf, S. K.; Baggerly, K. A.; Eli, M. B.; Lopez-Berestein, G.; Nagrath, D.; Bhattacharya, P. K.; Sood, A. K., Role of Increased n-acetylaspartate Levels in Cancer. *Journal of the National Cancer Institute* **2016**, *108* (6), djv426.

115. Burri, R.; Steffen, C.; Herschkowitz, N., N-acetyl-L-aspartate is a major source of acetyl groups for lipid synthesis during rat brain development. *Developmental Neuroscience* **1991**, *13* (6), 403-11.
116. Goldstein, F. B., The enzymatic synthesis of N-acetyl-L-aspartic acid by subcellular preparations of rat brain. *The Journal of biological chemistry* **1969**, *244* (15), 4257-60.
117. Tahay, G.; Wiame, E.; Tyteca, D.; Courtoy, P. J.; Van Schaftingen, E., Determinants of the enzymatic activity and the subcellular localization of aspartate N-acetyltransferase. *The Biochemical Journal* **2012**, *441* (1), 105-12.
118. Rosenbaum, D. M.; Cherezov, V.; Hanson, M. A.; Rasmussen, S. G.; Thian, F. S.; Kobilka, T. S.; Choi, H. J.; Yao, X. J.; Weis, W. I.; Stevens, R. C.; Kobilka, B. K., GPCR engineering yields high-resolution structural insights into beta2-adrenergic receptor function. *Science (New York, N.Y.)* **2007**, *318* (5854), 1266-73.
119. Jin, L.; Stec, B.; Lipscomb, W. N.; Kantrowitz, E. R., Insights into the mechanisms of catalysis and heterotropic regulation of Escherichia coli aspartate transcarbamoylase based upon a structure of the enzyme complexed with the bisubstrate analogue N-phosphonacetyl-L-aspartate at 2.1 Å. *Proteins: Structure, Function, and Bioinformatics* **1999**, *37* (4), 729-742.
120. Zeringo, N. A.; Bellizzi, J. J., 3rd, A PER2-derived mechanism-based bisubstrate analog for casein kinase Iepsilon. *Chemical biology & drug design* **2014**, *84* (6), 697-703.
121. Focia, P. J.; Craig, S. P., 3rd; Eakin, A. E., Approaching the transition state in the crystal structure of a phosphoribosyltransferase. *Biochemistry* **1998**, *37* (49), 17120-7.
122. Jencks, W. P., Coenzyme A Transferases. *The Enzymes* **1973**, *9*, 483-496.

Appendices

Appendix A

Figure A - 1) Autodock vina configuration file

Config.txt (2,3-dichloro-1,4-napthoquinone as a ligand with 3hsk_monomer as a receptor)

receptor = 3HSK_monomer.pdbqt

ligand = 2,3-dichloro-1,4-napthoquinone.pdbqt

out = 3hsk_2,3-dichloro-1,4-napthoquinone _out.pdbqt

log = 3hsk_2,3-dichloro-1,4-napthoquinone _log.txt

num_modes = 20

exhaustiveness = 16

center_x = 23.41

center_y = -0.854

center_z = 24.774

size_x = 30

size_y = 28

size_z = 30

Figure A - 2) VHTS parameters

a) VHTS config file

receptor = 3HSK_monomer.pdbqt

ligand = *.pdbqt

```
out = *.pdbqt
```

```
log = *.txt
```

```
num_modes = 20
```

```
exhaustiveness = 16
```

```
center_x = 24.793
```

```
center_y = 2.709
```

```
center_z = 23.112
```

```
size_x = 30
```

```
size_y = 28
```

```
size_z = 30
```

```
b) VS01.bash
```

```
#!/bin/bash
```

```
for f in ZINC*.pdbqt; do b=`basename $f .pdbqt`; echo Processing ligand $b; mkdir -p  
data01; ./Vina/vina --config conf.txt --ligand $f --out data01/$f.pdbqt --log data01/$f.txt;  
done
```

```
Figure A - 3) Result analysis
```

```
cd data01
```

```
grep " 1 " *.txt | cut -c1-12,35-42 >>result
```

```
cat result
```

Appendix B

Figure B) Configuration file of MD simulation minimization and equilibration

```
## ADJUSTABLE PARAMETERS
structure      /usr/people/Test1/NAMD_2.11_Linux-x86_64-multicore/spc_si.psf
coordinates    /usr/people/Test1/NAMD_2.11_Linux-x86_64-multicore/spc_si.pdb

set temperature 310
set outputname  spc_wb_eq_750000

firsttimestep  0
## SIMULATION PARAMETERS                                     ##
# Input
paraTypeCharmm      on
parameters           /usr/people/Test1/NAMD_2.11_Linux-x86_64-
multicore/par_all27_prot_lipid.inp
temperature          $temperature
# Force-Field Parameters
exclude              scaled1-4
1-4scaling           1.0
cutoff               12.0
switching            on
switchdist           10.0
pairlistdist         14.0

# Integrator Parameters
timestep             2.0 ;# 2fs/step
rigidBonds           all ;# needed for 2fs steps
nonbondedFreq        1
fullElectFrequency   2
stepspercycle        10
# Constant Temperature Control
langevin             on ;# do langevin dynamics
langevinDamping      1 ;# damping coefficient (gamma) of 1/ps
langevinTemp         $temperature
langevinHydrogen     off ;# don't couple langevin bath to hydrogens
```

```

# Periodic Boundary Conditions
cellBasisVector1 72.0 0. 0.0
cellBasisVector2 0.0 66.0 0.0
cellBasisVector3 0.0 0 71.0
cellOrigin      5.2 -1.3 3.7

wrapAll        on

# PME (for full-system periodic electrostatics)
PME            yes
PMEGridSpacing 1.0

#manual grid definition
#PMEGridSizeX 45
#PMEGridSizeY 45
#PMEGridSizeZ 48

# Constant Pressure Control (variable volume)
useGroupPressure yes ;# needed for rigidBonds
useFlexibleCell  no
useConstantArea  no
langevinPiston  on
langevinPistonTarget 1.01325 ;           # in bar -> 1 atm
langevinPistonPeriod 100.0
langevinPistonDecay 50.0
langevinPistonTemp $temperature

# Output
outputName      $outputname

restartfreq     250 ;# 500steps = every 1ps
dcdfreq        250
xstFreq        250
outputEnergies 100
outputPressure 100

margin         2.5


## EXECUTION SCRIPT                                ##

# Minimization
minimize       10000
reinitvels     $temperature
run 5000000 ;# 10ns

```


Appendix C

Figure C) DLS parameters during analysis of AfASADH sample

Standard report			
Created by: DLSuser			
Created at: 10/11/2016 11:50:26 AM			
General			
Measurement name	AFDILUTED	User	DLSuser
Method		Time	10/11/2016 11:44:37 AM
Status	Succeeded		
Settings			
Measurement cell	Disposable	Equilibration time	0h 01m 00s
Angle	Automatic	Analysis model	General
Target Temperature	20.0 °C	Cumulant model	Advanced
Quality			
Quality mode	Automatic	Measurement time	0h 00m 10s
Number of runs	60		
Filter			
Attenuation mode	Automatic	Attenuation	0
Focus			
Focus mode	Automatic	Focus position	0 mm
Material			
Name	Protein	Refractive index	1.4500
Absorption	0.0010		
Solvent			
Name	154mM NaCl	Refractive index	1.3323
Viscosity	1.0180 mPa.s		
Data output			
Hydrodynamic radius	64.51 nm	Polydispersity index	25.2 %
Intercept g ¹	0.8885	Mean intensity	283.2 kcounts/s
Filter optical density	1.036	Baseline	0.996
Focus position	-0.3 mm	Angle used	Side scatter
Processed runs	6	Transmittance	91.6 %
Kalliope version: 1.4.4		Measurement completed successfully	
Serial number: 81962747		Page 1 of 3	